A Nonlinear Approach to Ocean Wave Spectrum Extraction From Bistatic HF-Radar Data

by

© Murilo Teixeira Silva, B.Eng.

A thesis submitted to the School of Graduate Studies

in partial fulfilment of the requirements for the

degree of Master of Engineering

Faculty of Engineering and Applied Science

Memorial University of Newfoundland

October 2017

St. John's Newfoundland Canada

Abstract

In this thesis, a new approach to the extraction of the directional ocean wave spectrum from bistatic high frequency (HF) radar data is proposed. The proposed method relies on the simplification of the second-order bistatic radar cross-section, analogous to the one presented by Shahidi and Gill [1] for the monostatic case, to facilitate the use of nonlinear optimization methods, such as regularized nonlinear least-squares.

Initially, the historic development of the techniques related to the extraction of the ocean wave spectrum from HF radar data is provided in order to contextualize the work of this thesis. Then, an overview of the theory related to ocean waves and the bistatic radar cross-section is shown. Later, the nonlinear optimization method used in this thesis, Tikhonov regularization in Hilbert spaces, is explained, as well as the theoretical background necessary to understand the method.

Once the theory is laid out, the simplification of the second-order bistatic HF radar cross section is presented. The simplification consists of a change of variables that allow the use of the "sifting" property of the Dirac delta function. This reduces the dependence of the second-order bistatic cross-section to a single variable. After the simplification process is shown, the methodology for extracting the directional ocean wave spectrum from bistatic HF radar data is discussed.

As a proof-of-concept, the method is initially applied to the second-order bistatic cross section, without the presence of noise. The method successfully extracted the directional ocean wave spectrum without assuming any function model for the non-directional ocean wave spectrum, and assuming a cosine-power model for the direc-

tional spreading function.

Next, the first-order bistatic HF radar cross section is added to the second-order cross section, and the proposed method is applied, still without noise present. The proposed method was also able to extract the directional ocean wave spectrum and very low error is added by the inclusion of the first-order cross section.

Finally, different levels of noise are added to the cross section including the first- and second- orders, and the presented method is applied for the extraction. Again, the method yields good results, with acceptable levels of error for the different noise levels.

This new approach to the extraction of the directional ocean wave spectrum from bistatic HF radar data presents, to the author's knowledge, the first nonlinear extraction method for bistatic HF radar data. Further developments of the technique, such as the use of different nonlinear extraction methods, or a general directional spreading function, are suggested.

Acknowledgements

The author wishes to thank the Faculty of Engineering and Applied Science, Memorial University of Newfoundland (MUN), for affording him the opportunity of conducting this work. Particularly, the supervision of Prof. Eric W. Gill and Dr. Reza Shahidi and their interest and patience during the whole process are greatly appreciated. Their invaluable insights and suggestions were vital to the completion of this work.

The insights in the early stages of research provided by Dr. Wei Wang, Dr. Shuyan Chen, and Prof. James Munroe are worthy of special thanks. Thanks also to former and current members of the Radar and Remote Sensing Group at MUN, especially to Dr. Weimin Huang, Dr. Khalid El-Darymli, Mr. Brian Kidney, Mr. Xinlong Liu, Mr. Qingyun Yan, and Ms. Yue Ma, for providing a forum for discussion and for the invaluable advice and interesting conversations regarding the work at hand.

This work could not have been completed without the graduate student support from the Natural Science and Engineering Research Council (NSERC) grants to Dr. Eric W. Gill.

Finally, the author deeply appreciates the unfailing patience, understanding and support from his wife, Rafaela Silva, and his parents, family and friends in Brazil and Canada.

Contents

List of Tables

List of Figures

List of Symbols

The page numbers in this list indicate the place of the first appearance. There are various symbols used throughout this thesis, some of them not included in this list. In these cases, the symbols are defined immediately before or after their usage, or their meaning is obvious from the context.

ρ_{01}	Distance between transmitter and first scatter, page 4
ρ_{n0}	Distance between the n^{th} scatter and the receiver, page 4
g	Acceleration due to gravity, page 17
K	Magnitude of the ocean wave-number, page 17
ω	Ocean wave angular frequency, page 17
f	Ocean wave frequency, page 17
γ	Ratio between surface tension and water density, page 17
h	Depth of the ocean, page 17
λ	Wavelength of the ocean wave, page 18
T	Ocean wave period, page 18

ξ	Sea surface displacements from the mean level, page 23
r	Generic vector in the x-y plane, page 23
$\hat{\Psi}(\omega, \theta_{\mathbf{K}})$	Frequency-dependent directional ocean wave spectrum, page 24
$\hat{S}(K, \theta_{\mathbf{K}})$	Wave-number directional ocean wave spectrum, page 24
$\tilde{\Psi}(\omega)$	Frequency-dependent non-directional symmetric ocean wave spectrum, page 25
$D(\theta_{\mathbf{K}})$	Directional spreading function, page 25
$\tilde{S}(K)$	Wave-number non-directional symmetric ocean wave spectrum, page 26
$\Psi(\omega)$	Frequency-dependent non-directional ocean wave spectrum, page 26
$S(K)$	Wave-number non-directional ocean wave spectrum, page 26
$\overline{H_{1/3}}$	Significant wave height, page 28
$\overline{T}$	Mean ocean wave period, page 28
T_p	Peak ocean wave period, page 28
ω_p	Peak ocean wave frequency, page 28
K_p	Peak ocean wave-number, page 28
$\bar{\theta}$	Mean wave direction, page 28
u_*	Friction velocity of the wind over the water surface, page 30
X_w	Wind fetch, page 30

$\overline{F}$	Dimensionless function used in the similarity theory [4], page 30
U_z	Average wind velocity measured at z meters above sea level, page 31
C	Charnock-Ellison constant, page 31
α	Parameter to the Pierson-Moskowitz spectral model ($\alpha = 8.1 \times 10^{-3}$), page 31
β	Parameter to the Pierson-Moskowitz spectral model ($\beta = 0.74$), page 31
s	Longuet-Higgins spreading factor, page 32
Γ	Gamma function, page 32
${}_i\xi(\mathbf{r}, t)$	Surface displacement caused by ith-order waves, page 35
${}_iP_{\mathbf{K},\omega}$	Fourier components of the surface displacement caused by ith-order waves, page 35
${}_H\Gamma$	Hydrodynamic coupling coefficient, page 35
t	An instant in time, page 38
t_0	An instant in time that defines a particular scattering ellipse, page 38
$(E^+_{0_n})_{11}$	Total electric field at the receiver, page 38
$(E^+_{0_n})_{11}$	First-order electric field at the receiver, page 38
$(E^+_{0_n})_{2P}$	Second-order patch scattering electric field at the receiver, page 38
$(E^+_{0_n})_{2T}$	Second-order transmitter foot scattering electric field at the receiver, page 38

$(E_{0_n}^{+})_{2R}$ Second-order receiver foot scattering electric field at the receiver, page 38

ω_d Doppler shift in rad/s, page 39

σ_{11} First-order radar cross section, page 39

σ_{2P} Second-order patch scattering radar cross section, page 39

σ_{2T} Second-order transmitter foot scattering radar cross section, page 39

σ_{2R} Second-order receiver foot scattering radar cross section, page 39

$\boldsymbol{\rho}$ Vector between the transmitter and the receiver, page 40

$\boldsymbol{\rho_{0i}}$ Vector between the transmitter and the ith scatter, page 40

$\boldsymbol{\rho_{n0}}$ Vector between the last scatter ant the receiver, page 40

$\mathbf{N}$ Normal to the ellipse at the scattering patch, page 40

$\mathbf{T}$ Tangent to the ellipse at the scattering patch, page 40

$\mathbf{K}$ Resulting wave vector, page 40

θ_{0i} Direction of the vector between the transmitter and the i^{th} scatter, page 40

ϕ Bistatic angle, page 40

$\theta_{\mathbf{N}}$ Normal angle, page 40

$\Delta\rho_s$ Width of the scattering patch viewed by a pulsed radar, page 42

τ_o Pulse width a pulsed radar, page 42

c	Speed of light $c = 3 \times 10^8$ m/s, page 42
A_P	Area of the scattering patch, page 42
ρ_{n0}	Distance between the transmitter and the scattering patch, page 42
θ_{01}	Transmitter look direction, page 43
k_o	Wave-number of the radar transmitted signal, page 44
Sa	Sinc function, page 44
K_B	Bragg peak wave-number, page 44
ω_B	Bragg peak frequency, page 44
f_o	Transmitter frequency, page 45
θ_w	Wind direction, page 45
S_{PM}	Pierson-Moskowitz spectrum, page 46
$\hat{S}(mK)$	Non-directional symmetric ocean wave spectrum, page 46
${}_s\Gamma_P$	Symmetricized coupling coefficient, page 47
Γ_P	Coupling coefficient, page 47
${}_E\Gamma_P$	Electromagnetic coupling coefficient, page 47
Δ	Impedance of the ocean surface, page 47
$\hat{\boldsymbol{\rho}}_{\mathbf{0n}}$	Unit vector in the direction of the $0n$ scatter, page 47

$h^{-,+}$	Hydrodynamic peaks in the second-order cross section, page 48
$e_{1,2}^{-,+}$	Electromagnetic peaks in the second-order cross section, page 48
d	Distance between elements of a metric space, page 56
F	Nonlinear operator, page 58
$\mathbf{x}$	Parameters of the inverse problem, page 58
$\mathbf{y}_0$	Ideal data of the inverse problem. obtained by the nonlinear operator F, page 58
X	Parameter space, page 58
Y	Data space, page 58
$K(z,t)$	Kernel of the Fredholm integral equation, page 58
N	Nonlinear function of the input to the Fredholm integral equation, page 58
x	Input to the Fredholm integral equation, page 58
$y(z)$	Output of the Fredholm integral equation, page 58
δ	Output perturbation level, page 60
x^*	Parameter that helps to define the selection criterion in the case of multiple least-square solutions in the Tikhonov regularization, page 60
α	Regularization parameter, page 60
D^2	Second-order differential operator, page 62

D^1	First-order differential operator, page 62
J	Jacobian, page 65
$H(Y_1, Y_2)$	Kernel of the second-order patch scattering cross section after change of coordinates, page 66
Y_1	Second-order cross section proposed, page 66
Y_2	Second-order cross section proposed coordinate, page 66
σ_P	Patch Scattering Cross Section, page 94
n_r	Time series for the noise signal, page 105
ϵ	Uniform random phase varying from 0 to 2π, page 105
$h[\cdot]$	Heaviside function, page 105
B	Bandwidth of the signal, page 105
S_N	Power Spectral Density of the noise, page 105
ω'	Radian frequency, page 105
S_σ	Power spectral density of the received radar signal, page 105
C	Radar attenuation function, page 105
G_T	Gain of the transmitter, page 107
G_R	Gain of the receiver, page 107
P_T	Power of the transmitter, page 107

λ_o	Wavelength of the transmitter signal, page 107
ρ_{01}	Distance between the transmitter and the first scatter, page 107
ρ_{02}	Distance between the second scatter and the receiver, page 107
$\mathcal{F}$	Transmission path attenuation function, page 107
E_r	Received radar time series, page 107

Chapter 1

Introduction

1.1 Research Rationale

In the past decades, there has been a great focus given to the study of the ocean surface. Efforts to advance this topic have been driven by groups in different industries, such as scientists interested in the behaviour of the ocean surface, government entities interested in monitoring resources and detecting threats in their sovereign waters, and companies involved in navigation, or in the exploration and development of ocean-related renewable and non-renewable resources. As these industries develop, the demand for accurate information about the upper ocean increases, leading to new technologies and instruments applied to the assessment of and the gathering of different measurements from the ocean surface. Among these measurements, the directional ocean wave spectrum is the one that most thoroughly describes the ocean's behaviour.

One of the main features of the ocean surface is its inherent randomness, which im-

plies that stochastic analysis must be applied to understand and predict its behaviour. Furthermore, the periodicity of the ocean surface also suggests the use of frequency-domain techniques, of which spectral analysis is the most widely used. Stochastic spectral analysis can deal with the distribution of energy in different frequencies and directions, which makes it suitable for ocean surface mapping. The directional ocean wave spectrum, is the most holistic measurement in the study of the upper ocean, and other measurements such as significant wave height, peak wave period, and dominant wave direction can be determined from it. However, obtaining such a measurement is not an easy task.

Different instruments, such as wave buoys, current meters, and pressure sensors, are used for ocean surface measurements, while wind information over the ocean, such as speed and direction, is collected by anemometers installed on ships and buoys [5]. These instruments provide direct measurements of the quantities in question, which makes their information easy to interpret. Despite this, excepting ship anemometers and current drifters, these instruments share the disadvantage of being only able to collect information from the point at which they are installed. This makes mapping large regions of the ocean with these instruments a costly procedure.

Due to the high costs involved in mapping the ocean surface using the aforementioned instruments, over the years, the use of remote sensing for this purpose has increased to deal with the high expense associated with other methods. Microwave radars have been extensively used and methods to extract ocean information such as dominant wave direction, wave periods and spectral shape have been developed. The underlying physical mechanism of oceanographic radar applications relies on the fact that electromagnetic waves will, at grazing incidence, primarily interact with

ocean waves having wavelengths that are half the length of the radar's wavelength — a process known as Bragg scattering. Considering that microwave radars operate in wavelengths ranging from 0.1 cm to 100 cm, they will mainly interact with short ocean waves, which carry a small fraction of the energy of the wave field, that is concentrated over ocean waves of decametric wavelengths. Since the interaction between short and long waves is a complex process, the inference of the ocean wave spectrum by exploring the relationship between short and long waves is a difficult task.

High-frequency (HF) radars bring the inherent advantage of interacting with decametric wavelength ocean waves, since their operating frequencies range from 3 MHz to 30 MHz, which allows them to take advantage of Bragg scattering. Also, HF radars are easily steerable and have the capacity to make over-the-horizon measurements, either by ground or by sky wave propagation, allowing measurements at distances as far as 300 km from the source of the transmission in ground wave, or 3000 km in sky wave propagation. Combining these characteristics, HF radar presents itself as a useful instrument to observe the ocean surface.

HF radars in radio oceanography are presented in one of the following configurations: monostatic and bistatic. The difference between these configurations lies in the distance between transmitter and receiver, compared to the distance to the scattering patch. In a monostatic configuration, the distance between transmitter and receiver is much smaller than the one between them and the scattering patch (i.e. the transmitter and receiver are essentially co-located), while in a bistatic configuration, the distance between receiver and transmitter is comparable to the one to the scattering patch [6], although there is still a discussion in the scientific community as to a precise definition of the term "comparable distance" [7]. This difference between a

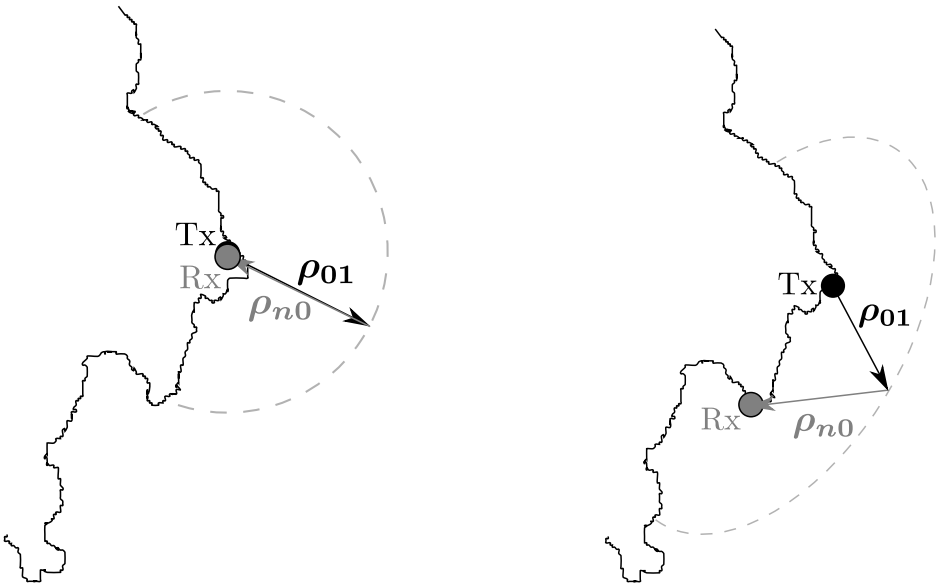

(a) Monostatic Configuration (b) Bistatic Configuration

Figure 1.1: Different radar configurations used for HF radars in radio oceanography

bistatic and a monostatic configuration can be observed in Figure 1.1, where ρ_{01} is the vector between transmitter and the first scatter, and ρ_{0n} is the distance between the n^{th} scatter and the receiver. Each of these configurations has its advantages and disadvantages.

One phenomenon in radio oceanography that affects the quality of the signal is direct communication between transmitter and receiver. This generates a sharp peak at zero Doppler shift, obfuscating information coming from the scattering patch. Direct communications are more likely to occur with radars in a monostatic configuration due to the proximity of the transmitter to the receiver.

Another advantage of a bistatic configuration over a monostatic one is the reduction of costs in building dual radar systems. HF radars, either in monostatic or bistatic configurations, can only obtain the magnitude of the angle in which the ocean

waves are travelling. This introduces an ambiguity in the directional characteristic of the ocean wave spectrum to be extracted from radar data. This problem can be overcome by the use of dual radar systems, meaning that two radars will be looking at the same patch of the ocean. In a monostatic configuration, two complete radars — including transmitter and receiver — would be necessary to implement this system, while in the bistatic case, only a second receiver would suffice. Therefore, a dual bistatic radar is more cost-effective than a dual monostatic.

While remote sensing instruments retrieve information over a broad swath of the ocean, the measurement of sea surface quantities relies on extraction techniques that are often mathematically complex or dependent on approximations that affect the accuracy of the results. The mathematical complexity of the extraction of ocean information from radar data comes from the formulation of the electromagnetic scattering process. In a bistatic configuration, this formulation is even more intricate, due to the elliptical coordinate analysis that is required in these systems. To simplify the extraction process, linearizations are often applied to the scattering expressions, which could potentially affect the accuracy of the results. Therefore, there is a demand for new ocean measurement extraction techniques from HF radar data that preserve the nonlinearity of the system and increase measurement accuracy.

This thesis proposes a new approach to the extraction of directional ocean wave spectra from bistatic HF radar data. This new method preserves the nonlinear characteristics of the cross section equations and further simplifies them to a single nonlinear Fredholm integral equation of the first kind, which is solved by nonlinear least-squares optimization. This inversion technique has been presented by Shahidi and Gill [1] for the monostatic case. Here the technique is generalized to a bistatic radar configura-

tion. The inclusion of first-order scattering in the inversion problem is also considered in this thesis. Since the extraction of the ocean wave spectrum is an ill-posed problem, a regularization technique should be used to improve convergence. Moreover, a smoothness constraint is introduced due to the natural smoothness of ocean wave spectra in the wavelengths that interact with the HF radar. Due to the unavailability of bistatic data to validate the method at the time this thesis was written, the technique was validated using noise-contaminated synthetic data.

1.2 Literature Review

Interactions between radio and ocean waves were initially reported during World War II, when radars were first employed at sea. The influence of the sea surface could be noticed in both microwave and high-frequency radars. Since the main purpose of these systems was target detection, this influence was referred to as "sea clutter". As the name suggests, the early efforts of radio scientists in this topic were directed towards the removal of clutter, while mathematicians and physicists were interested in the mechanisms that produced the interference. Scientists, such as Feinberg [8], Blake [9], and Rice [10], investigated electromagnetic propagation across rough surfaces, but their work was largely ignored by the radar community until 1955.

At the same time, physical oceanographers were interested in the problem of forecasting the ocean surface. Kinsman [11] offered a concise summary on the evolution of the wave forecasting problem until 1965. Of course, determining details of the directional ocean wave spectrum forms an important part of wave forecasting. Later developments on the topic were discussed by Massel [12]. According to Kinsman,

Pierson introduced the concept of stochastic spectral analysis to oceanography. After communications with Tuckey, Pierson had the idea of applying spectral analysis, a statistical method which up to that time had been applied by communication engineers to random signals, to the motion of the ocean surface. His first ideas on the topic were summarized in a two-volume report [13] published in 1952. In the same year, Neumann [14] published expressions relating the mean wind and the wave energy.

In 1953, Eckart [15] presented the acoustic scattering cross section of the sea surface as a function of the spatial spectrum of the surface waves, alluding to the possibility of obtaining the spatial spectrum of the ocean surface from this cross section. Since Eckart did not mention Pierson in his paper, this leads to the conclusion that he independently came up with the idea of using spectral analysis to understand the ocean surface contemporaneously. However, Eckart mentioned the difficulty of changing the directional parameter and frequency of the acoustic instrument as the main drawbacks on the suggestion to obtain the directional ocean wave spectrum. Based on Eckart's work, in 1954 Cox and Munk [16] presented what is possibly the first attempt to obtain sea surface spectral measurements using electromagnetic remote sensing devices — in this case, aerial photographs. In 1960, Cote *et al.* [17], in a report by the Stereo Wave Observation Project (SWOP), having Pierson as one of its group members, obtained directional wave spectra using stereo photographs. Clearly these attempts to assess the ocean surface used the visible part of the electromagnetic spectrum. Later, based on the observations by Moskowitz *et al.* [18] and on the similarity theory of Kitaigorodskii [4], Pierson and Moskowitz [19] derived their ocean wave spectrum model that would later become known as the Pierson-Moskowitz (PM) spectrum. In the following years, several physical oceanographers proposed different

spectral models for the ocean surface, accounting for different ocean conditions. These models are summarized by Massel [12].

The use of HF radars in oceanographic observations was only considered after Crombie [20] published a paper in which he described an experiment conducted at the Dominion Physical Laboratory in New Zealand. Crombie observed that the peaks in the Doppler radar spectrum produced by reflections from the ocean surface occurred at frequency shifts that could be predicted by Bragg's law — in other words, the ocean surface acts as diffraction gratings to the electromagnetic waves. These peaks were then called "Bragg peaks", after the physical law that predicts their positions in the Doppler spectrum. The results obtained by Crombie were later confirmed by Wait [21], who also noticed that the intensity of the peak was proportional to the height of the waves that reflected them.

One of the most important contributors to the theory and application of HF radars in oceanographic measurements is Dr. Donald Barrick. In 1970, after expanding Rice's perturbation theory [22, 23] and working on radar signal distortions due to volume and surface scattering [24], Barrick [25, 26, 27] applied perturbation theory to the propagation of electromagnetic waves of decametric wavelength — in other words, in the high-frequency region.

Based on Barrick's research, efforts on different fronts were made to devise a technique to extract the ocean wave spectrum from HF radar Doppler data. Munk and Nierenberg [28] observed that the cross section proposed by Barrick in [25] was related to Phillip's saturation constant, a feature of the nondirectional ocean wave spectrum. In this paper, they speculated on the use of HF radar to obtain the directional information of the ocean wave spectrum. In 1971, Hasselmann [29] suggested

that the Doppler spectrum sidebands related to second-order interactions would be proportional to the nondirectional ocean wave spectrum energy. Then, in 1972, Barrick devised the formulation for the first- [30] and second-order cross sections [31], where a clear relationship between the ocean wave spectrum and the radar received signal was presented. After Barrick and Snider [32] studied the statistics of the ocean wave spectrum, Barrick considered the extraction of ocean wave information. This resulted in publications on the extraction of wave parameters [33], and the nondirectional wave spectra [34] from the second-order cross section, following Hasselmann's insights. In the same year, Lipa [35] proposed a technique to extract the directional ocean wave spectrum by inverting Barrick's second-order cross section, where she used a linearization technique to convert the integral equation to a linear system. Her theoretical work was confirmed in 1978 using real HF radar data [36]. In the following years, Lipa partnered with Barrick and produced several papers on the topic [37–39], and together they founded CODAR (Coastal Ocean Dynamics Applications Radar) Ocean Sensors, Inc. with colleagues from the National Oceanic and Atmospheric Administration, in the United States.

In 1984, Srivastava [40] developed the formulation for the first- and second-order radar cross sections using Walsh's theory [41] which was based on generalized functions. Srivastava's formulation for the first-order cross section matched the one previously devised by Barrick, however, his second-order formulation also accounted for off-patch double scattering, as well as wave-wave and field-wave interactions covered in Barrick's theory. A summary accounting for different approaches to the scattering of electromagnetic waves across rough surfaces can be found in [3].

Later, in 1986, Wyatt *et al.* [42] and Wyatt [43] proposed a new method to extract

the ocean wave spectrum from HF radar data, extending a model-fitting technique proposed in a report by Lipa and Barrick [44]. By using this technique, the measured data were matched with a number of simulated Doppler spectra for different sea conditions. In 1990, Wyatt published a method in which she extended the Chahine-Twomey relaxation method [45, 46] to extract the directional ocean wave spectrum from radar data using Barrick's equations to describe the scattering. To obtain the directional characteristics of the spectrum without the inherent left-right ambiguity present in single-radar systems, Wyatt used a dual monostatic HF radar system, which allowed a more accurate result.

Using Barrick's cross section formulation, in 1990 Howell [47] developed an algorithm to extract ocean wave information from data obtained from single, or multiple narrow beam HF radar systems. Howell's algorithm was then adapted by Gill [5] to extract the ocean wave spectrum from wide-beam HF radar data. In 1993, Howell and Walsh [48] presented the technique in a paper, where they applied the algorithm to both the Barrick and Walsh *et al.* [49] cross section estimates. The technique returned better results with Walsh and Howell's estimates, confirming the model obtained by Walsh's generalized function technique.

The first author to approach ocean spectrum extraction without applying any linearization technique was Hisaki [50]. Hisaki used an optimization technique to invert the integral equation in Barrick's cross section, to which some constraints were applied due to the ill-posedness of the problem. Later research from Hisaki has expanded his nonlinear ocean wave spectrum extraction technique, and applied it to multiple radars [51–56].

A more recent approach to the extraction problem was proposed by Shahidi and

Gill [1], where the second-order cross section formulation presented by Howell and Walsh [48] was further reduced to a single-integral nonlinear Fredholm equation of the first kind, to which optimization techniques were applied to perform the inversion and obtain the directional ocean wave spectrum. The method has been validated using real data, which confirms the feasibility of the method [57], and additionally, a mathematically exact solution to the extraction of the nondirectional ocean wave spectra has been developed [58].

The developments reviewed to this point in this work, however, only accounted for the use of monostatic HF radar systems, not involving the bistatic configuration. Early works on the use of bistatic radars were presented by Pidgeon [59, 60], where he considered the use of the bistatic configuration for both aerial and satellite observations, and developing the cross section for the aerial case. According to Teague *et al.* [61], the first efforts to implement a bistatic HF surface-radar system came in the late 1960's, in a collaboration between Peterson, Munk and Nieremberg. Peterson would later collaborate with Teague and Tyler in order to conduct experiments that would lead to the first measurements of the directional ocean wave spectra for swell [62]. Further observations by Teague [63] concluded that a more refined, multifrequency experiment would be necessary to obtain a directional ocean wave spectrum for the local sea. Later, Barrick [64] explored the theory for the bistatic HF radar cross section, analyzing different radar configurations such as coast-coast, buoy-coast, and buoy-satellite. His studies of the bistatic configuration led to the development of the cross sections for bistatic radar configurations [31]. In the latter work, Barrick mentions a report by Nierenberg and Munk [65], in which a bistatic observation technique for the ocean wave spectrum in ocean wave number space was proposed. However,

due to the ubiquity of the monostatic radar for HF ground wave propagation, research on the bistatic case has not evolved at the same pace.

In 1999, Gill [3] presented the first- and second-order cross sections using the Walsh generalized function approach, later published by Gill and Walsh [66]. This research also led to further refinement of the generalized function approach, where Walsh and Gill [67] obtained more detailed expressions for the first three orders of the electric field in backscatter mode. Zhang and Gill [68] extracted the nondirectional ocean wave spectra by applying Howell's algorithm to the bistatic cross section formulation developed by Gill, obtaining results comparable to the monostatic case. This method, as explained, relied on linearizations to proceed with the inversion. To the author's knowledge, until now a nonlinear extraction method has not been devised for the extraction of directional ocean wave spectra from bistatic HF radar data.

1.3 Scope of the Thesis

As briefly explained in the end of Section 1.1, a nonlinear approach to the directional ocean wave extraction from bistatic HF radar data is proposed. This technique is founded on the work by Shahidi and Gill [1], where a change of variables is applied to reduce the monostatic second-order cross section expression. To contextualize the present research, this first chapter introduces the motivation for this work, and presents an overview of the state of the technology and the evolution of the extraction techniques.

In Chapter 2, the basic theoretical information required to understand the work of the thesis is presented. The main goal of the second chapter is to familiarize the

reader with the topic, introducing the mathematical concepts behind the next steps of the thesis. In order to introduce the measurement to be extracted, the basics of ocean wave generation and ocean wave spectrum model are discussed. Later in this chapter, the bistatic radar cross section equations are detailed and the scattering mechanisms involved are discussed.

Chapter 3 introduces the nondirectional ocean wave spectrum extraction technique from the bistatic second-order cross section, previously applied in [1] to the monostatic case. The extraction process is based on a simplification of the second-order bistatic cross section obtained by Gill and Walsh [69]. The process involves a change of variables to a domain that allows the simplification of the second-order cross section by applying the sifting property of the Dirac delta function. This chapter also explores particulars of the bistatic geometry that impact the simplification process. The extraction technique is then presented. This involves a discussion of the extraction methodology and the presentation of results for the noiseless case. In this work, the Longuet-Higgins directional factor is assumed for the extraction, but no specific model is assumed for the nondirecitonal spectrum. A good level of accuracy is achieved in the extraction. This provides a proof-of-concept for the technique, which is necessary before proceeding to a more complex situation, where not only the second-order cross section, but also first-order interactions and noise are considered.

The objective of Chapter 4 is to apply the method to a more realistic situation, where both first-order peaks and noise are present. First, the method is applied to the cross section including first- and second-order scatterings, but without any noise. Then, white Gaussian noise is added to the received radar signal in the time domain. After obtaining the noise-contaminated power spectral density, the extraction method

is applied. A fair level of accuracy is obtained, even in extremely noisy scenarios.

In Chapter 5, the conclusions of the research presented in this thesis are summarized. Also, further work on the topic is suggested.

Chapter 2

Theoretical Background

2.1 Introduction

The main goal of this chapter is to provide fundamental information regarding both the ocean wave spectrum and the bistatic radar cross section of the ocean surface. These are central topics in the discussions of this thesis.

Before considering the fundamentals of the ocean wave spectrum, the basic underlying mechanisms of ocean wave generation need to be understood. By understanding the types of waves and how they are generated, the reader will be familiarized with the types of waves HF radars interact with. Then, the ocean wave spectrum can be studied in both its non-directional and directional characteristics, and a model for each of them may be presented.

Once the fundamentals of the ocean wave spectra are known, the bistatic radar cross section is presented. First, the geometry of this radar configuration is presented, as well as how this configuration affects the scattering and, consequently, the received

radar information. Then, the cross sections for the first two orders of scattering are presented. These cross sections are central to the thesis, since it is from these equations that the ocean wave spectrum can be extracted.

2.2 Ocean Waves

2.2.1 Ocean Wave Classification

As stated by Massel [12], the ocean and atmosphere form a coupled thermodynamic system, exchanging mass, energy and momentum on their interface. This implies that any forcing of one fluid over the other will generate a response that will change the interfacial conditions of the system. In the case of the ocean-atmosphere system, waves are the responses from the ocean due to external forces.

According to Kinsman [11], there are several ways to classify ocean waves. One method, presented by Munk [2] and similar to the one presented by Kinsman, classifies waves according to their periods, or, reciprocally, their frequencies. In this classification, there are seven types of waves: capillary, ultra-gravitational, ordinary gravitational, infra- gravitational, long-period, ordinary tide and transtidal waves. Figure 2.1 shows the relative energy distribution of each class of waves, as well as their period bands.

As explained, for example, by Kinsman [11], in general, ocean waves are dispersive. This means that the phase velocity of these ocean waves will be dependent on their wavelengths. This establishes a relationship between angular frequency and wavelength of the waves, known as the *dispersion relation*. Knowing the dispersion

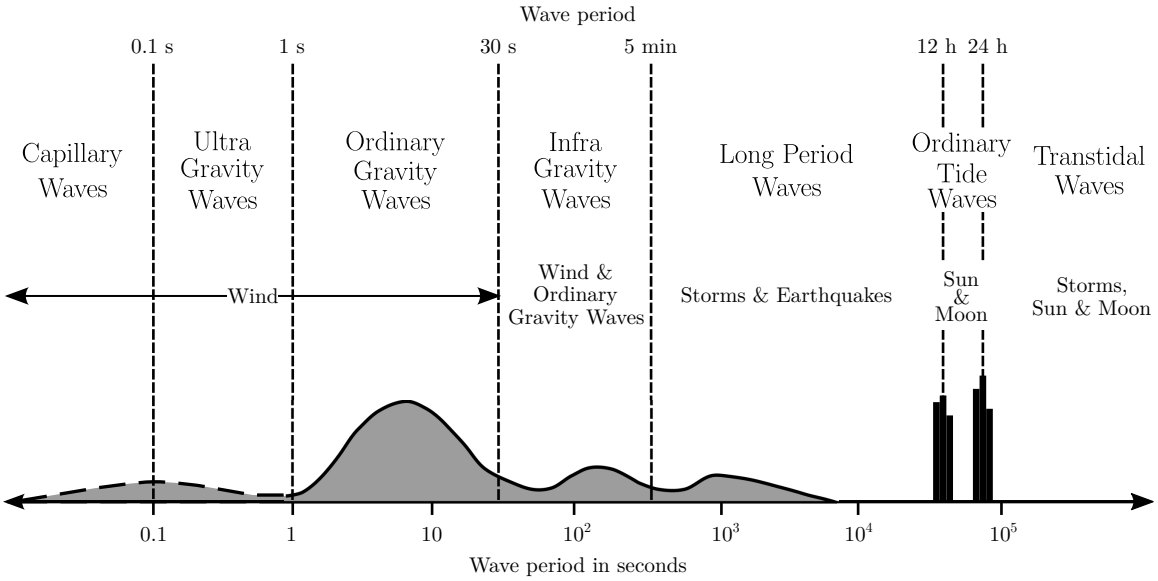

Figure 2.1: Classification of ocean waves according to wave period, with relative energy amplitude and generating forces for each type of wave. Adaptation from original by Munk in [2]

relation for ocean waves, it is possible to infer their wavelength if their period is known. As described, for example, by Phillips [70], the dispersion relation of ocean surface waves can be written as

$$\omega^2 = gK\left(1 + \gamma\frac{K^2}{g}\right)\tanh(Kh), \tag{2.1}$$

where g is the acceleration due to gravity, K is the magnitude of the ocean wave's wave-number, ω is the angular frequency of the ocean wave, γ is the ratio between the surface tension and water density, and h is the depth of the ocean.

Observing (2.1), a balance between the terms of the sum in parentheses can be identified. At wave-numbers $K < \sqrt{\frac{g}{\gamma}}$, the restoring force for the ocean wave is predominantly gravitational, whereas for waves with $K > \sqrt{\frac{g}{\gamma}}$ the restoring force is

primarily surface tension. This description matches with the proposed classification in Fig. 2.1, where the first case comprises the waves known as *gravitational (or gravity) waves*, while waves in the second case are classified as *capillary waves*.

Another classification can be made regarding the hyperbolic tangent in (2.1). From its argument, waves can be classified according to the relationship between depth and wave-number, or alternatively, wavelength, since $K = \frac{2\pi}{\lambda}$, where λ is the wavelength of the ocean wave. When $Kh >> 1$, in other words, if the water depth is much larger than the wavelength, the waves are called *deep water waves*. Conversely, if $Kh \approx 0$, this means that the depth is much smaller than the wavelength, therefore these waves are called *shallow water waves*. If neither of these conditions is satisfied, the wave is said to be of intermediate depth.

Throughout this thesis, the considered scenario is of deep water gravity waves. Mathematically, this situation can be described as $K << \sqrt{\frac{g}{\gamma}}$ and $Kh >> 1$. Assuming both conditions, (2.1) can be rewritten as

$$\omega^2 = gK. \tag{2.2}$$

This is an important condition, since most of the energy in the ocean surface is concentrated in this wave class. From a wavelength-wave period perspective, (2.2) can be rewritten as

$$\lambda = \frac{g}{2\pi}T^2, \tag{2.3}$$

where T is the wave period. Taking the relationship described by (2.3) and comparing to the wave periods in the classification proposed by Munk and expressed in Fig. 2.1, it may be inferred that deep water gravity waves have wavelengths between 1.56 and 1405 m. As a matter of comparison, HF radars, depending on their operating

frequency, have transmission wavelengths between 10 and 100 m, while microwave radars have wavelengths between 25 mm and 30 cm, which are comparable at the lower end to capillary waves. Given the Bragg scattering mechanism, alluded to in Section 1.1, the HF radar is much better equipped to measure ocean surface gravity waves, as compared to microwave radars.

As can easily be observed, waves with different wavelengths coexist in a wave field, often being superimposed and usually transferring energy between themselves. Also, a wave field is not independent of its surroundings or of waves generated by previous or distant winds. Therefore, another classification arises, with these waves being either classified as *sea* or *swell*.

A wave system can be classified as a *sea* if the waves are generated by local winds. However, when these waves gain enough energy to move out of their original wave fields, they are classified as *swell*. Swell usually has longer wavelengths compared to local seas, and sea waves travel on the top of swells. Understanding the difference between sea and swell is important to comprehend the terminology used in wave forecasting. For example, the expression "sea-state" refers to waves that were generated by local winds, and does not consider swells.

Ocean waves are also classified according to their generating or restoring forces. Massel [12] presents six classes of waves with respect to their generating/restoring forces:

- **Sound waves**, generated by the compressibility of the fluid. In the case of the ocean, sea water is often considered an incompressible fluid or as having extremely low compressibility values. Therefore, ocean sound waves are very

small and are usually neglected.

- **Capillary waves** that, as previously explained, have surface tension as their restoring force. As explained, for example, by Lamb [71], the maximum wavelength for a capillary wave is 1.73 cm.

- **Surface gravity waves** that, as their name suggest, are gravity waves that occur on the surface. This is the type of wave that was previously explained in Munk's classification.

- **Internal gravity waves**, are gravity waves that happen at the interface of stratified fluids, such as sea water. The stratification happens due to differences in density inside the fluid. More information on internal waves can be found in Cushman-Roisin and Beckers [72].

- **Planetary waves**, generated by the equilibrium of the potential vorticity due to changes in depth and latitude. These waves are also known as Rossby waves. This class of waves, as well as other types that depend on the Earth's rotation, can be found in Chapter 9 of the book by Cushman-Roisin and Beckers [72].

Alternatively, Fig. 2.1 presents another classification according to the generating forces, showing the overlap with the classification according to the wave period. In the case of surface gravity waves, wind and gravity are the main forces involved in their generation and restoration processes.

2.2.2 Wind Wave Generation and Development

One important topic regarding ocean surface gravity waves is the process of wave generation. As previously stated, different types of waves are generated by different forces and phenomena, such as gravitational fields for tide and transtidal waves, or storms and earthquakes for long period waves. In the case of surface gravity waves, the wind plays the key role in their generation, while gravity acts as a restoring force.

According to Phillips [70] and Massel [12], the development of a more widely accepted wind wave generation theory came in the 1950's, especially after the publication of two papers, one by Phillips [73], and another by Miles [74], both published in 1957 in the Journal of Fluid Mechanics. Even though the research behind these papers was developed independently, the two proposed mechanisms are in fact complementary and are also referred to as the *Phillips-Miles mechanism*.

The Phillips-Miles mechanism can be described in a thought experiment, in which each part of the theory can be understood. At first, a flat air-sea interface, without any perturbation from each of the fluids is considered. If pressure variations are introduced into the atmosphere and transmitted to the air-sea interface, these pressure variations will resonate on the interface itself, due to the fact that this is a coupled thermodynamic system. These pressure variations cause small ripples in the ocean surface as a response to the initial pressure variations. This process is known as the *Phillips' resonance mechanism*.

Phillips' theory can successfully explain the initial growth of the waves, but cannot describe their further growth properly. The waves described by Phillips' theory are most likely capillary waves, and would propagate and dissipate through the ocean

surface using its surface tension if these pressure variations were to cease. However, if a parallel shear flow is applied over the rippled surface, energy will be transferred from the wind to these small ripples at a much higher rate than Phillips' theory would predict. The waves affected by this parallel shear flow would rapidly grow in size and speed, which would change their restoring forces from surface tension to gravity, as indicated by (2.1). The process responsible for wave growth due to a shear wind flow is known as *Miles' shear flow mechanism*.

From observations such as the ones made by Elliott [75] and Hasselmann *et al.* [76], it is possible to see that in some cases, waves travel faster than the wind that generated them. According to Stewart [77], this is due to nonlinear interactions between waves in the wave field. Some theories were developed on how this nonlinear interaction happens, and some of them are explained in Chapter 13 of [11], or, more recently, in section 6.2.2 of Massel [12] for deep water waves. One of the explanations is presented by Hasselmann [78, 79, 80] , arguing that one of the nonlinear processes that occurs between ocean waves is the energy transfer from shorter to longer waves. Stewart [77] shows, using the model presented by Pierson and Moskowitz [19], that waves with the highest energy in a wave field travel at phase speeds 14% higher than the wind speed blowing at 19.5 m from the ocean surface. These waves, however, cannot grow indefinitely. As described by Massel [12], when waves meet some criteria, such as their wave height to wavelength ratio reaching 1/7 or their particle velocity at the crest being equal to the wave phase speed, they start to destabilize, becoming what are known as breaking waves. The detailed theory on how and when the waves break can be found in Massel [81].

What was presented in this section is merely an outline of the Phillips-Miles theory

with some additions, presented in order to familiarize the reader with the underlying mechanisms of the object of study, necessary to understand further observations in both the ocean wave spectrum and in the HF radar mapping of the ocean surface. However, the purpose here has not been to present the mathematical development of the theory, but simply to provide a more intuitive approach. A more detailed explanation, as well as the more recent additions to the theory, can be found in the work by Massel [12].

2.2.3 The Ocean Wave Spectrum

As mentioned in Section 1.1, the directional ocean wave spectrum is one of the most holistic measurements of the ocean surface. While observing a given wave field, particular waves in it will have different wavelengths that will be superimposed and interacting with each other. Due to the obvious difficulties of measuring each wave in a given field, spectral analysis will give more detailed information, such as the energy of waves at a given wavelength, and the direction in which these waves are propagating.

Consider the sea surface displacements from the mean level $\xi(\mathbf{r}, t)$, where $\mathbf{r}$ is a spatial vector in the horizontal plane defined as $\mathbf{r} = (x, y) = x\hat{\mathbf{i}} + y\hat{\mathbf{j}} = r\angle\underline{\theta_{\mathbf{r}}}$ and the wave-number vector is defined as $\mathbf{K} = (K_x, K_y) = K_x\hat{\mathbf{i}} + K_y\hat{\mathbf{j}} = K\angle\underline{\theta_{\mathbf{K}}}$. Assuming that the dispersion relations derived in Section 2.2.1 hold, it is possible to define a stochastic process $A(\omega, \theta_{\mathbf{K}})$, such that

$$\xi(\mathbf{r}, t) = \int_{-\infty}^{\infty}\int_{-\pi}^{\pi} \exp[j(\mathbf{K}\cdot\mathbf{r} + \omega t)]dA(\omega, \theta_{\mathbf{K}}). \tag{2.4}$$

This expression is analogous to the one presented by Pierson [13]. From Equa-

tion (2.4), the autocorrelation of sea surface displacements can be written in its simplified form as [12]

$$R(\mathbf{\Delta r}, \tau) = \int_{-\infty}^{\infty} \int_{-\pi}^{\pi} \exp[j(\mathbf{K} \cdot \mathbf{\Delta r} + \omega\tau)] \hat{\Psi}(\omega, \theta_{\mathbf{K}}) d\omega d\theta_{\mathbf{K}}, \tag{2.5}$$

where $\hat{\Psi}(\omega, \theta_{\mathbf{K}})$ is the frequency-dependent directional spectral density function of the surface waves, also known as the *frequency-dependent directional ocean wave spectrum*, and $\mathbf{\Delta r} = (\Delta x, \Delta y)$.

Clearly the directional ocean wave spectrum in Equation (2.5) is dependent on both direction and frequency of the ocean waves. Another common way to express the directional ocean wave spectrum is with respect to wave-number. For deep water gravity waves, where the dispersion relation is given by (2.2), the autocorrelation function with respect to the wave-number directional ocean wave spectrum $\hat{S}(K, \theta_{\mathbf{K}})$ is given by [12]

$$\begin{aligned} R(\mathbf{\Delta r}, \tau) &= \int_{-\infty}^{\infty} \int_{-\infty}^{\infty} \exp[j(\mathbf{K} \cdot \mathbf{\Delta r} + \sqrt{gK}\tau)] \hat{S}(\mathbf{K}) dK_x dK_y \\ &= \int_{-\infty}^{\infty} \int_{-\pi}^{\pi} \exp[j(\mathbf{K} \cdot \mathbf{\Delta r} + \sqrt{gK}\tau)] \hat{S}(K, \theta_{\mathbf{K}}) K dK d\theta_{\mathbf{K}}. \end{aligned} \tag{2.6}$$

By observing (2.5) and (2.6), it is possible to deduce a relation between $\hat{\Psi}(\omega, \theta_{\mathbf{K}})$ and $\hat{S}(K, \theta_{\mathbf{K}})$. Since frequency and wave-number are related by the dispersion relation, (2.2) can be used to deduce the relationship in the case of deep water gravity waves. From (2.2),

$$KdK = 2\frac{\omega^3}{g^2} d\omega, \tag{2.7}$$

which implies that

$$\hat{S}(K, \theta_{\mathbf{K}}) = \frac{g^2}{2\omega^3} \hat{\Psi}(\omega, \theta_{\mathbf{K}}). \tag{2.8}$$

2.2.3.1 Non-Directional Ocean Wave Spectrum and Directional Factor

In most cases, it is desirable to analyze the power density spectral information independent of the direction to which the waves are propagating, for example in the case of single point measurements. Considering the autocorrelation function $R(\mathbf{\Delta r}, \tau)$ of a single point, i.e. making $\Delta r = (0, 0)$,

$$R(\tau) = \int_{-\infty}^{\infty} \int_{-\pi}^{\pi} \hat{\Psi}(\omega, \theta_{\mathbf{K}}) e^{j\omega\tau} d\omega d\theta_{\mathbf{K}} \tag{2.9}$$

If ω is considered independent of the wave direction $\theta_{\mathbf{K}}$, the expressions for the directional spectra can be written as

$$\hat{\Psi}(\omega, \theta_{\mathbf{K}}) = \tilde{\Psi}(\omega) D(\theta_{\mathbf{K}}) \tag{2.10}$$

where $\tilde{\Psi}(\omega)$ is the non-directional ocean wave spectrum and $D(\theta_{\mathbf{K}})$ is the directional spreading function, or directional factor.

The directional spreading function is chosen such that,

$$\tilde{\Psi}(\omega) = \int_{-\pi}^{\pi} \hat{\Psi}(\omega, \theta_{\mathbf{K}}) d\theta_{\mathbf{K}}.$$

This expression implies that

$$\int_{-\pi}^{\pi} D(\theta_{\mathbf{K}}) d\theta_{\mathbf{K}} = 1,$$

a fundamental characteristic of the directional spreading function.

Substituting (2.10) in (2.9), and integrating over wave direction, the autocorrelation expression becomes

$$R(\tau) = \int_{-\infty}^{\infty} \tilde{\Psi}(\omega) e^{j\omega\tau} d\omega. \tag{2.11}$$

From this expression it is possible to conclude that the autocorrelation function at a single point and its frequency-dependent non-directional ocean wave spectrum are Fourier transform pairs. Therefore, the ocean wave spectrum of a single-point measurement can be determined by the Fourier transform of the autocorrelation function. That is

$$\tilde{\Psi}(\omega) = \frac{1}{2\pi} \int_{-\infty}^{\infty} R(\tau) e^{-j\omega\tau} d\tau. \tag{2.12}$$

Since the directional spreading function is the same for both the frequency-dependent and the wave-number directional ocean wave spectra, (2.8) can be rewritten as

$$\tilde{S}(K) = \frac{g^2}{2\omega^3} \tilde{\Psi}(\omega).$$

By using this relationship, it is possible to obtain the non-directional wave-number ocean wave spectrum. It is important to note, however, that from a property of the Fourier transform, $\tilde{\Psi}$ and $\tilde{S}(K)$ are even functions. Due to their symmetry, these functions are called symmetric ocean wave spectra. These expressions are more commonly used in theoretical considerations [11, 12], while in practice, non-symmetric ocean wave spectra are more commonly used. These spectra are defined as

$$\Psi(\omega) = \begin{cases} 2\tilde{\Psi}(\omega), & \omega \geq 0 \\ 0, & \text{otherwise,} \end{cases} \tag{2.13}$$

and

$$S(K) = \begin{cases} 2\tilde{S}(K), & K \geq 0 \\ 0, & \text{otherwise.} \end{cases} \tag{2.14}$$

Throughout this thesis, the reader will find $\hat{S}(K, \theta_{\mathbf{K}})$ being referred to simply as the "directional ocean wave spectrum", or $S(K)$ as the "non-directional ocean wave

spectrum". Terms such as "wave-number" and "non-symmetric" will be dropped from now on to facilitate the writing. However, all results herein presented can be easily converted to a frequency-dependent directional ocean wave spectrum.

2.2.3.2 Spectral Moments and Traditional Meteorological Measurements

With regards to the non-directional ocean wave spectrum, spectral moments are very important measurements. The r^{th}-moment of the spectrum is defined as

$$M_r = \int_0^\infty \omega^r \Psi(\omega) d\omega \tag{2.15}$$

Using (2.2) and (2.8) in (2.15), the form the spectral moments for the wave-number spectrum can be written as

$$M_r = (\sqrt{g})^r \int_0^\infty \left(\sqrt{K}\right)^{r+2} S(K) dK. \tag{2.16}$$

One spectral moment of particular interest is the zero-moment of the spectrum. It can be understood as the variance of the ocean wave spectrum [12], and it is important for some measurements of the ocean behaviour. Making $r = 0$, the variance of the ocean wave spectrum can be written as

$$\text{Var}[S(K)] = M_0 = \int_0^\infty K S(K) dK. \tag{2.17}$$

The zero-moment of the spectrum is particularly important because, by using it, it is possible to obtain the significant wave height of a patch of the ocean.

The significant wave height $\overline{H_{1/3}}$ is one of the measurements used in a more traditional approach to physical oceanography, such as peak wave period, and mean wave direction. The significant wave height is defined as the height of the highest 1/3 of

the waves, and in the past it was empirically obtained [77]. Later, however, a more theoretical method to obtain the significant wave height was developed. By using the variance of the spectrum, $\overline{H_{1/3}}$ can be defined as

$$\overline{H_{1/3}} = 4\sqrt{M_0} = 4\sqrt{\int_0^\infty KS(K)dK} = 4\sqrt{\int_0^\infty \Psi(\omega)d\omega}. \tag{2.18}$$

Other traditional measurements that can be obtained from the non-directional ocean wave spectrum are the mean and peak wave periods. The mean wave period $\overline{T}$ can be easily calculated using the spectral moments:

$$\overline{T} = 2\pi\frac{M_0}{M_1}. \tag{2.19}$$

As for the peak wave period, it is necessary to know the frequency, or the wave-number of the spectrum peak, respectively ω_p and K_p. Once this peak is identified, the peak wave period T_p can be calculated as

$$T_p = \frac{2\pi}{\omega_p} = \frac{2\pi}{\sqrt{gK_p}} \tag{2.20}$$

The last of the mentioned physical oceanography measurements used to describe wave fields is the mean wave energy direction. The mean wave energy direction $\bar{\theta}$, or simply mean wave direction, as the name suggests, is the mean direction in which the waves are propagating. In some conditions, this mean wave direction can be taken to approximate the direction in which the wind is blowing.

2.2.3.3 Spectral Models

Even though several factors contribute to the generation and development of a wave field, the overall shape and properties of ocean wave spectra are not entirely random.

Massel [12] provides a summary of such characteristics, such as a distinct peak, with the spectrum decreasing to both sides, but faster towards the lowest wave-numbers. The location and height of the peak are related to the amount of energy that is provided to the spectrum.

The spectral region farther from the peak and towards higher wave-numbers is known as the *saturation range*. Within this range, the ocean wave spectrum follows an inverse fourth- [82] or fifth-order [70] decay. The saturation range indicates a balance between the input energy to the wave field — in this case, the wind — and dissipative mechanisms, such as the breaking of the waves. Section 3.2.2 of Massel [12] deals with the saturation range in more detail.

Due to the generally well-defined shape of the ocean wave spectrum, many mathematical models have been developed in order to describe the spectral distribution of the ocean waves. Among these models, the Pierson-Moskowitz (PM) model [19] is one of the most commonly used. Here, a brief explanation of the PM model will be given. Other spectral models can be found in Massel [12].

Regarding the shape of the directional spreading function, however, not much is known as compared to the non-directional spectrum. However, this shape can be described by four main types of functions: cosine-power, hyperbolic functions, exponential and double peak models. Among the cosine-power models, the Longuet-Higgins spread function [83] is one of the most well known. Later in this section a short description of this model will be given. Similar to the non-directional spectral models, other models can be found in Massel [12].

Pierson-Moskowitz Model The Pierson-Moskowitz spectral model, also referred as the PM spectrum, along with the JONSWAP spectrum proposed by Hasselmann *et al.* [76], is one of the most famous spectral models in its field. As the title of the report in which it was first published suggests, the similarity theory of S. A. Kitaigorodskii [4] is one of the key elements of this spectral model.

In his paper, Kitaigorodskii proposed that the spectral density function of the sea can be described as a function of the wave frequency ω, acceleration due to gravity g, friction velocity u_* of the wind over the water surface, and the wind fetch X_w. Symbolically,

$$\Psi(\omega) = F(\omega, g, u_*, X_w).$$

A fully-developed sea or, in other words, a sea in which the energies provided by the wind and absorbed and dissipated by the waves are in equilibrium, is by definition independent of fetch and of the time over which the wind was blowing over the surface [84]. In this situation, Kitaigorodskii proposed that the spectrum of a fully-developed sea could be written as

$$\Psi(\omega) = g^2\omega^{-5}\overline{F}\left(\frac{u_*\omega}{g}\right), \tag{2.21}$$

where $\overline{F}$ is a dimensionless function that is used for consideration of similarity theory. In order to determine which function would be appropriate for $\overline{F}$, experimental data was considered. Among the quantities considered in (2.21), however, friction velocity cannot be readily measured. Kitaigorodskii explicitly states that the wind direction cannot be used directly, but rather that it should be calculated using the Charnock-Ellison equation for friction velocity [85], written as

$$\frac{U_z}{u_*} = \frac{1}{C}\log_{10}\left(\frac{gz}{{u_*}^2}\right) + 11.0,$$

where $x \approx 0.4$ and U_z is the average wind velocity measured at the level z.

Using the expression provided by Kitaigorodskii, field data for fully developed seas obtained by Moskowitz *et al.* [18], and the saturation range proposed by Phillips [86], Pierson and Moskowitz developed the spectral model that has come to be known as the Pierson-Moskowitz spectrum, abbreviated as the PM spectrum. The PM spectrum can be written as

$$\Psi(\omega) = \alpha g^2 \omega^{-5} \exp\left[-\beta \left(\frac{g}{\omega U_{19.5}}\right)^4\right], \tag{2.22}$$

or,

$$S(K) = \frac{\alpha}{2} K^{-4} \exp\left[-\beta \left(\frac{1}{U_{19.5}}\sqrt{\frac{g}{K}}\right)^4\right], \tag{2.23}$$

α and β being dimensionless constants, where $\alpha = 8.1 \times 10^{-3}$ and $\beta = 0.74$. Figure 2.2 shows the Pierson-Moskowitz non-directional ocean wave spectrum for different wind speeds.

It must be observed that Kitaigorodskii's suggestion to use Charnock-Ellison's friction velocity was not followed in (2.22) and (2.23). According to Pierson and Moskowitz [19], the use of the Charnock-Ellison's friction velocity would add more assumptions to the spectrum, and any imprecision due to the use of the anemometer-measured velocity would introduce other factors, that are not treated in the report. It must be observed, however, that even without using friction velocity in its formulation, the PM spectral model has become the *de facto* standard for fully developed seas, even though this assumption has been questioned by later research [12].

Longuet-Higgins Directional Factor This directional factor was first proposed by Longuet-Higgins *et al.* [83] in 1961 as an extension of the cosine-power model

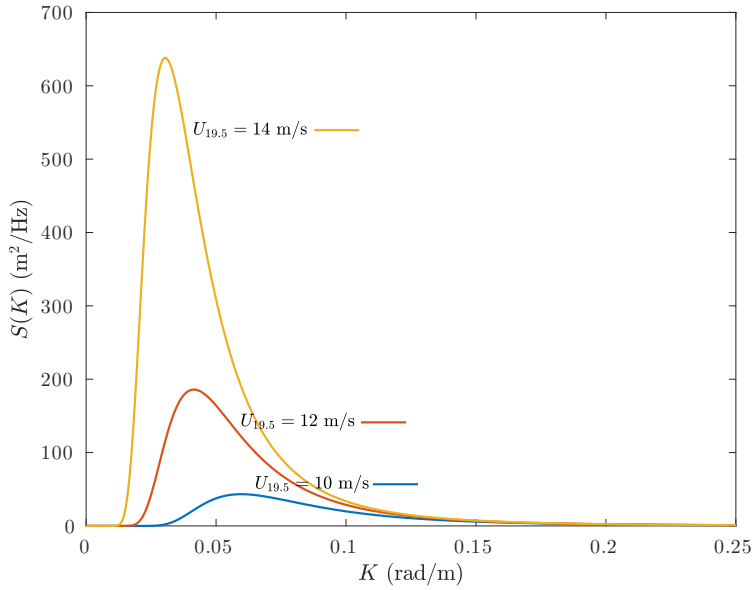

Figure 2.2: Pierson-Moskowitz non-directional spectral model for different wind speeds

proposed by Pierson *et al.* [87]. The cardioid-shaped Longuet-Higgins directional factor can be written as

$$D(\theta_{\mathbf{K}}, s) = \frac{2^{2s+1}}{\pi} \frac{\Gamma^2(s+1)}{\Gamma(2s+1)} \cos^{2s}\left(\frac{\theta_{\mathbf{K}} - \bar{\theta}}{2}\right), \tag{2.24}$$

where s is known as the spreading factor, and Γ is the Gamma function presented, for example, in [88].

Figure 2.3 shows the spectrum described in (2.24), for various values of the spreading factor s and a mean wind direction of 0°. A change in the mean wind direction $\bar{\theta}$ changes the direction of the maximum of the directional spreading function, and the effect of changing $\bar{\theta}$ is not shown in the Figure 2.3, since it only results in a rotation of the directional spreading function about the origin.

Clearly, the spreading factor s in (2.24) plays a large role in the directional function

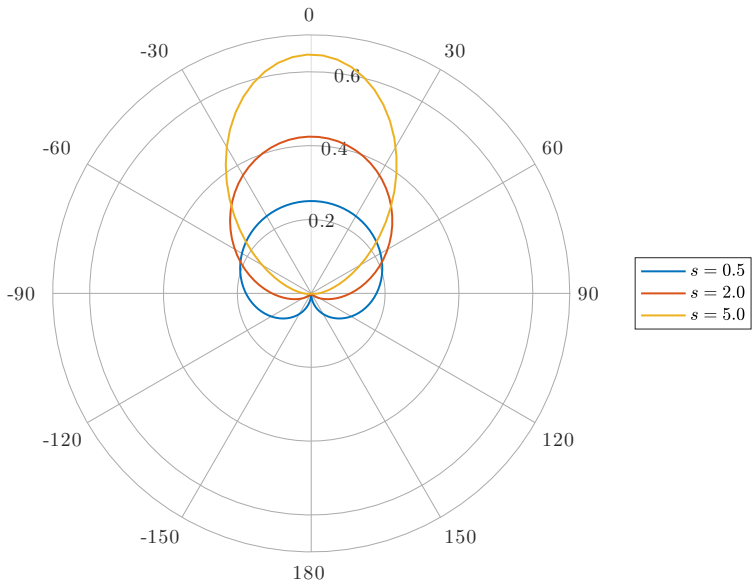

Figure 2.3: Longuet-Higgins directional spreading function for different spreading factors.

and is found to be a value dependent on the wave frequency. In the literature, however, $s = 2$ is largely considered a reasonable value of the spreading factor [3].

Directional Ocean Wave Spectrum By combining the Pierson-Moskowitz non-directional spectrum and the Longuet-Higgins directional spreading function, it is possible to simulate the directional spreading function. Analogous to (2.10), it is possible to write the wave-number directional ocean wave spectrum in terms of a directional spreading function and a non-directional factor. This is written as

$$\hat{S}(K, \theta_{\mathbf{K}}) = \tilde{S}(K) D(\theta_{\mathbf{K}}). \tag{2.25}$$

Figure 2.4 shows the directional ocean wave spectrum generated by the combination of the PM spectrum and the Longuet-Higgins directional factor, for a wind speed $U_{19.5} = 12$ m/s, mean wind direction $\bar{\theta} = 0°$, and spreading factor $s = 2$.

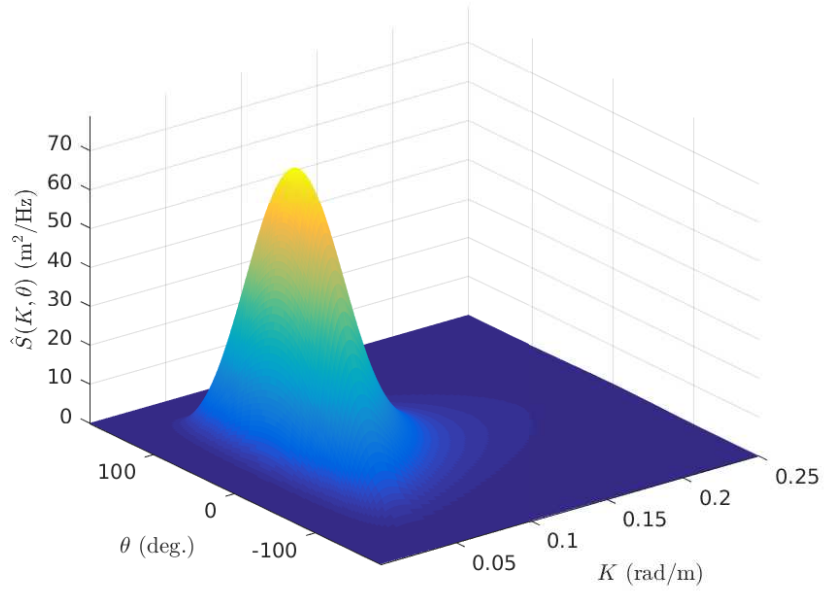

Figure 2.4: Directional ocean wave spectrum generated by a combination of the Pierson-Moskowitz spectrum and the Longuet-Higgins directional spreading function. Transmitter frequency $f_o = 13.385$ MHz, bistatic angle $\phi = 30°$, transmitter look direction $\theta_{01} = 60°$, wind speed $U_{19.5} = 12$ m/s, spreading factor $s = 2$, and wind direction $\theta_w = \bar{\theta} = 0°$.

2.2.4 Wave-Wave Interaction

As explained in previous sections, the waves on the ocean surface described by the directional ocean wave spectrum $\hat{S}(K, \theta_{\mathbf{K}})$ interact with each other, resulting in composite waves. The wave vector for these composite waves is given by

$$\mathbf{K} = \pm\mathbf{K}_1 \pm \mathbf{K}_2 \pm \cdots \pm \mathbf{K}_n,$$

where $\mathbf{K}$ is the wave vector of a nth-order wave, resulting from the combination of n first-order waves. Therefore, the ocean surface displacement can be expressed as

$$\xi(\mathbf{r},t) = \sum_{i=1}^{\infty} {}_i\xi(\mathbf{r},t), \tag{2.26}$$

where each ${}_i\xi(\mathbf{r},t)$ represents the surface displacement contribution given by ith-order waves. In terms of Fourier components, a ith-order surface displacement can be written as

$${}_i\xi(\mathbf{r},t) = \sum_{\mathbf{K},\omega} {}_iP_{\mathbf{K},\omega} \exp\left[j(\mathbf{K}\cdot\mathbf{r} + \omega t)\right], \tag{2.27}$$

with the Fourier components for the ith surface displacements ${}_iP_{\mathbf{K},\omega}$ being written as

$${}_iP_{\mathbf{K},\omega} = \sum_{\substack{\mathbf{K}=\sum_n^i \mathbf{K}_n \\ \omega=\sum_n^i \omega_n}} {}_H\Gamma \prod_{n=1}^{i} {}_1P_{\mathbf{K},\omega}. \tag{2.28}$$

In this expression, ${}_H\Gamma$ is known as *hydrodynamic coupling coefficient* [3].

Several different authors have proposed their own formulations for the hydrodynamic coupling coefficient, for both deep and shallow water waves. Due to the importance of this coefficient in the analysis of HF radar Doppler spectra, part of the work in this field was conducted by researchers in the HF radar community — see, for example, Weber and Barrick [89] and Walsh *et al.* [49].

In this thesis, only the first two orders of the Doppler spectrum will be studied. Since, by definition, there is no hydrodynamic interaction within first-order waves, their hydrodynamic coefficient is equal to unity. The second-order spectrum, on the other hand, has a hydrodynamic coupling coefficient for deep water gravity waves given by [49, 78–80]

$${}_H\Gamma = \frac{1}{2}\left[K_1 + K_2 + \frac{g}{\omega_1\omega_2}(K_1K_2 + \mathbf{K_1}\cdot\mathbf{K_2})\left(\frac{gK + (\omega_1+\omega_2)^2}{gK - (\omega_1+\omega_2)^2}\right)\right], \tag{2.29}$$

where $\omega_1 = \sqrt{gK_1}$ and $\omega_2 = \sqrt{gK_2}$, with K_1 and K_2 being the magnitudes of $\mathbf{K_1}$ and $\mathbf{K_2}$ respectively.

2.3 The Bistatic Radar Cross Section

According to the IEEE Standard for Definitions of Terms for Antennas (IEEE Std 145™-2013) [90], the term *scattering cross section* is defined as follows:

> *"For a scattering object and an incident plane wave of a given frequency, polarization, and direction, an area that when multiplied by the power flux density of the incident wave would yield sufficient power that could produce, by isotropic radiation, the same radiation intensity as that in a given direction from the scattering object."*

In other words, the scattering cross section is a measurement that, if multiplied by the power flux density of the incident wave, would result in the radiation intensity from the scattering object by isotropic radiation. The term *radar cross section*, on the other hand, is the portion of the scattering cross section with a specific polarization. It is an important measurement in radio oceanography because, if a mathematical form of the scattering cross section is derived, it is potentially possible to understand the contribution of each characteristic of the object to the received signal.

If the radar receiver is situated at the same position as the transmitter, or if it is at a position that is close enough to the source to be considered at the same position, the cross section is called *monostatic*. In a more general case, if the receiver is at any other position that is not the same as the receiver, the cross section is known as *bistatic* [90]. The difference between these two configurations can be seen in Figure 1.1.

In radio oceanography, the formulation of the radar cross section is a vital part of the process of extracting the directional ocean wave spectrum. Since the ocean

surface waves are themselves the "scattering objects", the directional ocean wave spectrum is a key element of the cross section, and, therefore, it can be obtained from the received electric field by means of mathematical inversion.

2.3.1 Scattering Mechanisms

When a radar signal is emitted towards the ocean by an onshore transmitter, it interacts with ocean waves of any order on the ocean surface. After a single scatter, a portion of the signal will be returned directly to the receiver by waves of different orders, while other portions may be scattered multiple times before reaching the receiver. Therefore, the received signal will contain information about multiple waves, which will introduce a continuum of Doppler shifts on the transmitted signal.

The received electric field is then a combination of parts of the transmitted signal that went through different paths before arriving at the receiver. Signals that have travelled through shorter paths will have higher energies compared to ones that have travelled through longer paths. Therefore, in general, the more interactions a radar signal has with the ocean, the lower is its mean energy at the receiver.

It is important to notice that most HF radar systems use vertical monopoles or dipoles at the receiver, which only allow the interrogation of vertically polarized radiation. This design approach is justified by the fact that horizontally polarized radiation in the HF band will quickly die out in surface wave propagation over the ocean [91]. Therefore, only vertically polarized radiation is considered throughout this thesis.

The interaction between the transmitted signal and ocean waves can occur in two

different ways: when the signal is scattered by a single nth-order wave, this interaction is said to be *hydrodynamic*, whereas when the signal is scattered by multiple first-order waves, the interaction is said to be *electromagnetic*. A combination of the two, when the signal is scattered by multiple nth-order waves is also possible. These interactions are also classified in orders, taking into account the number of bounces and the sequence of the waves from which the signal was scattered. Walsh and Gill [67] provide a thorough explanation of the scattering mechanisms, as well as the equations for each type of scattering up to third-order.

Another classification of these interactions can be given if the position of the scatters is also considered. If all the scatters occur at the same remote area of the ocean, the interaction is known as *patch scattering*, while if at least one scattering event occurs close to the transmitter or the receiver, the interaction is known as *foot scattering*.

In summary, the received electromagnetic signal $E^+_{0_n}$ at a time t from a scattering ellipse defined by t_0 can be analyzed up to its second-order scattering as [66]

$$E^+_{0_n}(t_o,t) = (E^+_{0_n})_{11}(t_o,t) + (E^+_{0_n})_{2P}(t_o,t) + (E^+_{0_n})_{2T}(t_o,t) + (E^+_{0_n})_{2R}(t_o,t), \quad (2.30)$$

where the terms on the right-side of Equation (2.30) are defined as follows:

- $(E^+_{0_n})_{11}$: First-order scattering, that is a first-order interaction (i.e. single bounce) between the transmitted signal and a first-order wave (i.e. a wave that was not generated by superposition).

- $(E^+_{0_n})_{2P}$: Second-order patch scattering, that is, a second-order effect that happens within the scattering patch over the ocean. It can be divided into two parts:

  - *Hydrodynamic*: A first-order interaction between the transmitted signal and a second-order wave (i.e. a wave that is formed by a superposition of two waves). It can be classified independently as a first-order scattering.
  - *Electromagnetic*: A second-order scattering (i.e. double bounce) between the transmitted signal and two first-order waves.

- $(E_{0_n}^+)_{2T}$: Second-order electromagnetic scattering with one of the first-order waves near the transmitter followed by one scatter from a first-order wave on the remote patch

- $(E_{0_n}^+)_{2R}$: Second-order electromagnetic scattering with one of the first-order waves near the receiver after one scatter from a first-order wave on the remote patch

From (2.30) and the definition of cross section, the total radar cross section at a particular Doppler shift ω_d up to second-order scattering can be written as

$$\sigma(\omega_d) = \sigma_{11}(\omega_d) + \sigma_{2P}(\omega_d) + \sigma_{2T}(\omega_d) + \sigma_{2R}(\omega_d), \tag{2.31}$$

where σ is the total cross section. The subscript of each of the terms in (2.30) and (2.31) indicates which type of scattering mechanism the term represents.

Throughout this thesis, only patch scattering up to second-order will be considered; therefore, σ_{2T} and σ_{2R} and any higher order scattering cross sections will be neglected.

2.3.2 Bistatic Geometry

To proceed to the analysis of the bistatic radar cross sections, the bistatic geometry needs to be understood. For the bistatic configuration, elliptical coordinates are the natural coordinates of the system. A detailed explanation regarding the use of elliptical geometry for each type of scattering in the bistatic radar configuration can be found in the thesis by Gill [3].

As previously mentioned, this present work will only deal with patch scattering up to second-order. Further information on both patch and foot scattering in the bistatic configuration can be found in Gill [3]. Figure 2.5 shows the geometry of an n^{th}-order patch scatter in the bistatic configuration after setting the coordinate origin at the transmitter, where $\boldsymbol{\rho}$ is the vector between transmitter (Tx) and receiver (Rx); $\boldsymbol{\rho_{0i}}$, the vector between the transmitter and the i^{th} scatter, with $1 \leq i \leq n$; $\boldsymbol{\rho_{n0}}$, the vector between the last scatter and the receiver; $\mathbf{N}$, the unit vector normal to the ellipse at the scattering patch ($\mathbf{N} = 1\underline{/\theta_{\mathbf{N}}}$); $\mathbf{T}$, the tangent to the ellipse at the scattering patch; $\mathbf{K}$, the resulting wave vector, given by

$$\mathbf{K} = \sum_{i=1}^{n} \mathbf{K_i},$$

where $\mathbf{K_i}$ are the wave vectors for each wave from which the transmitted signal has scattered (electromagnetic coupling) or each first-order wave in a composite wave (hydrodynamic coupling); θ_{0i} is the direction of the vector between the transmitter and the i^{th} scatter; ϕ, the bistatic angle; and $\theta_{\mathbf{N}}$ is the normal to the scattering ellipse at the point of scatter.

Observing the properties of an ellipse, the convenience of using this coordinate system becomes clear. Two properties of the ellipse of interest in this analysis are the

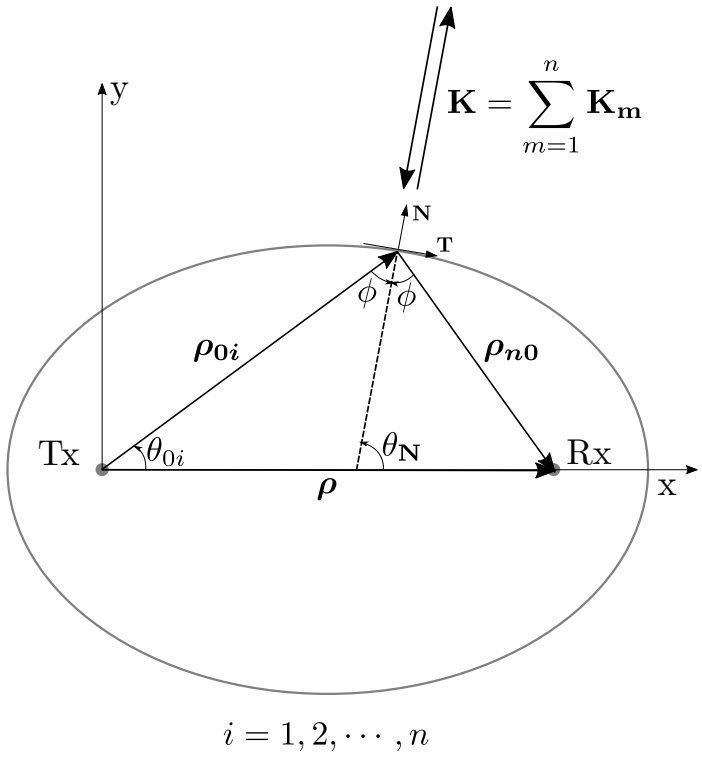

Figure 2.5: Patch scattering geometry in bistatic configuration (Adapted from Gill [3])

reflection property and the angle bisection property.

The reflection property of an ellipse states that, if a ray of light is emitted from one focus of the ellipse and reflects on its inner surface, the ray will always pass through the other focus [92]. Considering the geometry of the bistatic patch scattering presented in Fig. 2.5, it can be observed that, if the coordinates are set such that the transmitter and the receiver are both on the foci of the ellipse, and the scattering patch is always on the surface of the ellipse, there will always be part of the signal that will bounce on the scattering patch and be reflected to the receiver. If the reflection property is combined with the fact that the sum of the distances between the foci and any point of the ellipse is constant, and that the speed of an electromagnetic wave is constant

within an isotropic medium, it can be said that a signal transmitted from one of the foci of the ellipse and scattered by any point on its boundary will arrive at the receiver at the same time. For a bistatic radar, this ellipse is known as the *scattering ellipse*. Therefore, the scattering patch will be defined as the region of the scattering ellipse that is being observed by the receiver. The area of this patch will be a function of the beamwidth of the receiver, and if the scattering patch is sufficiently narrow, the received signal can be treated as coming from a single representative point on the scattering ellipse [3]. In this work, a bistatic narrow beam radar is considered, meaning that the aforementioned consideration can be made. For a pulsed narrow beam radar in bistatic configuration, the width of the scattering patch $\Delta\rho_s$ and the area of the scattering patch can be respectively defined as

$$\Delta\rho_s = \frac{c\tau_o}{2}, \tag{2.32}$$

and

$$A_P = \Delta\rho_s(\rho_{n0}\theta_{HPBW}), \tag{2.33}$$

where τ_o is the pulse width, c is the speed of light, ρ_{n0} is the distance between the transmitter and the scattering patch, and θ_{HPBW} is the half-power beamwidth of the receiver antenna.

Another important property to be observed is the angle bisection property. This property states that if an ellipse with foci F_1 and F_2 is given, the local normal to the ellipse at any point P bisects the angle $\angle F_1PF_2$. From Fig. 2.5, it is clear that the vector $\mathbf{N}$ is the normal to ellipse at the scattering point P, and that its extension, represented by the dashed line, divides the angle between $\boldsymbol{\rho}_{\mathbf{0i}}$ and $\boldsymbol{\rho}_{\mathbf{n0}}$ in half. In a bistatic geometry, each half of this angle is known as the *bistatic angle*,

written as ϕ. The bistatic angle is one of the main characteristics of the bistatic configuration, allowing for the analysis and determination of the direction of the waves being observed by such radar structure.

As the name suggests, in a patch scattering scenario all the scatters are located within the scattering patch. In this case, since the scattering patch is sufficiently distant from the transmitter, the following assumptions can be made:

$$\boldsymbol{\rho_{01}} = \boldsymbol{\rho_{02}} = \cdots = \boldsymbol{\rho_{0n}}$$

and

$$\theta_{01} = \theta_{02} = \cdots = \theta_{0n}.$$

In patch scattering, therefore, θ_{01} is defined as the transmitter look direction.

Using basic properties of triangles, it is easy to arrive at the relationship between the normal angle $\theta_{\mathbf{N}}$, transmitter look direction θ_{01} and the bistatic angle. The relationship is written as

$$\theta_{\mathbf{N}} = \theta_{01} + \phi. \tag{2.34}$$

2.3.3 First-Order Bistatic Cross Section

As described by Gill [3], the first-order bistatic radar cross-section can be written as

$$\sigma_{11}(\omega_d) = 2^4 \pi k_o^2 \sum_{m=\pm 1} \hat{S}(m\mathbf{K}) \frac{K^{5/2} \cos\phi}{\sqrt{g}} \Delta\rho_s \, \mathrm{Sa}^2 \left[\frac{\Delta\rho_s}{2} \left(\frac{K}{\cos\phi} - 2k_o \right) \right], \tag{2.35}$$

where ω_d is the Doppler shift frequency in rad/s; k_o is the wave-number of the transmitted signal; m is a constant chosen such that

$$m = \begin{cases} 1 & \omega_d \leq 0 \\ -1 & \omega_d \geq 0 \end{cases}$$

$\Delta\rho_s$ is the width of the scattering patch, defined by Equation (2.32); and Sa is the sinc function, given by

$$\mathrm{Sa}(x) = \frac{\sin x}{x}.$$

The first-order waves that can be perceived by a radar in a bistatic configuration has the same direction as the vector normal to the ellipse $\mathbf{N}$. Therefore, the vector $\mathbf{K}$ can be defined as

$$\mathbf{K} = K\underline{/\theta_{\mathbf{N}}}. \tag{2.36}$$

This shows the importance of (2.34) in operating a bistatic radar. If the transmitter is a phased array, the beam can be steered in order to change $\theta_{\mathbf{N}}$ and, consequently, the direction of the observed waves.

In the first-order cross section, the magnitude of the observed wave-number at a given frequency ω_d follows the dispersion relation of the ocean waves, stated in (2.2) for deep water gravity waves. Using (2.2), the magnitude of the observed wave-number is given by

$$K = \frac{\omega_d^2}{g}. \tag{2.37}$$

Observing the argument of the sinc function in (2.35), it is evident that the ocean wave spectrum has a peak at

$$K_B = 2k_o \cos\phi, \tag{2.38}$$

or at the frequencies

$$\omega_B = \pm\sqrt{2gk_o \cos\phi}. \tag{2.39}$$

The maxima of the Doppler spectrum at these frequencies are known as *Bragg peaks*. Therefore, by changing the bistatic angle or the transmitter frequency, the ocean

wave frequency — or wave-number — of the peak energy of the Doppler spectrum also changes. This allows more versatility in the measurement of the ocean surface.

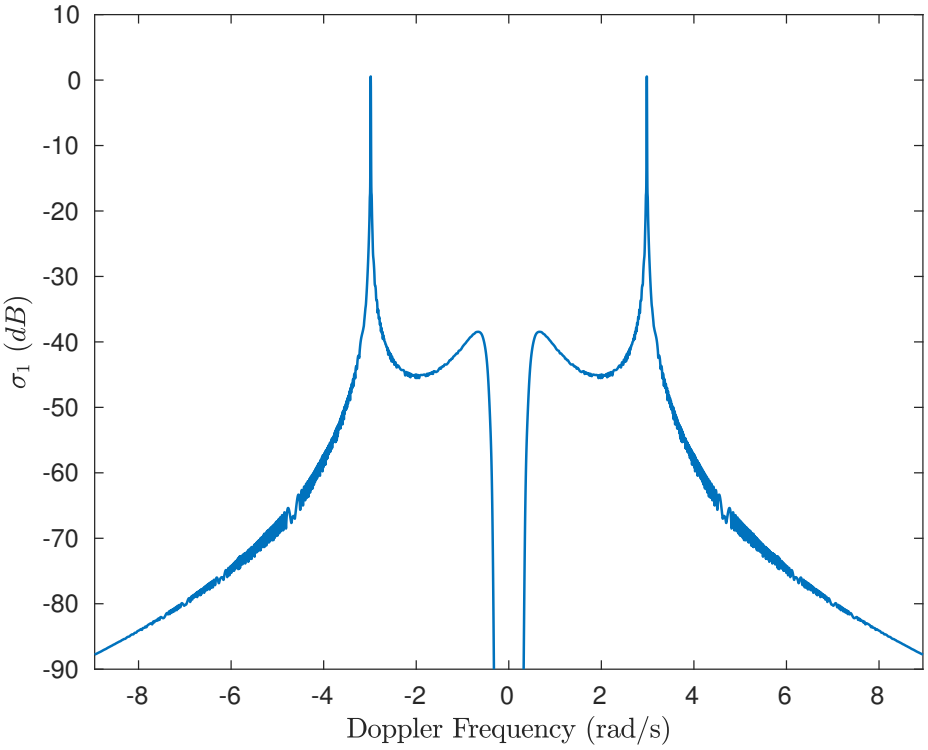

Figure 2.6: Simulated first-order bistatic cross section. Transmitter frequency f_o = 13.385 MHz, bistatic angle $\phi = 30°$, transmitter look direction $\theta_{01} = 60°$, wind speed $U_{19.5}$ = 12 m/s and wind direction $\theta_w = \bar{\theta} = 180°$. The two large maxima are the Bragg peaks.

Figure 2.6 presents a simulated first-order bistatic cross section, generated using (2.35) . The directional ocean wave spectrum is a combination of the Pierson-Moskowitz ocean wave spectrum, defined by (2.23), and the Longuet-Higgins directional spreading function, defined by (2.24).

It is important to notice that (2.35) uses the symmetric non-directional spectrum

$\hat{S}(m\mathbf{K})$, arranged such that the constant m would define which side of the spectrum is being referred to. Therefore, in order to use (2.23) to simulate (2.35), the condition expressed by (2.14) must be met, since the Pierson-Moskowitz spectrum is defined as a non-symmetric spectrum. Therefore,

$$\hat{S}(mK) = \frac{1}{2} S_{PM}(K), \tag{2.40}$$

where S_{PM} is the Pierson-Moskowitz spectrum defined by (2.23), and $\hat{S}(mK)$ is the non-directional part of the directional spectrum in (2.35). This conclusion also applies to higher-order cross sections.

2.3.4 Second-Order Bistatic Cross Section

As previously stated, the only second-order scattering mechanism taken into account in this thesis is patch scattering. According to Gill [3], the second-order patch scattering cross section is written as

$$\sigma_{2P}(\omega_d) \approx 2^6 \pi^2 k_o^4 \cos^4 \phi_o \sum_{m_1=\pm 1} \sum_{m_2=\pm 1} \int_{-\pi}^{\pi} \int_0^{\infty} \hat{S}(m_1 \mathbf{K_1}) \hat{S}(m_2 \mathbf{K_2}) \|_s \Gamma_P\|^2 \cdot \delta(\omega_d + m_1 \sqrt{gK_1} + m_2 \sqrt{gK_2}) K_1 dK_1 d\theta_{\mathbf{K_1}}, \tag{2.41}$$

where $\mathbf{K_1}$ and $\mathbf{K_2}$ are chosen such that

$$\mathbf{K_1} + \mathbf{K_2} = \mathbf{K}, \tag{2.42}$$

where $\mathbf{K} = K_B \underline{/\theta_{\mathbf{N}}}$. This is an important difference between the first- and second-order cross sections: while in the first-order cross section the magnitude of $\vec{K}$ is defined by the Doppler frequency, in the second-order, it is the Bragg peak wavenumber as in (2.38). The variables m_1 and m_2 play a similar role to the one played

by m in the first-order cross section. In the second-order, however, m_1 and m_2 are used to distinguish the four spectral areas defined as

$$\begin{aligned}
&1)\ \omega_d < -\omega_B, && m_1 = m_2 = 1 \\
&2)\ -\omega_B < \omega_d < 0, && \begin{cases} m_1 = -1, \quad m_2 = +1, \quad \text{if } K_1 > K_2 \\ m_1 = +1, \quad m_2 = -1, \quad \text{if } K_1 < K_2 \end{cases} \\
&3)\ 0 < \omega_d < \omega_B, && \begin{cases} m_1 = +1, \quad m_2 = -1, \quad \text{if } K_1 > K_2 \\ m_1 = -1, \quad m_2 = +1, \quad \text{if } K_1 < K_2 \end{cases} \\
&4)\ \omega_d > \omega_B, && m_1 = m_2 = -1
\end{aligned} \tag{2.43}$$

Another important feature of the second-order cross section is the symmetricized coupling coefficient ${}_s\Gamma_P$, defined as

$${}_s\Gamma_P = \frac{1}{2}[\Gamma_P(\mathbf{K_1}, \mathbf{K_2}) + \Gamma_P(\mathbf{K_2}, \mathbf{K_1})], \tag{2.44}$$

where Γ_P is the coupling coefficient. In turn, the coupling coefficient is defined as

$$\Gamma_P(\mathbf{K_m}, \mathbf{K_n}) = {}_H\Gamma + {}_E\Gamma_P(\mathbf{K_m}, \mathbf{K_n}), \tag{2.45}$$

where ${}_H\Gamma$ is the hydrodynamic coupling coefficient, defined by (2.29), and ${}_E\Gamma_P$ is the patch scattering electromagnetic coupling coefficient defined as

$${}_E\Gamma_P(\mathbf{K_m}, \mathbf{K_n}) = \frac{k_o}{K\cos(\phi)} \left\{ \frac{j\sqrt{\mathbf{K_m} \cdot (\mathbf{K_m} - 2k_o\hat{\boldsymbol{\rho}}_{\mathbf{0n}})} + k_o}{k_o^2 + \mathbf{K_m} \cdot (\mathbf{K_m} - 2k_o\hat{\boldsymbol{\rho}}_{\mathbf{0n}}) + jk_o\Delta} \cdot \frac{(\mathbf{K_m} \cdot \hat{\boldsymbol{\rho}}_{\mathbf{0n}})[\mathbf{K_n} \cdot (\mathbf{K_m} - k_o\hat{\boldsymbol{\rho}}_{\mathbf{0n}})]}{\sqrt{\mathbf{K_m} \cdot (\mathbf{K_m} - 2k_o\hat{\boldsymbol{\rho}}_{\mathbf{0n}})} + jk_o\Delta} \right\}, \tag{2.46}$$

where Δ is the normalized surface impedance of the ocean surface [57] and $\hat{\boldsymbol{\rho}}_{\mathbf{0n}}$ is the unit vector in the direction of $\boldsymbol{\rho}_{\mathbf{0n}}$. Since only patch scattering is being considered, $\hat{\boldsymbol{\rho}}_{\mathbf{01}} = \hat{\boldsymbol{\rho}}_{\mathbf{02}}$, as observed in Fig. 2.5.

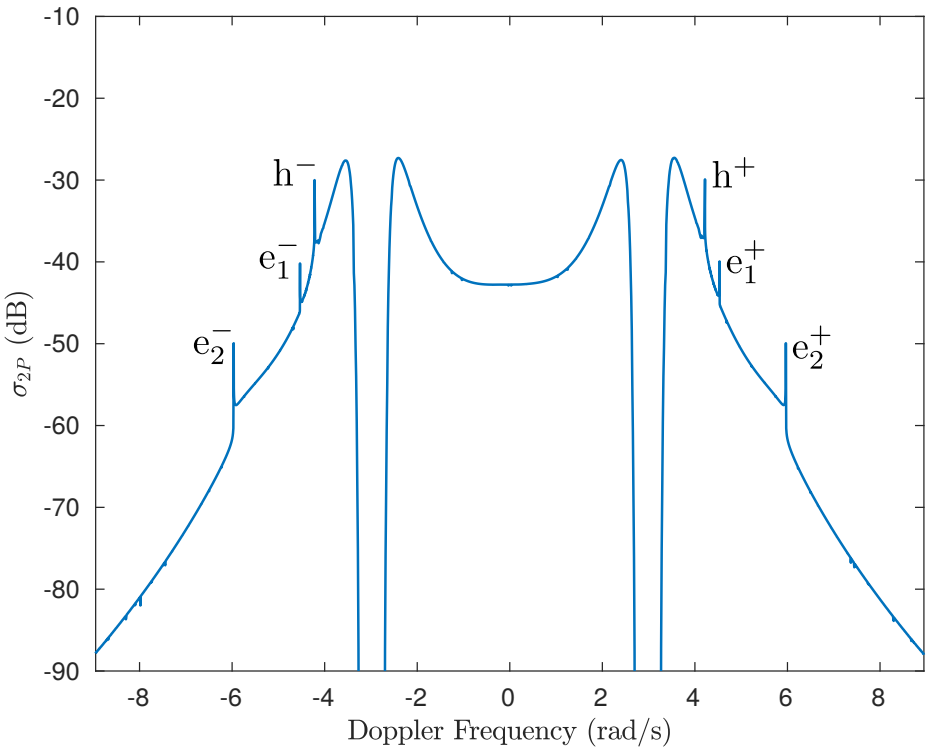

Figure 2.7: Theoretical second-order bistatic cross section. Transmitter frequency $f_o = 25$ MHz, bistatic angle $\phi = 30°$, transmitter look direction $\theta_{01} = 60°$, wind speed $U_{19.5} = 15\ m/s$ and wind direction $\theta_w = \bar{\theta} = 180°$.

Using the same information as for the simulation of the first-order cross-section, the second-order cross section was simulated, as shown in Fig. 2.7. In this simulation, the normalized impedance of the ocean surface was defined as [26]

$$\Delta = \frac{Z}{\eta_o} \approx \frac{1}{120\pi}\sqrt{\frac{\mu}{\epsilon}}, \tag{2.47}$$

where, Z is the impedance of the ocean surface, $\eta_o = 120\pi\ \Omega$ is the impedance of the free space,

$$\epsilon = \epsilon_r \epsilon_o + j\left(\frac{\sigma}{\omega_o}\right)$$

is the electric permittivity of sea water with conductivity $\sigma \approx 4$ $\mho$/m, and relative

permittivity $\epsilon_r = 80$, under a transmitter frequency $\omega_o = 2\pi f_o$.

The peaks observed in Figure 2.7 are due to singularities in the cross-section. According to Gill [3], the h^- and h^+ peaks occur due to a singularity that becomes more evident when a change of variables is applied to Equation (2.41). Making

$$Y \equiv \sqrt{K_1}$$

and

$$K_2 = \sqrt{K_1^2 + K^2 - 2K_1 K \cos(\theta_{\mathbf{K_1}} - \theta_{\mathbf{N}})},$$

and applying the Change of Variables Theorem, the second-order cross-section can be rewritten as

$$\sigma_{2P}(\omega_d) \approx 2^7 \pi^2 k_o^4 \cos^4\phi_o \sum_{m_1=\pm 1} \sum_{m_2=\pm 1} \int_{-\pi}^{\pi} \int_{D_P} \hat{S}(m_1 \mathbf{K_1}) \hat{S}(m_2 \mathbf{K_2}) \|_s \Gamma_P\|^2 \cdot \delta(\omega_d - D_P(Y, \theta_{\mathbf{K_1}})) Y^3 \left| \frac{\partial Y}{\partial D_P} \right|_{\theta_{\mathbf{K_1}}} dD_P \, d\theta_{\mathbf{K_1}}, \quad (2.48)$$

where

$$D_P(Y, \theta_{\mathbf{K_1}}) = -m_1 \sqrt{g} Y - m_2 \sqrt{g} [Y^4 + K^2 - 2Y^2 K \cos(\theta_{\mathbf{K_1}} - \theta_{\mathbf{N}})]^{\frac{1}{4}},$$

and for $L = m_1 m_2$,

$$\left| \frac{\partial Y}{\partial D_P} \right|_{\theta_{\mathbf{K_1}}} = \frac{1}{\sqrt{g} \left| 1 + L \dfrac{Y^3 - Y K \cos(\theta_{\mathbf{K_1}} - \theta_{\mathbf{N}})}{[Y^4 + K^2 - 2Y^2 K \cos(\theta_{\mathbf{K_1}} - \theta_{\mathbf{N}})]^{\frac{3}{4}}} \right|}.$$

When $\theta_{\mathbf{K_1}} = \theta_{\mathbf{N}}$, $Y = \sqrt{\frac{K}{2}} = \sqrt{k_o \cos\phi}$, and $L = 1$, the denominator of the Jacobian $\left| \frac{\partial Y}{\partial D_P} \right|_{\theta_{\mathbf{K_1}}}$ vanishes, causing a singularity at

$$\omega_d = \mp \sqrt{2} \omega_B,$$

marked as h^- and h^+ in Figure 2.7. As for the e_1 and e_2 peaks, they occur due to singularities in the electromagnetic coupling coefficient ${}_E\Gamma_P$. From Equation (2.46), a singularity will occur when

$$\mathbf{K_m} \cdot (\mathbf{K_m} - 2k_o\hat{\boldsymbol{\rho}}_{\mathbf{0n}}) - k_o^2\Delta^2 = 0,$$

where $\theta_{0n} = \theta_{\mathbf{N}} - \phi$. If a (K_{m_x}, K_{m_y}) plane is considered, this equation can be rewritten as

$$K_{m_x}^2 + K_{m_y}^2 - (2k_o\cos\theta_{0n})K_{m_x} - (2k_o\sin\theta_{0n})K_{m_y} - k_o^2\Delta^2 = 0. \tag{2.49}$$

Geometrically, Equation (2.49) represents the expression for a conic section centred at $(k_o\cos(\theta_{\mathbf{N}} - \phi), k_o\sin(\theta_{\mathbf{N}} - \phi))$ and radius $k_o\sqrt{1+\Delta}$. Gill [3] demonstrated that if a perfect conductive surface is considered, i.e. $\Delta \to 0$, the singularities will occur for $K_1 = K_2$ and

$$\omega_d = \pm 2^{\frac{3}{4}}\sqrt{\frac{(1 \pm \sin\phi)^{\frac{1}{2}}}{\cos\phi}}\ \omega_B. \tag{2.50}$$

However, if a complex Δ such that $\mathrm{Im}\{\Delta^2\} \neq 0$ is considered, the left-hand side of Equation (2.49) will never go to zero, since

$$\mathrm{Im}\left\{K_{m_x}^2 + K_{m_y}^2 - (2k_o\cos\theta_{0n})K_{m_x} - (2k_o\sin\theta_{0n})K_{m_y}\right\} = 0,\ \forall\ \mathbf{K_m} = (K_{m_x}, K_{m_y}),$$

and

$$\mathrm{Im}\{\Delta^2\} \neq 0 \iff \mathrm{Im}\{(a+jb)^2\} \neq 0 \iff 2jab \neq 0 \iff a \neq 0,\ b \neq 0,\ \forall\ a, b \in \mathbb{R}.$$

Therefore, if Δ has both nonzero real and imaginary parts, Equation (2.49) will never go to zero and, instead of singularities, the electromagnetic peaks $e_1^{+,-}$ and $e_2^{+,-}$ will occur at the same frequencies found in Equation (2.50), since $k_o\Delta^2$ is not dependent on $\mathbf{K_m}$.

2.4 General Chapter Summary

In this chapter, the theoretical background for the thesis was presented. Section 2.2 presented the fundamental concepts regarding ocean waves, their classification, generation and development. Later, the ocean wave spectrum was discussed, showing the mathematical development of the ocean wave spectrum, as well as its fundamental characteristics. One model for the non-directional ocean wave spectrum and one for the directional spreading function were presented. At the end of the section, the problem of wave-wave interaction was addressed, showing how multiple wave interactions affect the distribution of Fourier parameters on the ocean surface.

In Section 2.3, the bistatic radar cross section was introduced. The definition of "cross section" was presented, emphasizing the importance of this measurement in radio oceanography. The scattering mechanisms were also presented, showing how cross sections are classified, and how the received electric field can be analysed. Then, the bistatic geometry for patch scattering was introduced, presenting the basic angle relationships in a bistatic radar. Once the scattering mechanisms and bistatic geometry were explained, the first- and second-order cross sections were addressed, detailing how both geometry and the scattering mechanisms influence the measurement.

From the ideas laid down in this chapter, the problem of wave inversion can be discussed. In the next chapter, the changes of coordinates for the second-order cross section will be presented, as well as the method for the extraction of the ocean wave spectrum using the presented change of variables.

Chapter 3

Extraction of Ocean Wave Spectrum from Second-Order Bistatic Cross Section

3.1 Introduction

In Chapter 2, the fundamentals of ocean wave classification, generation, and development were discussed, as well as how the status and behaviour of the ocean can be quantified using the directional ocean wave spectrum. Being one of the most important measurements in forecasting the ocean surface, various technologies have been developed to obtain the directional ocean wave spectrum. Among the instruments applied to this analysis, HF radar is one of the most versatile, due to its ability to measure different parts of the ocean just by steering the receiver beam, if an antenna such as a phased array is used.

In radio oceanography, the radar cross section plays a crucial role in the process of extracting the ocean wave spectrum. If the mathematical formulation of the cross section, especially, as suggested by Hasselmann [29], of the second-order cross section, is known, several mathematical inversion methods can be applied to obtain the ocean wave spectrum. Section 1.2 presented an overview of how these methods evolved.

In this chapter, a new method, similar to the one presented by Shahidi and Gill [1] for the monostatic case, is applied to obtain the ocean wave spectrum from the second order bistatic radar cross section. To understand the kind of problem being dealt with and the need for a simplification of the second-order cross section, the fundamental mathematical concepts regarding nonlinear inverse problems and their solution will be presented. First, a brief explanation on Hilbert spaces is necessary, since it is a concept extensively used in the definition of inverse problems and their solutions. This will be followed by a definition of well- and ill-posed problems, and how inverse problems, such as the nonlinear Fredholm equation of the first kind, relate to these definitions. Then, Tiknonov regularization in Hilbert scales will be presented, as well as how it can be used to solve nonlinear ill-posed problems. Finally, the second-order cross section will be simplified to facilitate the use of Tikhonov regularization to extract the directional ocean wave spectrum, with results of the extraction subsequently presented.

3.2 Fundamental Concepts for the Nonlinear Extraction of the Ocean Wave Spectrum

The extraction of the ocean wave spectrum from the second-order cross section is an example of what is known in mathematics and other fields as an *inverse problem*. Inverse problems are a class of problems in which the goal is to obtain the cause of a phenomenon from observed measurements. In the case of the problem laid out in this thesis, it is desired to obtain the ocean wave spectrum from HF radar data, more specifically the radar cross section per unit area. Due to the nonlinear nature the problem, special care must be taken in choosing the method of solution.

A fundamental concept that frequently arises while studying the solution of inverse problems is the one of Hilbert spaces.

3.2.1 Vector, Banach, Hilbert, and Euclidean Spaces

The vector space is one of the most basic concepts of linear algebra. A vector space is a set V which is defined by two laws of composition [93]:

- Addition: $\forall \mathbf{u}, \mathbf{v} \in V,\ \exists \mathbf{w} \in V,\ \mathbf{u} + \mathbf{v} = \mathbf{w}$.
- Scalar multiplication: $\forall \mathbf{u} \in V,\ c \in \mathbb{R},\ \exists \mathbf{v} \in V,\ \mathbf{v} = c\mathbf{u}$.

Consequently, a vector space must satisfy the following axioms:

- By having addition as one of its laws of composition, the vector space V becomes an abelian group V^+, which implies that it meets the following requirements:
  - Closure: $\forall \mathbf{u}, \mathbf{v} \in V,\ \exists \mathbf{w} \in V,\ \mathbf{u} + \mathbf{v} = \mathbf{w}$

  - Commutativity: $\forall \mathbf{u}, \mathbf{v} \in V,\ \mathbf{u} + \mathbf{v} = \mathbf{v} + \mathbf{u}$
  - Associativity: $\forall \mathbf{u}, \mathbf{v}, \mathbf{w} \in V,\ (\mathbf{u} + \mathbf{v}) + \mathbf{w} = \mathbf{u} + (\mathbf{v} + \mathbf{w})$
  - Identity element: $\exists \mathbf{0}_V \in V,\ \forall \mathbf{v} \in V, \mathbf{v} + \mathbf{0}_V = \mathbf{0}_V + \mathbf{v} = \mathbf{v}$.
  - Inverse element: $\forall \mathbf{v} \in V,\ \exists \mathbf{u} \in V,\ \mathbf{u} + \mathbf{v} = \mathbf{v} + \mathbf{u} = \mathbf{I}$. In the case of addition, $\mathbf{u} = -\mathbf{v}$.

- Scalar multiplication also satisfies the associativity requirement, meaning that $\forall \mathbf{v} \in V,\ a, b \in \mathbb{R},\ (ab)\mathbf{v} = a(b\mathbf{v})$
- The identity element for scalar multiplication is the real number 1, therefore $1\mathbf{v} = \mathbf{v}$.
- Scalar multiplication satisfies the following distributive laws $\forall a, b \in \mathbb{R},\ \forall \mathbf{u}, \mathbf{v} \in V$

$$(a + b)\mathbf{v} = a\mathbf{v} + b\mathbf{v}$$

$$a(\mathbf{u} + \mathbf{v}) = a\mathbf{u} + a\mathbf{v}$$

Even though vector spaces are a powerful concept used in different applications [94], they are still rather limited, since only addition and scalar multiplication are defined in a vector space. Therefore, spaces that include more operations are often needed.

One of the most commonly used operators in vector spaces is the norm. By definition, norm is a functional $\|\cdot\| : V \to \mathbb{R}$ that satisfies the following requirements $\forall a \in \mathbb{R}, \mathbf{u}, \mathbf{v} \in V$ [95]:

- Positive homogeneity: $\|a\mathbf{v}\| = |a|\|\mathbf{v}\|$

- Triangle inequality: $\|\mathbf{u}+\mathbf{v}\| \leq \|\mathbf{u}\| + \|\mathbf{v}\|$
- Non-negativity: $\|\mathbf{u}\| \geq 0$. $\|\mathbf{u}\| = 0 \iff \mathbf{u} = \mathbf{0}_V$

If a vector space V is equipped with a norm, it is known as a *normed space*, and the norm will be noted as $\|\cdot\|_V$. If the distance between elements inside a normed space V is defined $\forall \mathbf{u}, \mathbf{v} \in V$ as

$$d(\mathbf{u}, \mathbf{v}) = \|\mathbf{v} - \mathbf{u}\|_V,$$

then V is known as a *metric space* with metric d.

Among the most largely used norms in science is the L^p-norm, defined as

$$\|\mathbf{v}\|_p = \left(\sum_{i=1}^{n} |v_i|^p \right)^{1/p} \tag{3.1}$$

for $p \in \mathbb{R},\ p \geq 1$, and $\mathbf{v} = (v_1, \cdots, v_n)$. If a normed space is equipped with the L^p-norm, this space is known as a L^p-space.

According to, for example, Royden and Fitzpatrick [95], a sequence $\{\mathbf{v}_n\}$ in a normed space V is said to be Cauchy in V if, for each $\epsilon > 0$, there is $N \in \mathbb{N}$ such that

$$\|\mathbf{v}_n - \mathbf{v}_m\| < \epsilon,\ \forall\ m, n \geq N.$$

If every Cauchy sequence $\{\mathbf{v}_n\} \in V$ converges to a vector $\mathbf{v} \in V$, i.e.

$$\lim_{n\to\infty} \|\mathbf{v}_n - \mathbf{v}\|_V = 0,$$

then V is said to be *complete*. A complete metric space is then known as a *Banach space*.

Another important operator with which vector spaces can be equipped is the inner product. The inner product is defined by the functional $\langle \cdot, \cdot \rangle : V \times V \to \mathbb{C}$ (or $\mathbb{R}$), which satisfies the following statements $\forall \mathbf{u}, \mathbf{v}, \mathbf{w} \in V,\ \forall a, b \in \mathbb{R}$ [95, 96]

- $\langle \mathbf{u}, \mathbf{v} \rangle = \overline{\langle \mathbf{v}, \mathbf{u} \rangle}$, where $\overline{\langle \mathbf{u}, \mathbf{v} \rangle}$ is the complex conjugate of $\langle \mathbf{u}, \mathbf{v} \rangle$.
- $\langle a\mathbf{u} + b\mathbf{v}, \mathbf{w} \rangle = a\langle \mathbf{u}, \mathbf{w} \rangle + b\langle \mathbf{v}, \mathbf{w} \rangle$
- $\langle \mathbf{v}, \mathbf{v} \rangle \geq 0,\ \langle \mathbf{v}, \mathbf{v} \rangle = 0 \iff \mathbf{v} = \mathbf{0}_V$

If a vector space is equipped with inner product, this space is known as an *inner product space*. If a Banach space H is also an inner product space and has its norm defined such that, $\forall \mathbf{v} \in V$,

$$\|\mathbf{v}\|_H^2 = \langle \mathbf{v}, \mathbf{v} \rangle,$$

then H is called a *Hilbert space*.

Now, consider a Hilbert space that is isomorphic to a real space — $H \cong \mathbb{R}^n$, with $n \in \mathbb{N}$ being the dimension of $\mathbb{R}^n$ — with L^2-norm as its metric, i.e. H is a real L^2-space. This space is known as an *Euclidean space*.

In summary, Banach and Hilbert spaces are complete vector spaces that are equipped with extra functions — Banach spaces being equipped with a norm, and Hilbert spaces with both a norm and an inner product. Euclidean space is a particular case of a real n-dimensional Hilbert space that has an L^2-norm.

With the basic definitions of vector, Banach, Hilbert and Euclidean spaces in place, it is important to understand the types of problems that can be presented and which methods are available to solve them.

3.2.2 Posedness of a problem

Mathematically, a nonlinear problem can be written as [97–99]

$$F(\mathbf{x}) = \mathbf{y}_0, \tag{3.2}$$

where $F : D(F) \subset X \rightarrow Y$ is a the nonlinear operator between the Hilbert spaces X and Y, $\mathbf{x} \in X$ are the parameters of the operator F, and $\mathbf{y}_0 \in Y$ is the output of the operator F. If $\mathbf{x}$ is given and it is desired to obtain $\mathbf{y}_0$, the problem is known as a *forward problem*, while if $\mathbf{y}_0$ is given and $\mathbf{x}$ is desired, the problem is classified as an *inverse problem*.

A number of problems in science are described as inverse problems, e.g. reconstruction of a structure by using X-ray tomography, deblurring of images [100], or the extraction of the ocean wave spectrum herein presented. An often used example of nonlinear inverse problem is the nonlinear Fredholm equation of the first kind [98]. This type of integral equation is often found while solving inverse problems [101] and can be written as [102]

$$y(z) = \int_a^b K(z,t)N(x(z))dt, \tag{3.3}$$

where $K(z,t)$ is known as the kernel of the equation, and N is a nonlinear function of the input x.

A problem is considered to be well-posed in the Hadamard sense, if and only if, it simultaneously satisfies the following properties: it has a solution, this solution is unique, and this solution is uniformly continuous — in other words, given a generic function $g : X \rightarrow Y$, $\forall x_1, x_2 \in X$, $\forall\ \varepsilon > 0,\ \exists\ \delta > 0,\ \varepsilon, \delta \in \mathbb{R}$, such that

$$\|x_1 - x_2\| < \delta \Rightarrow \|g(x_1) - g(x_2)\| < \varepsilon.$$

If a problem does not respect one of the previous statements, it is referred to as being *ill-posed*. Inverse problems are almost always ill-posed [103, 104].

Another important definition that must be understood while dealing with integral equations is the one of well- and ill-conditioned problems. As described, for example,

by Vandenberghe [105], a problem is well conditioned if small changes in the problem input lead to small changes in its output; conversely, if small changes in the problem parameters lead to a large change in its output, it is considered ill-conditioned. This definition must not be confused with the definition of ill-posedness, even though these characteristics might appear together in a problem. A problem can be well-posed and ill-conditioned if it has a unique solution and the mapping between input and output is uniformly continuous, even if $\delta << \varepsilon$.

In the case of Fredholm equations of the first kind, the problem is considered ill-posed for both linear [98, 106] and nonlinear [102] equations. It must be noted, however, that the nonlinear Fredholm equation of the second kind, described as

$$y(z) = x(z) + \int_a^b K(z,t)N(x(z))dt,$$

are well-posed [102]. Therefore, one available method to solve Fredholm equations of the first kind is to approximate it to the closest Fredholm equation of the second kind. This process, suggested independently by Phillips [107] and Tikhonov [97], is commonly known as Tikhonov regularization. Once the problem is regularized, a number of methods can be used to solve for the now well-posed problem. Such techniques include the direct computation method, and the Adomian decomposition method [102]. Another method, that combines both regularization and an algorithm to solve the inverse problem is known as regularized nonlinear least squares [104].

3.2.3 Regularized Nonlinear Least-Squares

Nonlinear least-squares is a data fitting technique in which the goal is to find the set of parameters that minimizes the quadratic deviation between the ideal output

of a system and the measured output, normally contaminated with noise or other perturbations. Consider $\mathbf{y}_\delta \in Y$ the measured and $\mathbf{y}_0$ the ideal output, where δ is the perturbation level defined as

$$\|\mathbf{y}_\delta - \mathbf{y}_0\|_Y \leq \delta. \tag{3.4}$$

The nonlinear least-squares solution $\hat{\mathbf{x}} \in D(F)$ for (3.2) can be written as

$$\hat{\mathbf{x}} = \min_{\mathbf{x}} \|F(\mathbf{x}) - \mathbf{y}_\delta\|_Y^2. \tag{3.5}$$

Among the optimization algorithms that can be used to solve (3.5), one of the most commonly used is the Levenberg-Marquardt algorithm [108, 109].

As previously discussed, solving for $\mathbf{x}$ in a nonlinear Fredholm equation of first kind as in Equation (3.3) is an ill-posed problem in the Hadamard sense. The direct use of optimization methods, such as nonlinear least-squares, is insufficient to solve this type of problem. Tikhonov [97] proposed the inclusion of a regularizing parameter to the least-squares problem, resulting in the technique known as *Tikhonov regularization*, or *regularized least-squares* . In the case of a nonlinear equation, this method is also known as *regularized nonlinear least-squares*.

The solution using the Tikhonov regularization can be written as [110]

$$\hat{\mathbf{x}} = \min_{\mathbf{x}} \|F(\mathbf{x}) - \mathbf{y}_\delta\|_Y^2 + \alpha\|\mathbf{x} - \mathbf{x}^*\|_X^2, \tag{3.6}$$

where α is known as the regularization parameter, and $\mathbf{x}^*$ is a parameter that helps to define the selection criterion in the case of multiple least-square solutions [110].

Due to its popularity, several improvements have been incorporated into the original Tikhonov regularization. One of these improvements is called Tikhonov regular-

ization in Hilbert scales [99]. In this method, the norm of the regularizing term is substituted by a stronger norm.

3.2.4 Tikhonov Regularization in Hilbert Scales

Let X_0 be the space such that $\|\mathbf{x}\|_{X_0} \sim \|\mathbf{x}\|_X \forall \mathbf{x} \in X$, and $(X_s)_{s\in\mathbb{R}}$ be the Hilbert scale of X_0, defined as a set induced by the application of a densely defined, self-adjoint and strictly positive operator $\mathscr{Y}$, in which all the powers of $\mathscr{Y}$ are defined [111]. In this space, the norm $\|\cdot\|_r$ is defined such that

$$\|\mathbf{x}\|_r = \|\mathscr{Y}^r\mathbf{x}\|_{X_0} \sim \|\mathscr{Y}^r\mathbf{x}\|_X,\ r \in \mathbb{R}. \tag{3.7}$$

By using the Hilbert scale in the regularization parameter, (3.6) can be rewritten as [99]

$$\begin{aligned}\hat{\mathbf{x}} &= \min_{\mathbf{x}} \|F(\mathbf{x}) - \mathbf{y}_\delta\|_Y^2 + \alpha\|\mathbf{x} - \mathbf{x}^*\|_r^2 \\ &= \min_{\mathbf{x}} \|F(\mathbf{x}) - \mathbf{y}_\delta\|_Y^2 + \alpha\|\mathscr{Y}^r(\mathbf{x} - \mathbf{x}^*)\|_X^2.\end{aligned} \tag{3.8}$$

It may be observed that, for $r = 0$, the form in (3.8) returns to its original form, expressed by (3.6). In several applications, a differential operator D is used as the constraint operator $\mathscr{Y}$ for the Hilbert scale for L^2-spaces [112, 113].

The most often used differential operators in regularizing parameters are the first- and second-order differential operators, respectively D^1 and D^2. Using finite differences, these operators can be written as [113]

$$D^2 = \begin{bmatrix} -2 & 1 & & \\ 1 & \ddots & \ddots & \\ & \ddots & \ddots & 1 \\ & & 1 & -2 \end{bmatrix},\ D^1 = (D^2)^{1/2}. \tag{3.9}$$

The use of a differential operator in the regularization term is also mentioned for the linear case [114].

3.2.5 Determination of the Regularization Parameter

Once the form of the Tikhonov regularization is known, it is necessary to devise a formulation for the regularization parameter α. One of the most widely-used methods to determine the regularization parameter is the L-curve method [115]. This method uses a log-log plot of the quadratic deviation $\Phi(x, y_\delta)$ *versus* the regularizing term $\Omega(x)$ for different values of α, which usually has an L-shape. The value of α on the corner of the L-curve is considered the optimal value of the regularization parameter, since an equilibrium of both $\Phi(x, y_\delta)$ and $\Omega(x)$ is achieved [116].

Over the years, several approaches have been developed. They can be divided into two main groups: the methods that rely on *a priori* knowledge, and the ones that rely on *a posteriori* knowledge [117]. Since *a priori* knowledge of the problem is not always available, a great number of very sophisticated *a posteriori* methods have been developed, among them, some iterative methods [118].

Neubauer [119] determined that the best possible convergence rate for nonlinear Tikhonov regularization is $O(\delta^{2/3})$, where δ is defined in (3.4). In his paper, he delineated under which conditions this convergence rate can be achieved, and one of the necessary conditions is that the regularization parameter is given by

$$\alpha \sim \delta^{2/3}. \tag{3.10}$$

This is, however, an *a priori* approach to the regularization problem, since the discrepancy rate δ must be known beforehand. Some modifications can be introduced in

order to find an optimal parameter choice based on the one proposed by Neubauer. Substituting the discrepancy parameter by the quadratic deviation in the previous iteration, the iterative *a posteriori* regularization parameter based on (3.10) can be written as

$$\alpha_k = \|F(x_{\alpha_{k-1}}) - y_\delta\|_Y^{2/3}. \tag{3.11}$$

3.3 Simplification of the Second-Order Bistatic Cross Section

With the tools presented in the previous section, it is possible to obtain a solution for an inverse problem such as a nonlinear Fredholm equation of the first kind. In this section, the problem of extracting the directional ocean wave spectrum from the bistatic second-order cross section will be considered.

Here, the formulation of the second order bistatic radar cross section will be repeated, to facilitate understanding of the subsequent steps:

$$\sigma_{2P}(\omega_d) \approx 2^6\pi^2 k_o^4 \cos^4\phi_o \sum_{m_1=\pm1}\sum_{m_2=\pm1}\int_{-\pi}^{\pi}\int_0^{\infty} \hat{S}(m_1\mathbf{K_1})\hat{S}(m_2\mathbf{K_2})\|_s\Gamma_P\|^2 \\ \delta(\omega_d + m_1\sqrt{gK_1} + m_2\sqrt{gK_2})K_1\ dK_1 d\theta_{\mathbf{K_1}} \tag{3.12}$$

Even though Equation (3.12) resembles a nonlinear Fredholm equation of the first kind, it is a considerably more complicated problem. As can be observed, the expression for the second-order bistatic cross section can be classified as a double nonlinear integral Fredholm equation of the first kind, in which $\hat{S}$ is the parameter to be inverted, and it is presented as a product of two different inputs, $m_1\mathbf{K_1}$ and $m_2\mathbf{K_2}$. Its

kernel includes constraints in K_1 and K_2 embedded in the Dirac delta function, which worsens the problem of uniform continuity. In summary, dealing with (3.12), or its variation presented by Barrick [120], is not a trivial task, especially for the bistatic radar configuration. These complications led Zhang and Gill [68] to use the linearization proposed by Howell [47] to extract the ocean wave spectrum from (3.12) in the bistatic case. It has also led many other authors to use linearizations and constraints to solve for the monostatic case. Here, a simplification is sought in order to transform Equation (3.12) into a nonlinear Fredholm equation of the first kind, a problem with available and well-known solution techniques, as presented in the previous section.

As proposed by Shahidi and Gill [1], the use of the Dirac delta function in (3.12) suggests that the second-order radar cross section can be treated as a convolution integral. To make the integration possible, a change of variables must be applied to (3.12), allowing the integration of the Dirac delta function and reducing the expression of the second-order radar cross section to a single nonlinear Fredholm integral equation of the first kind, which is significantly simpler to solve by means of nonlinear optimization.

Observing the argument of the Dirac delta in (3.12), the following coordinates must be used in the simplification:

$$\begin{cases} Y_1 &= \sqrt{K_1} \\ Y_2 &= \sqrt{K_2}. \end{cases} \tag{3.13}$$

To use the change of coordinates theorem, the Jacobian of the coordinate transform

must be calculated. The Jacobain for the change of coordinates is given by

$$J = \begin{vmatrix} \dfrac{\partial K_1}{\partial Y_1} & \dfrac{\partial K_1}{\partial Y_2} \\ \dfrac{\partial \theta_{\mathbf{K_1}}}{\partial Y_1} & \dfrac{\partial \theta_{\mathbf{K_1}}}{\partial Y_2} \end{vmatrix} = \frac{\partial K_1}{\partial Y_1}\frac{\partial \theta_{\mathbf{K_1}}}{\partial Y_2} - \frac{\partial K_1}{\partial Y_2}\frac{\partial \theta_{\mathbf{K_1}}}{\partial Y_1} \tag{3.14}$$

The first row derivatives can be readily calculated, with the results being

$$\frac{\partial K_1}{\partial Y_1} = 2Y_1 \tag{3.15}$$

and

$$\frac{\partial K_1}{\partial Y_2} = 0. \tag{3.16}$$

The fact that the partial derivative in (3.16) is equal to zero, eliminates the need of calculating the other element of the antidiagonal.

From the relationship described in (2.42), the law of cosines may be used to derive an expression that relates the magnitudes of $\mathbf{K_1}$ and $\mathbf{K_2}$ and the angle $\theta_{\mathbf{K_1}}$:

$${K_2}^2 = {K_1}^2 + K^2 - 2K_1 K\cos(\theta_N - \theta_{\mathbf{K_1}}). \tag{3.17}$$

By using the change of variables presented in (3.13), Equation (3.17) can be rewritten as

$${Y_2}^4 = {Y_1}^4 + K^2 - 2{Y_1}^2 K\cos(\theta_N - \theta_{\mathbf{K_1}}). \tag{3.18}$$

From (3.18), the remaining partial derivative can be written as

$$\frac{\partial \theta_{\mathbf{K_1}}}{\partial Y_2} = \frac{-2Y_2^3}{Y_1^2 K\sin(\theta_N - \theta_{\mathbf{K_1}})}. \tag{3.19}$$

Therefore, (3.14) can be written as

$$J = \frac{-4{Y_2}^3}{Y_1 K\sin(\theta_N - \theta_{\mathbf{K_1}})}. \tag{3.20}$$

Using the change of coordinates theorem, (3.12) can be rewritten as

$$\sigma_{2P}(\omega_d) \approx 2^6\pi^2 k_o^4 \cos^4\phi_o \sum_{m_1=\pm1}\sum_{m_2=\pm1}\int_0^\infty\int_0^\infty S_1(m_1\mathbf{K_1})S_1(m_2\mathbf{K_2})\|_s\Gamma_P\|^2 \\ \delta(\omega_d + m_1\sqrt{g}Y_1 + m_2\sqrt{g}Y_2)Y_1^2\|J\|dY_1dY_2, \quad (3.21)$$

where $\mathbf{K_1} = Y_1^2\underline{/\theta_{K_1}}$ and $\mathbf{K_2} = Y_2^2\underline{/\theta_{K_2}}$. Making

$$H(Y_1, Y_2) = 2^5\pi k_o^4 \cos^4\phi_o\|_s\Gamma_P\|^2 Y_1^2\|J\| \quad (3.22)$$

and

$$\hat{S}(m_i\mathbf{K_i}) = \hat{T}(m_i, Y_i, \theta_{\mathbf{K_i}}),\ \mathrm{i} = 1,\ 2, \quad (3.23)$$

Equation (3.21) can be rewritten as

$$\sigma_{2P}(\omega_d) \approx 2\pi \sum_{m_1=\pm1}\sum_{m_2=\pm1}\int_0^\infty\int_0^\infty H(Y_1, Y_2)\hat{T}(m_1, Y_1, \theta_{\mathbf{K_1}})\hat{T}(m_2, Y_2, \theta_{\mathbf{K_2}}) \\ \cdot\,\delta(\omega_d + m_1\sqrt{g}Y_1 + m_2\sqrt{g}Y_2)dY_1dY_2. \quad (3.24)$$

By integrating (3.24) over Y_2, the second-order cross section can be reduced to a single integral, as follows:

$$\sigma_{2P}(\omega_d) \approx 2\pi \sum_{m_1=\pm1}\sum_{m_2=\pm1}\int_0^\infty H(Y_1, Y_2)\cdot\hat{T}\left(m_1, Y_1, \theta_{\mathbf{K_1}}\right)\hat{T}\left(m_2, Y_2, \theta_{\mathbf{K_2}}\right)dY_1, \quad (3.25)$$

where Y_2 is given by

$$Y_2 = -\left(\frac{\omega_d}{m_2\sqrt{g}} + \frac{m_1}{m_2}Y_1\right). \quad (3.26)$$

In order to emphasize the directional and non-directional parts of the spectrum, the definition in (2.10) can be applied to $\hat{T}$ in Equation (3.25), resulting in

$$\sigma_{2P}(\omega_d) \approx 2\pi \sum_{m_1=\pm1}\sum_{m_2=\pm1}\int_0^\infty H(Y_1, Y_2)\cdot\left[\tilde{T}(Y_1)D\left(m_1, \theta_{\mathbf{K_1}}\right)\right] \\ \cdot\left[\tilde{T}(Y_2)D\left(m_2, \theta_{\mathbf{K_2}}\right)\right]dY_1. \quad (3.27)$$

From Equation (3.26), it is evident that at each Doppler shift ω_d, Y_2 is a translation of $\pm Y_1$ by a factor of $\pm\frac{\omega_d}{\sqrt{g}}$, with the signs varying independently, since $m_1, m_2 = \pm 1$. This is an important conclusion from the coordinate change presented herein. Since Y_1 and Y_2 represent waves in the same scattering patch and this patch is considered small for a narrow beam radar, the waves in the second-order spectrum share the same non-directional spectral distribution. Therefore, $\tilde{T}(Y_2)$ is a translated form of $\tilde{T}(Y_1)$ for patch scattering with a narrow beam radar. This result allows for simplifications in the wave extraction process that will be addressed later.

This expression is a reduced form of the second-order bistatic radar cross section, expressed in (3.12). Still, the angles $\theta_{\mathbf{K_1}}$ and $\theta_{\mathbf{K_2}}$ are present in (3.27). Thus, a relationship between Y_1, Y_2 and its angles must be found.

3.3.1 Wave Vector Direction in the New Coordinate Frame

Figure 3.1 presents the details of the second-order patch scattering geometry. As may be observed, the resulting wave vector $\mathbf{K}$ has the same direction as the normal to the ellipse $\mathbf{N}$, as explained in Section 2.3.4, and has magnitude equal to K_B, given by (2.38). The combination of any $\mathbf{K_1}$ and $\mathbf{K_2}$ must result in K, as expressed in (2.42).

Unlike the monostatic case presented by Shahidi and Gill [1], the direction of $\mathbf{K}$ does not coincide with the transmitter look direction. Instead, it coincides with the normal to the ellipse. This introduces a rotation to the wave vector system with respect to the transmitter coordinates. To take this into account, the angle $\theta_{\mathbf{N}}$ must be taken into consideration in the scattering analysis.

Being the result of a vector sum, the magnitudes of $\mathbf{K}$, $\mathbf{K_1}$, and $\mathbf{K_2}$ follow the

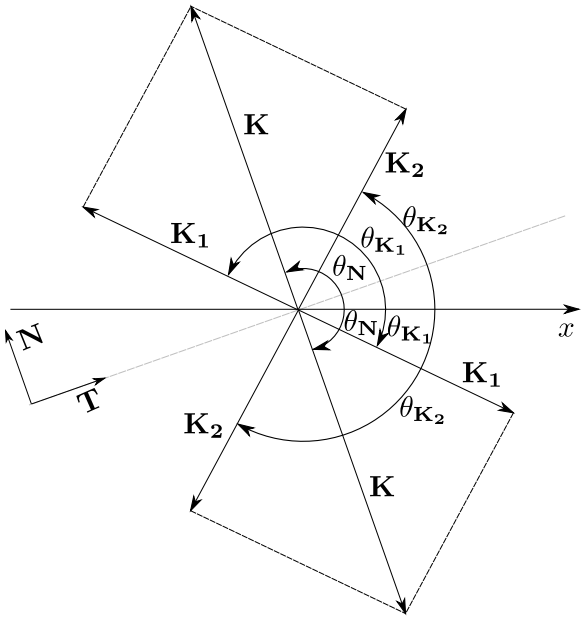

Figure 3.1: Geometry of the wave numbers in the second-order patch scattering

cosine law. This characteristic was previously taken into account while calculating the Jacobian for the change of variables. From (3.18), it is possible to obtain a relationship between $\theta_{\mathbf{K_1}}$, Y_1, and Y_2. This relationship can be written as

$$\theta_{\mathbf{K_1}} = \theta_{\mathbf{N}} \mp \arccos\left(\frac{{Y_1}^4 - {Y_2}^4 + K^2}{2K{Y_1}^2}\right). \tag{3.28}$$

Similarly, an expression that relates $\theta_{\mathbf{K_2}}$, Y_1, and Y_2 can be found by using the law of cosines. Since $\mathbf{K_2} = \mathbf{K} - \mathbf{K_1}$ from (2.42),

$$\theta_{\mathbf{K_2}} = \theta_{\mathbf{N}} \pm \arccos\left(\frac{{Y_2}^4 - {Y_1}^4 + K}{2K{Y_2}^2}\right). \tag{3.29}$$

The $\mp$ and $\pm$ signs for the inverse cosine functions in (3.28) and (3.29) are consequences of the trigonometric identity $\cos(\psi) = \cos(-\psi),\ \forall\psi$. The angles are chosen in pairs such that if the top sign is chosen for one of the angles, the top sign should also be chosen for the other angle. Therefore, the possible pairs of angles, making

$K = 2k_o \cos\phi$, are

$$\begin{cases} \theta^{-}_{\mathbf{K_1}} & = \theta_{\mathbf{N}} - \arccos\left(\dfrac{{Y_1}^4 - {Y_2}^4 + 4{k_o}^2\cos^2\phi}{4k_o{Y_1}^2\cos\phi}\right) \\ \theta^{+}_{\mathbf{K_2}} & = \theta_{\mathbf{N}} + \arccos\left(\dfrac{{Y_2}^4 - {Y_1}^4 + 4{k_o}^2\cos^2\phi}{4k_o{Y_2}^2\cos\phi}\right) \end{cases}$$

and

$$\begin{cases} \theta^{+}_{\mathbf{K_1}} & = \theta_{\mathbf{N}} + \arccos\left(\dfrac{{Y_1}^4 - {Y_2}^4 + 4{k_o}^2\cos^2\phi}{4k_o{Y_1}^2\cos\phi}\right) \\ \theta^{-}_{\mathbf{K_2}} & = \theta_{\mathbf{N}} - \arccos\left(\dfrac{{Y_2}^4 - {Y_1}^4 + 4{k_o}^2\cos^2\phi}{4k_o{Y_2}^2\cos\phi}\right). \end{cases}$$

If the same signs are chosen, the condition in the vector sum expressed in (2.42) cannot be fulfilled and, therefore, this is not a possible combination.

By adapting the expressions of $\theta_{\mathbf{K_1}}$ and $\theta_{\mathbf{K_2}}$ presented by Shahidi and Gill [1] for the monostatic case to the non-normalized case, the directions of $\mathbf{K_1}$ and $\mathbf{K_2}$ can be respectively written as

$$\theta_{\mathbf{K_1}_{\text{Monost.}}} = \pm\arccos\left(\frac{{Y_2}^4 - {Y_1}^4 - K^2}{2K{Y_1}^2}\right) \tag{3.30}$$

$$\theta_{\mathbf{K_2}_{\text{Monost.}}} = \mp\arccos\left(\frac{{Y_1}^4 - {Y_2}^4 - K^2}{2K{Y_2}^2}\right). \tag{3.31}$$

Due to the scattering geometry in the monostatic case, both possible values in Equation (3.30) have the same magnitudes. The same observation applies to Equation (3.31). This reduces the problem of multiple scattering angles for the same magnitudes of $\mathbf{K_1}$ and $\mathbf{K_2}$ to a simple multiplication by a factor of two Shahidi [121]. In the bistatic configuration, however, this symmetry is not present due to the direction of $\mathbf{K}$ not being the same as that of the transmitted signal. In this case, the two angles in Equations (3.28) and (3.29) will have different magnitudes. Therefore, the cross section needs to be calculated for each possible angle in a $(\mathbf{K_1}, \mathbf{K_2})$ pair.

From Equations (3.26), (3.28) and (3.29), it is possible to conclude that the second-order cross section in the new coordinate frame, presented in (3.27), is only dependent on Y_1, since all other variables can be obtained from expressions that relate it with other quantities, such as Doppler shift ω_d, transmitter wave number k_o, and bistatic angle ϕ. This opens up the possibility of using nonlinear optimization techniques in a more efficient manner, since the expression in (3.27) is a simplified version of (3.12).

3.4 Methodology

It is desired to obtain the ocean wave spectrum distribution from bistatic HF-radar data. The radar cross section that represents the bistatic HF-radar data is expressed by Equation (3.27). As previously mentioned, the problem of solving for the directional ocean wave spectrum in Equation (3.27) is a nonlinear ill-posed problem. Therefore, in seeking an optimal solution, the problem should be regularized.

The directional ocean wave spectrum was extracted from synthetic HF-radar data, generated by simulation using Matlab® for different radar and ocean configurations. For the non-directional spectrum, the Pierson-Moskowitz model, described by Equation (2.23), was used. As for the directional spread function, the Longuet-Higgins model in Equation (2.24) was chosen. In order to speed up the optimization, the nondirectional ocean wave spectrum was limited to 256 points, which resulted in a "spiky" returned signal. This choice does not jeopardize the presented method.

In the extraction process, the regularized nonlinear least-squares method presented in Section 3.2.3 was used, specifically the Tikhonov Regularization in Hilbert scales, described by Equation (3.8). Since both input and output spaces are Eu-

clidean, the norms $\|\cdot\|_X$ and $\|\cdot\|_Y$ can be substituted by the L^2-norm described by Equation (3.1) for $p = 2$. Regarding the $\mathscr{Y}$ operator, the second-order differential operator D^2 described by Equation (3.9) was used. The regularization parameter was iteratively chosen by using the process described by Equation (3.11). The method was implemented by modifying the `levenbergMarquardt` algorithm in Matlab® to include the regularization parameter. After modification, the nonlinear least-squares function `lsqnonlin` was used.

To attest to the efficacy of the proposed method, the root-mean-square error e and the normalized root-mean-square error$RMSE$ of each measurement were presented. For a given estimated variable $\mathbf{X}$ with $\mathbf{X_r}$ being the reference (or ground truth), both of size N, these error measurements are defined as

$$RMSE_X = \sqrt{\frac{1}{N}\sum_{n=1}^{N} |\mathbf{X}[\,n\,] - \mathbf{X_r}[\,n\,]|^2},$$

and

$$e_X = \frac{RMSE_X}{\max(\mathbf{X_r})}.$$

For the investigations in this thesis, synthetic bistatic HF-Radar data was generated from different configurations, where wind speed, wind direction, and bistatic radar configuration are changed in order to observe how the extraction method is affected by each of these parameters. Moreover, traditional meteorological measurements, such as significant wave height and peak wave period, will also be included in the error analysis. These meteorological measurements, however, will be obtained from the directional ocean wave spectrum, and are thus not strictly the objective of the extraction.

The objective function was designed such that no spectral model was assumed

for the non-directional spectrum, while the Longuet-Higgins directional function was assumed for the directional spread function. The translation property found between $T(Y_1)$ and $T(Y_2)$ was exploited, and $T(Y_2)$ was derived from $T(Y_1)$ by spline interpolation and extrapolation using the Matlab® function `interp1`. Therefore, the variables for which the problem will be solved are the non-directional ocean wave spectrum T, or more specifically $\hat{S}$, mean wind direction $\bar{\theta}$, and spreading factor s.

3.5 Extraction Results and Discussion

3.5.1 Changes in Wind Speed

Figure 3.2 presents the synthetic second-order cross section simulation for different wind speeds while Figures 3.3 and 3.4 present the original and extracted non-directional spectrum and directional spread function for each case. Tables 3.1 and 3.2 present, respectively, the normalized and RMS errors for the extracted spectrum and for the significant wave height for each wind speed. For all results, errors in the peak wave period T_{max} were equal to zero, meaning that the peak wave period was retrieved exactly in all experiments with the new optimization-based method. It must be emphasized that, at this point, these are results for the idealized synthetic data that has no noise content.

3.5.2 Changes in Wind Direction

Figure 3.5 presents the synthetic second-order cross section simulation for different wind speeds while Figures 3.6 and 3.7 present the original and extracted non-

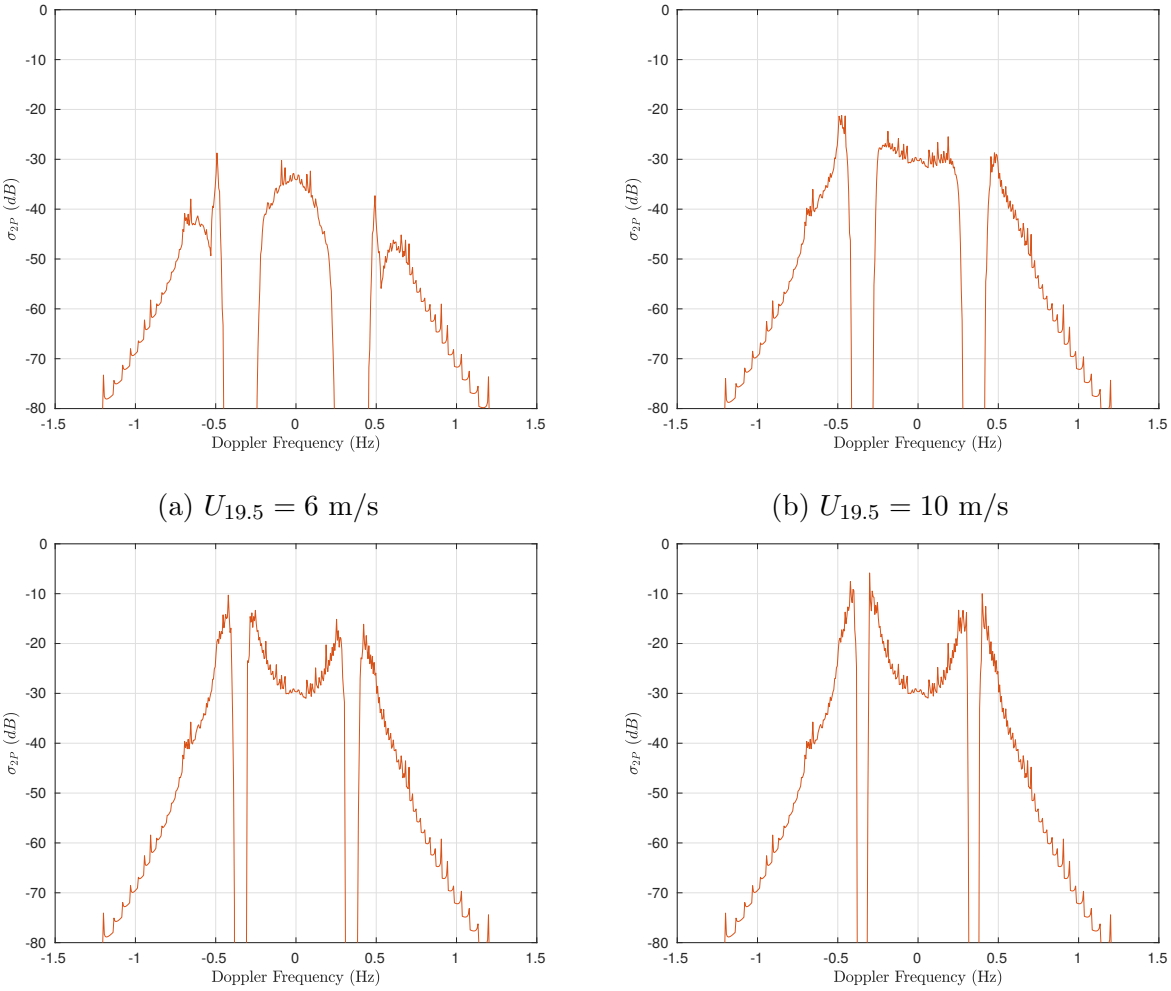

(a) $U_{19.5} = 6$ m/s

(b) $U_{19.5} = 10$ m/s

(c) $U_{19.5} = 18$ m/s

(d) $U_{19.5} = 25$ m/s

Figure 3.2: Synthetic second-order bistatic cross section under different wind speeds. Transmitter frequency $f_o = 13.385$ MHz, bistatic angle $\phi = 30°$, transmitter look direction $\theta_{01} = 60°$, spreading factor $s = 1.85$, and wind direction $\theta_w = \bar{\theta} = 15°$.

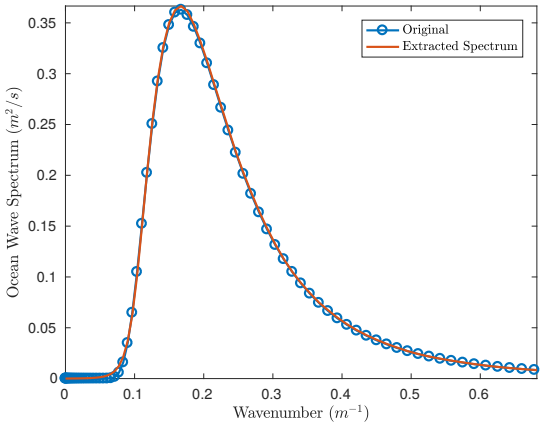

(a) $U_{19.5} = 6$ m/s

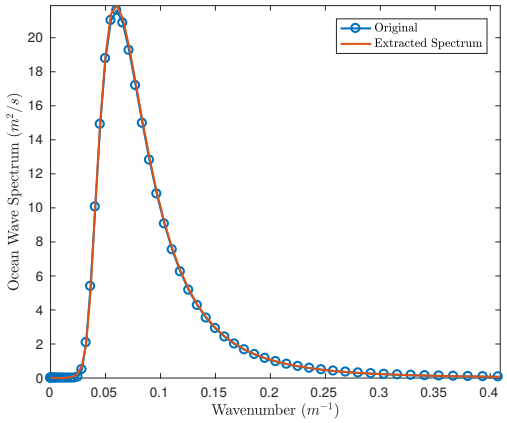

(b) $U_{19.5} = 10$ m/s

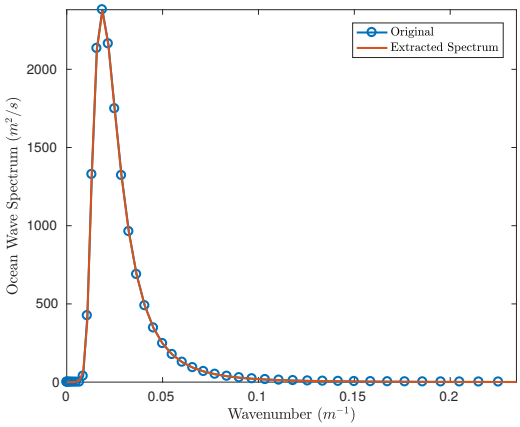

(c) $U_{19.5} = 18$ m/s

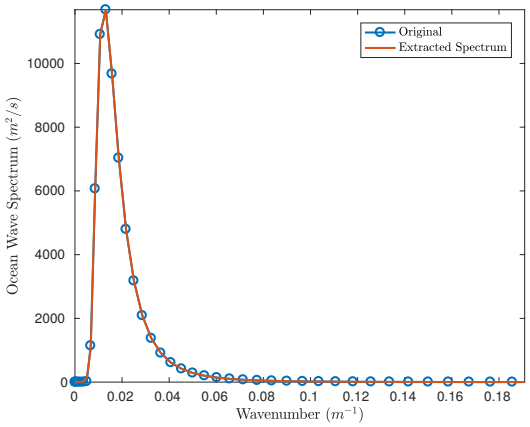

(d) $U_{19.5} = 22$ m/s

Figure 3.3: Comparison between the original and extracted non-directional ocean wave spectra for different wind speeds. Transmitter frequency $f_o = 13.385$ MHz, bistatic angle $\phi = 30°$, transmitter look direction $\theta_{01} = 60°$, spreading factor $s = 1.85$, and wind direction $\theta_w = \bar{\theta} = 15°$.

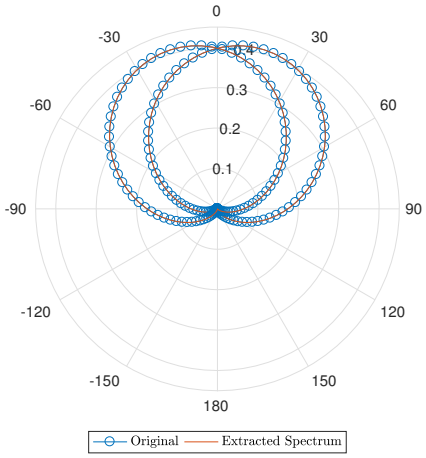

(a) $U_{19.5} = 6$ m/s

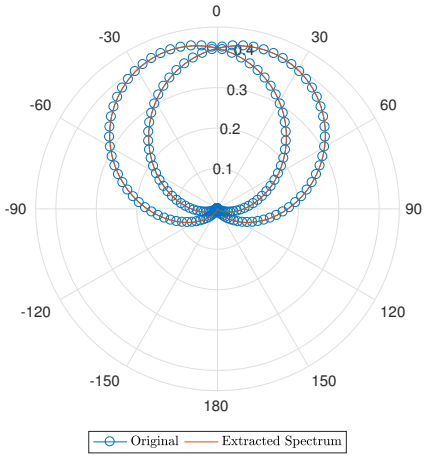

(b) $U_{19.5} = 10$ m/s

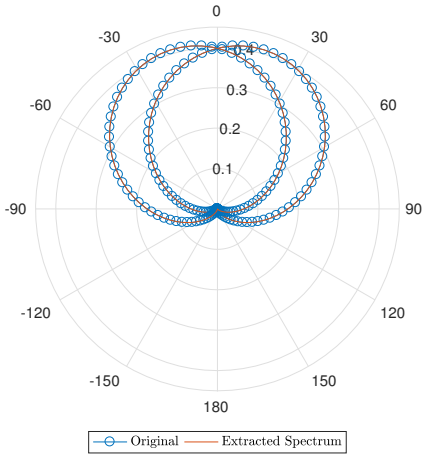

(c) $U_{19.5} = 18$ m/s

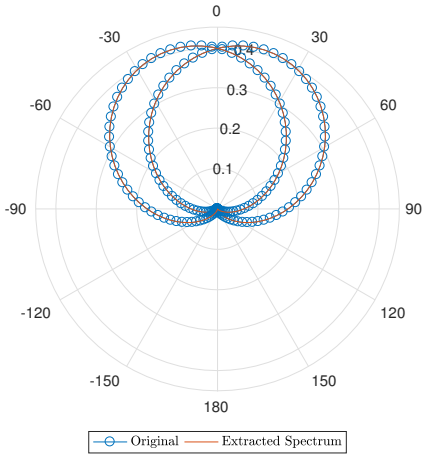

(d) $U_{19.5} = 22$ m/s

Figure 3.4: Comparison between the original and extracted ocean wave directional spread functions for different wind speeds. Transmitter frequency $f_o = 13.385$ MHz, bistatic angle $\phi = 30°$, transmitter look direction $\theta_{01} = 60°$, spreading factor $s = 1.85$, and wind direction $\theta_w = \bar{\theta} = 15°$.

Table 3.1: Normalized root-mean-square error for the ocean wave spectrum extraction under different wind speeds

$U_{19.5}$ (m/s)	$e_{\hat{S}}$	$e_{\bar{\theta}}$	e_s	$e_{\overline{H_{1/3}}}$
6	0.28%	0.03%	0.04%	1.65%
10	0.24%	0.05%	0.04%	0.25%
18	0.16%	0.01%	0.00%	0.19%
22	0.09%	0.09%	0.09%	0.11%

Table 3.2: Root-mean-square error for the ocean wave spectrum extraction under different wind speeds

$U_{19.5}$ (m/s)	$RMSE_{\hat{S}}$ (m^2/s)	$RMSE_{\bar{\theta}}$ (°)	$RMSE_s$	$RMSE_{\overline{H_{1/3}}}$ (m)
6	1.02×10^{-3}	4.33×10^{-3}	6.50×10^{-4}	8.93×10^{-3}
10	5.39×10^{-2}	8.14×10^{-3}	7.70×10^{-4}	4.06×10^{-3}
18	3.83	1.22×10^{-3}	6.00×10^{-5}	9.11×10^{-3}
22	10.03	1.28×10^{-2}	1.61×10^{-3}	7.73×10^{-3}

directional spectrum and directional spread function for different wind directions. Tables 3.3 and 3.4 present, respectively, the normalized and RMS errors for the extracted spectrum and for the significant wave height for each wind direction. For all results, as mentioned previously, errors in the peak wave period T_{max} were equal to zero.

3.5.3 Changes in Spreading Factor

Figure 3.8 presents the synthetic second-order cross section simulation for different values for the spreading factor s, while Figures 3.9 and 3.10 present the original and extracted non-directional spectrum and directional spread function for each case. Tables 3.5 and 3.6 present, respectively, the normalized and RMS errors for the extracted spectrum and for the significant wave height for each spreading factor. For all results, errors in the peak wave period T_{max} were equal to zero.

3.5.4 Changes in Bistatic Configuration

Figure 3.11 presents the synthetic second-order cross section simulation for different combinations of bistatic angle ϕ and transmitter look direction θ_{01}, while Figures 3.12 and 3.13 present the original and extracted non-directional spectrum and directional spread function for each case. Tables 3.7 and 3.8 present, respectively, the normalized and RMS errors for the extracted spectrum and for the significant wave height for each combination. For all results, errors in the peak wave period T_{max} were equal to zero.

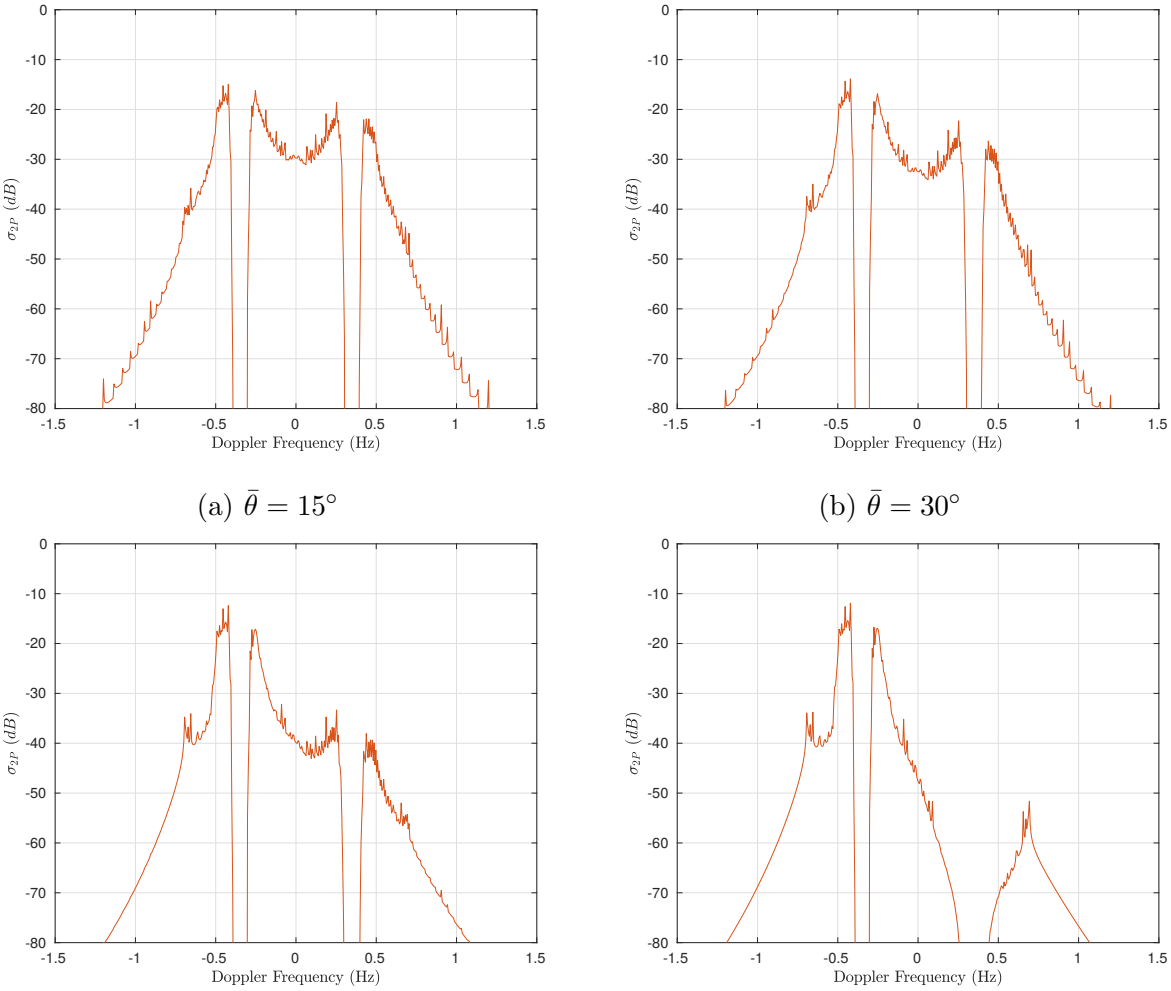

(a) $\bar{\theta} = 15°$

(b) $\bar{\theta} = 30°$

(c) $\bar{\theta} = 60°$

(d) $\bar{\theta} = 90°$

Figure 3.5: Synthetic second-order bistatic cross section under different wind directions. Transmitter frequency $f_o = 13.385$ MHz, bistatic angle $\phi = 30°$, transmitter look direction $\theta_{01} = 60°$, spreading factor $s = 1.85$, and wind speed $U_{19.5} = 15$ m/s.

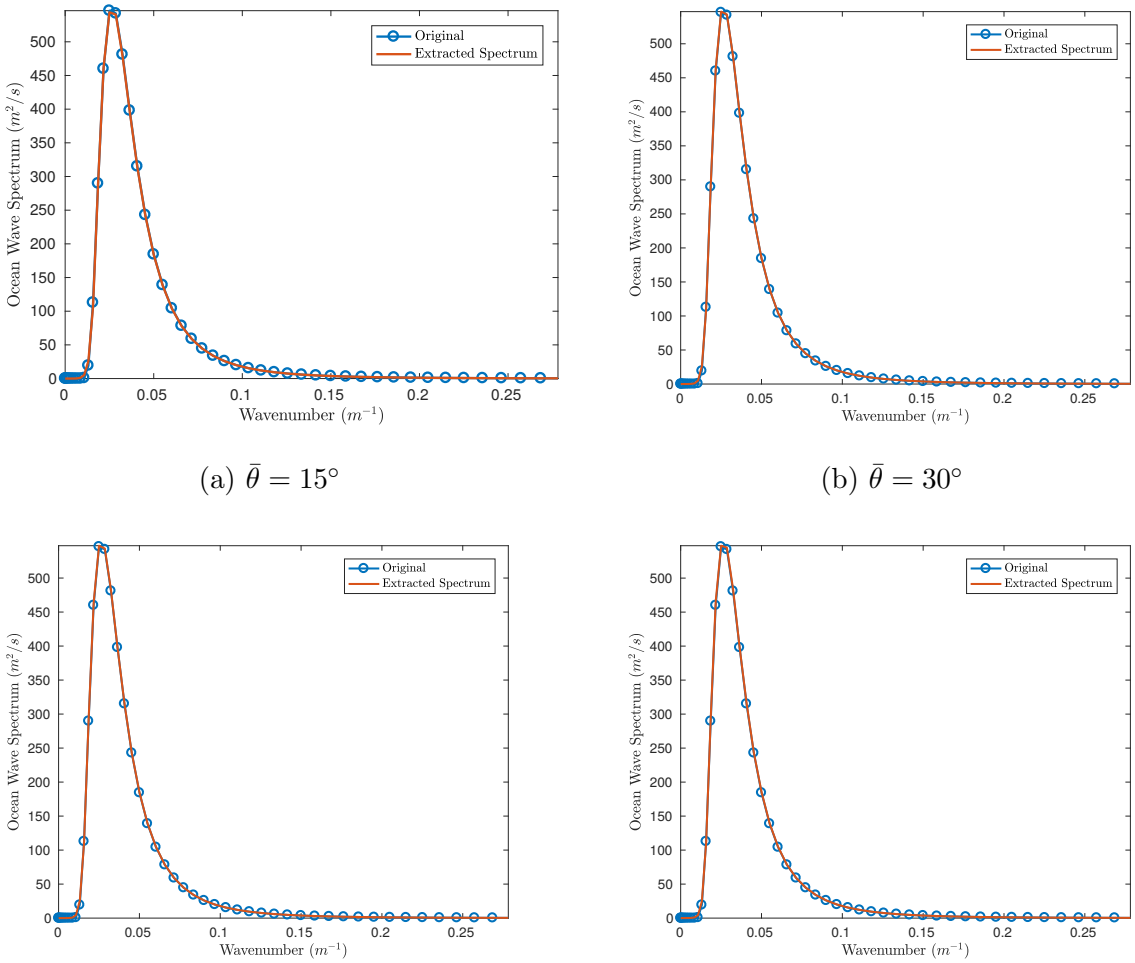

(a) $\bar{\theta} = 15°$

(b) $\bar{\theta} = 30°$

(c) $\bar{\theta} = 60°$

(d) $\bar{\theta} = 90°$

Figure 3.6: Comparison between the original and extracted non-directional ocean wave spectra for different wind directions. Transmitter frequency $f_o = 13.385$ MHz, bistatic angle $\phi = 30°$, transmitter look direction $\theta_{01} = 60°$, spreading factor $s = 1.85$, and wind speed $U_{19.5} = 15$ m/s.

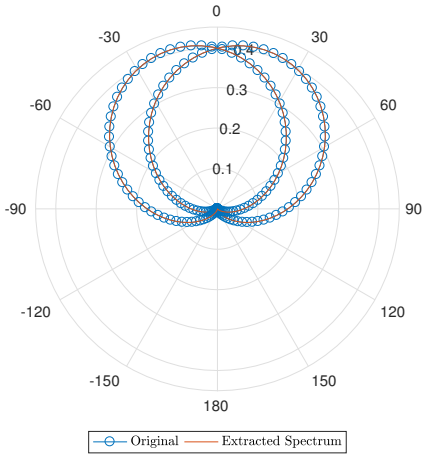

(a) $\bar{\theta} = 15°$

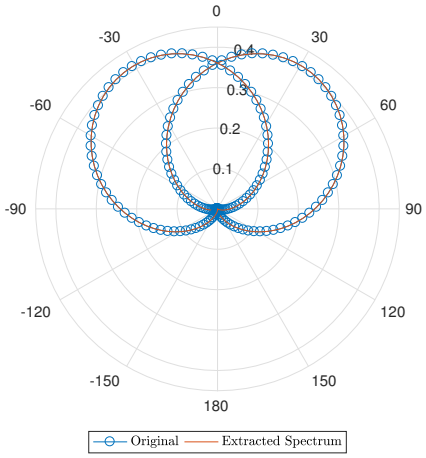

(b) $\bar{\theta} = 30°$

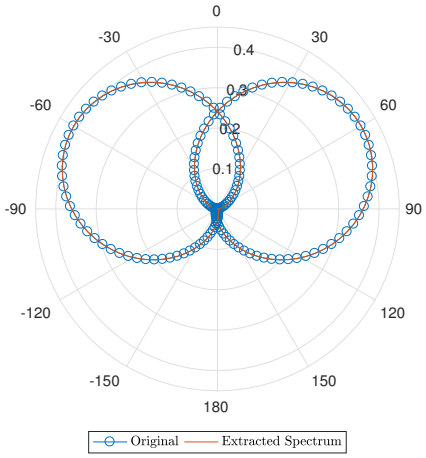

(c) $\bar{\theta} = 60°$

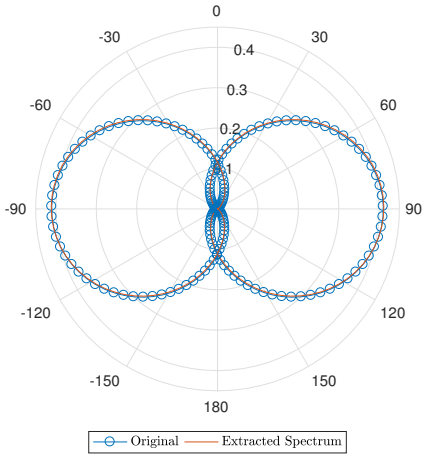

(d) $\bar{\theta} = 90°$

Figure 3.7: Comparison between the original and extracted ocean wave directional spread functions for different wind directions. Transmitter frequency $f_o = 13.385$ MHz, bistatic angle $\phi = 30°$, transmitter look direction $\theta_{01} = 60°$, spreading factor $s = 1.85$, and wind speed $U_{19.5} = 15$ m/s.

Table 3.3: Normalized root-mean-square error for the ocean wave spectrum extraction under different wind directions

$\bar{\theta}$ (°)	$e_{\hat{S}}$	$e_{\bar{\theta}}$	e_s	$e_{\overline{H_{1/3}}}$
15°	0.13%	0.10%	0.12%	0.24%
30°	0.11%	0.02%	0.03%	0.07%
60°	0.11%	0.23%	0.34%	0.09%
90°	0.13%	0.89%	0.67%	0.21%

Table 3.4: Root-mean-square error for the ocean wave spectrum extraction under different wind directions

$\bar{\theta}$ (°)	$RMSE_{\hat{S}}$ (m^2/s)	$RMSE_{\bar{\theta}}$ (°)	$RMSE_s$	$RMSE_{\overline{H_{1/3}}}$ (m)
15°	7.12×10^{-1}	1.57×10^{-2}	2.15×10^{-3}	8.46×10^{-3}
30°	6.45×10^{-1}	7.14×10^{-3}	6.10×10^{-4}	2.44×10^{-3}
60°	5.90×10^{-1}	1.35×10^{-1}	6.36×10^{-3}	3.02×10^{-3}
90°	7.12×10^{-1}	8.05×10^{-1}	1.24×10^{-2}	7.39×10^{-3}

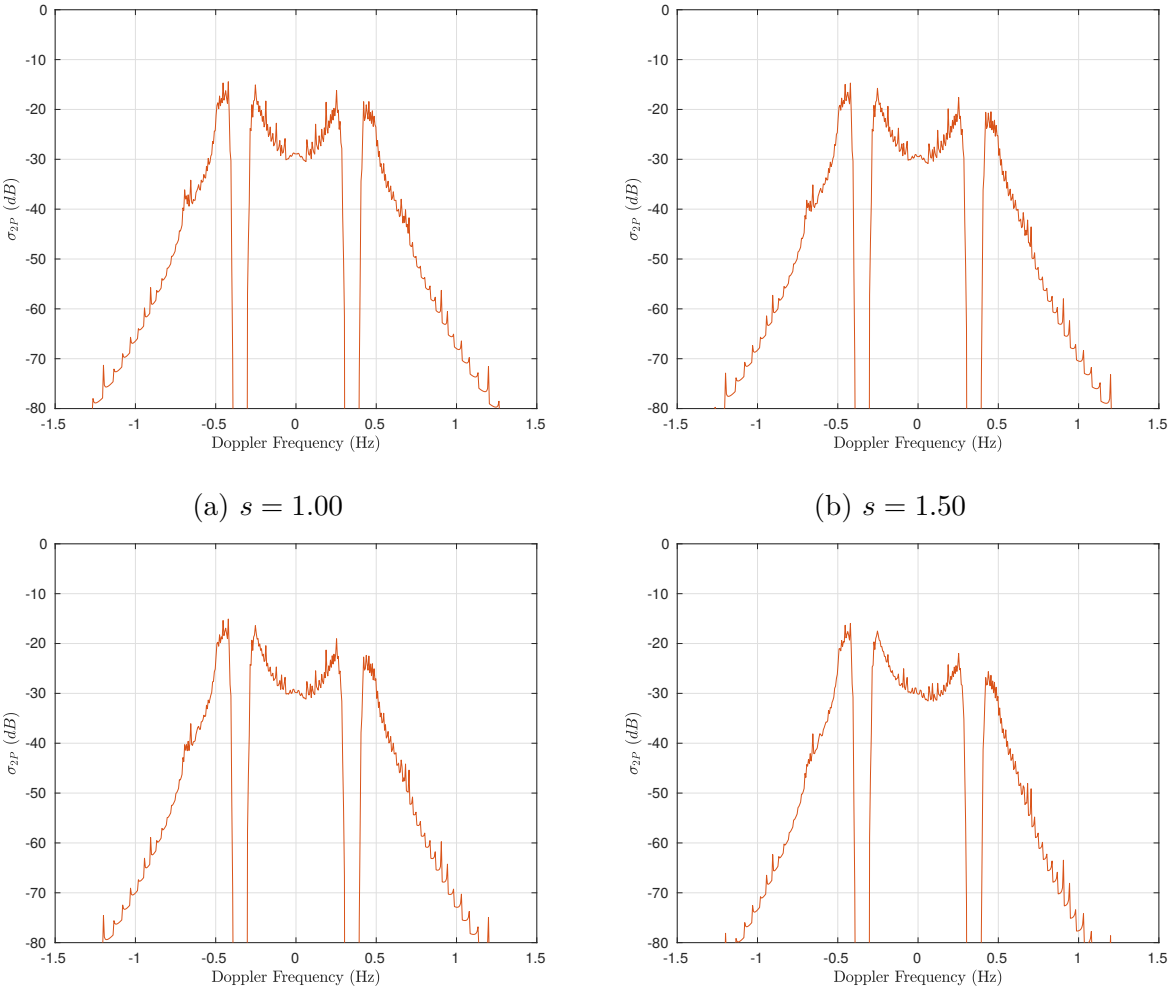

(a) $s = 1.00$

(b) $s = 1.50$

(c) $s = 2.00$

(d) $s = 3.00$

Figure 3.8: Synthetic second-order bistatic cross section under different spreading factors. Transmitter frequency $f_o = 13.385$ MHz, wind speed $U_{19.5} = 15$ m/s, and wind direction $\theta_w = \bar{\theta} = 15°$.

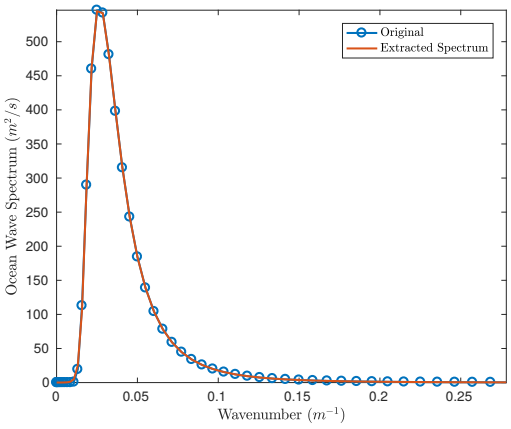

(a) $s = 1.00$

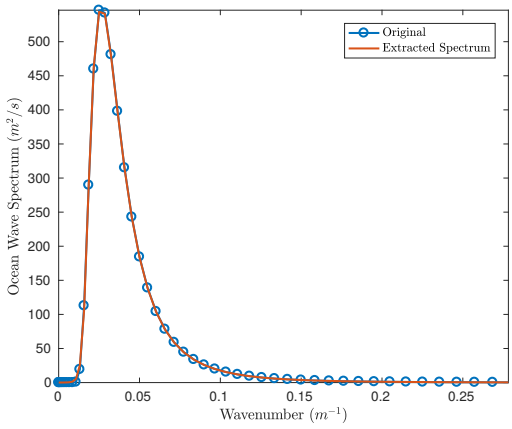

(b) $s = 1.50$

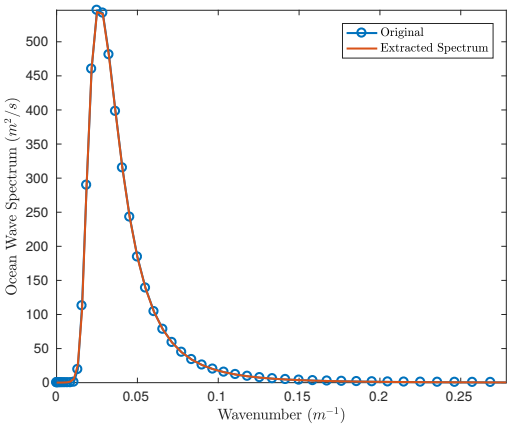

(c) $s = 2.00$

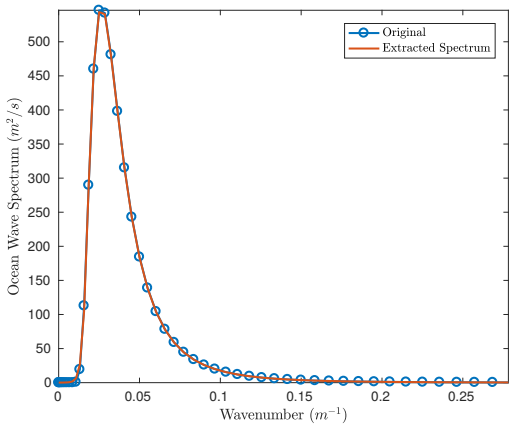

(d) $s = 3.00$

Figure 3.9: Comparison between the original and extracted non-directional ocean wave spectra for different spreading factors. Transmitter frequency $f_o = 13.385$ MHz, wind speed $U_{19.5} = 15$ m/s, and wind direction $\theta_w = \bar{\theta} = 15°$.

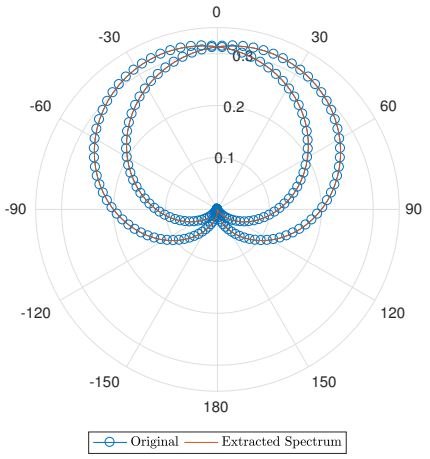

(a) $s = 1.00$

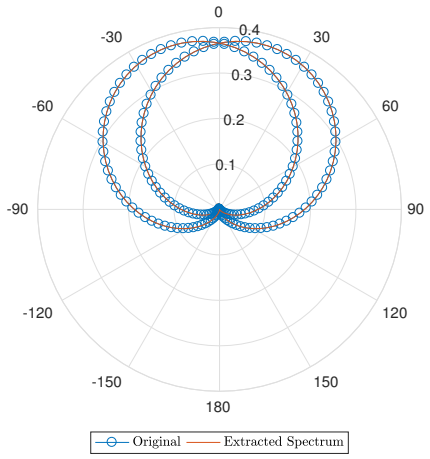

(b) $s = 1.50$

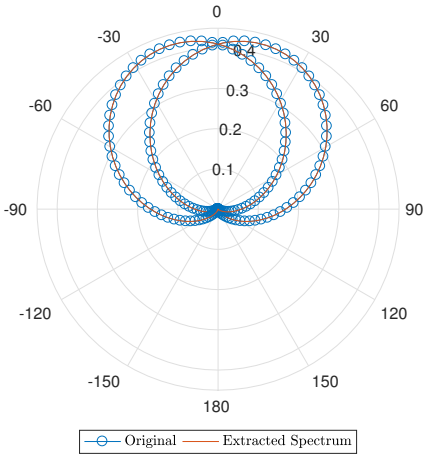

(c) $s = 2.00$

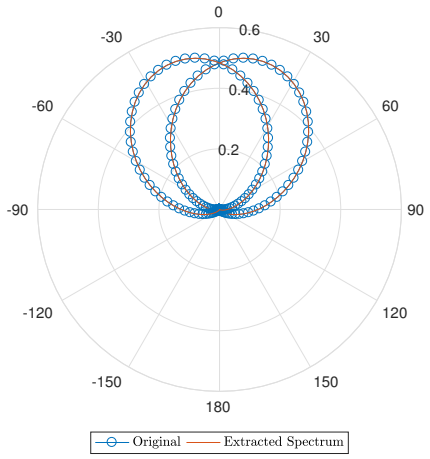

(d) $s = 3.00$

Figure 3.10: Comparison between the original and extracted ocean wave directional spread functions for different spreading factors. Transmitter frequency $f_o = 13.385$ MHz, wind speed $U_{19.5} = 15$ m/s, and wind direction $\theta_w = \bar{\theta} = 15°$.

Table 3.5: Normalized root-mean-square error for the ocean wave spectrum extraction under different spreading factors

s	$e_{\hat{S}}$	$e_{\bar{\theta}}$	e_s	$e_{\overline{H_{1/3}}}$
1.00	0.12%	0.12%	0.13%	0.09%
1.50	0.13%	0.11%	0.12%	0.20%
2.00	0.14%	0.08%	0.09%	0.22%
3.00	0.15%	0.03%	0.04%	0.20%

Table 3.6: Root-mean-square error for the ocean wave spectrum extraction under different spreading factors

s	$RMSE_{\hat{S}}$ (m^2/s)	$RMSE_{\bar{\theta}}$ (°)	$RMSE_s$	$RMSE_{\overline{H_{1/3}}}$ (m)
1.00	6.68×10^{-1}	1.86×10^{-2}	1.32×10^{-3}	3.17×10^{-3}
1.50	7.28×10^{-1}	1.67×10^{-2}	1.82×10^{-3}	6.70×10^{-3}
2.00	7.74×10^{-1}	1.25×10^{-2}	1.84×10^{-3}	7.56×10^{-3}
3.00	8.41×10^{-1}	5.38×10^{-3}	1.28×10^{-3}	6.89×10^{-3}

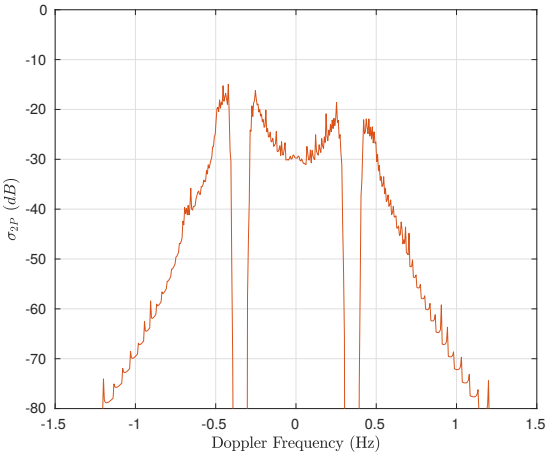

(a) $\phi = 30.00°,\ \theta_{01} = 60.00°$

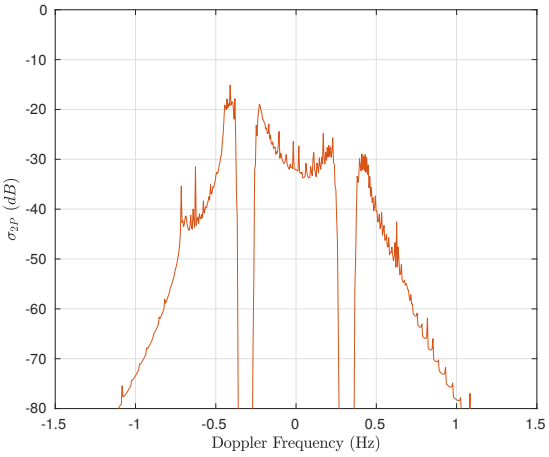

(b) $\phi = 45.00°,\ \theta_{01} = 30.00°$

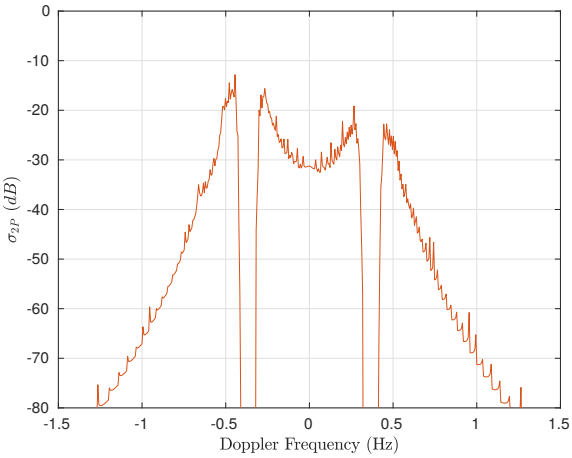

(c) $\phi = 15.78°,\ \theta_{01} = 66.50°$

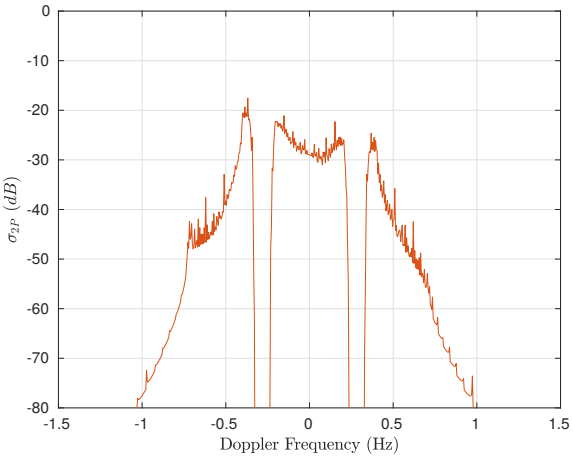

(d) $\phi = 55.20°,\ \theta_{01} = 35.50°$

Figure 3.11: Synthetic second-order bistatic cross section under different bistatic configurations. Transmitter frequency $f_o = 13.385$ MHz, spreading factor $s = 1.85$, wind speed $U_{19.5} = 15$ m/s, and wind direction $\theta_w = \bar{\theta} = 15°$.

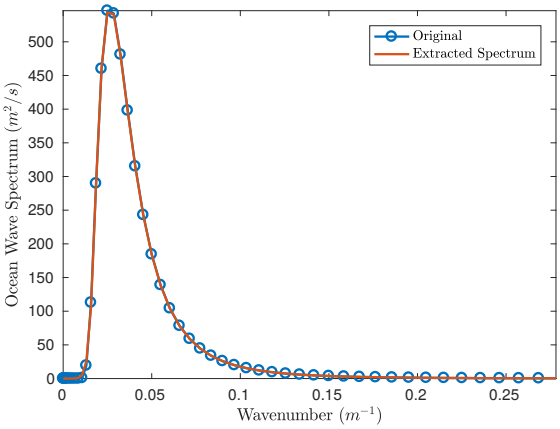

(a) $\phi = 30.00°,\ \theta_{01} = 60.00°$

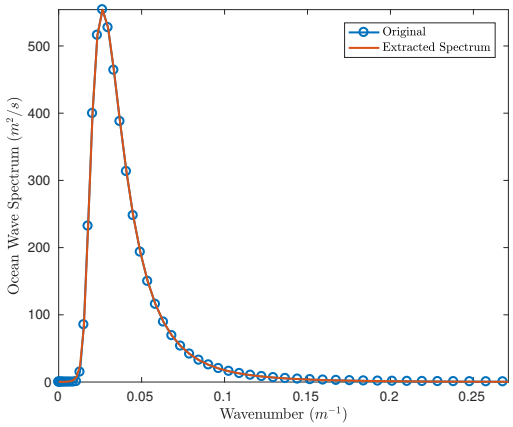

(b) $\phi = 45.00°,\ \theta_{01} = 30.00°$

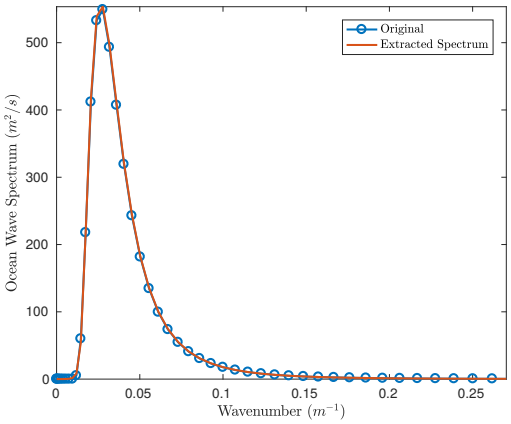

(c) $\phi = 15.78°,\ \theta_{01} = 66.50°$

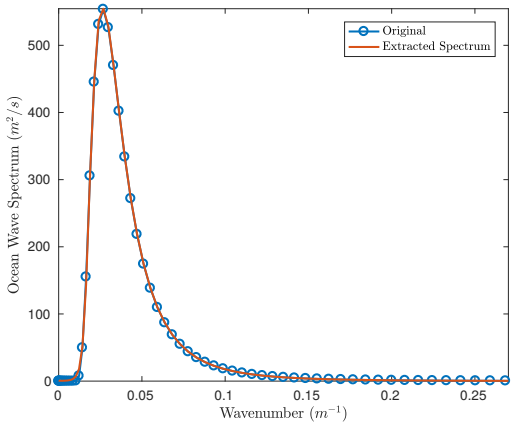

(d) $\phi = 55.20°,\ \theta_{01} = 35.50°$

Figure 3.12: Comparison between the original and extracted non-directional ocean wave spectra for different bistatic configurations. Transmitter frequency f_o = 13.385 MHz, spreading factor s = 1.85, wind speed $U_{19.5}$ = 15 m/s, and wind direction $\theta_w = \bar{\theta} = 15°$.

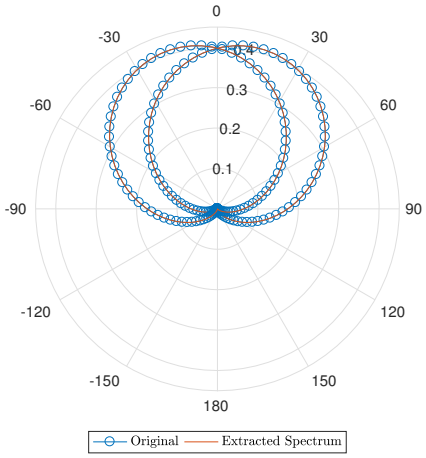

(a) $\phi = 30.00°,\ \theta_{01} = 60.00°$

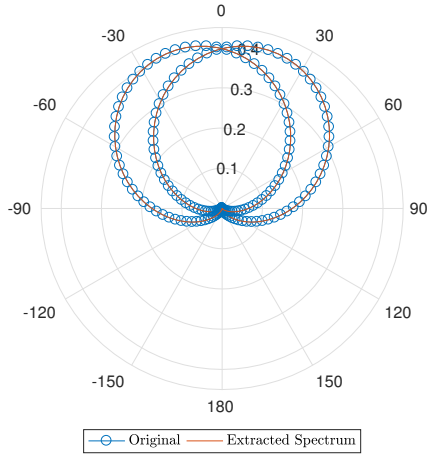

(b) $\phi = 45.00°,\ \theta_{01} = 30.00°$

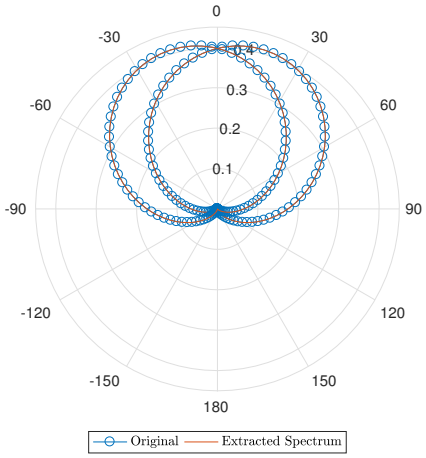

(c) $\phi = 15.78°,\ \theta_{01} = 66.50°$

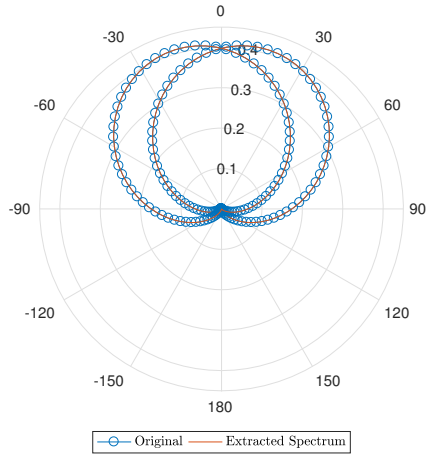

(d) $\phi = 55.20°,\ \theta_{01} = 35.50°$

Figure 3.13: Comparison between the original and extracted ocean wave directional spread functions for different bistatic configurations. Transmitter frequency $f_o = 13.385$ MHz, spreading factor $s = 1.85$, wind speed $U_{19.5} = 15$ m/s, and wind direction $\theta_w = \bar{\theta} = 15°$.

Table 3.7: Normalized root-mean-square error for the ocean wave spectrum extraction under different bistatic configurations

ϕ (°)	θ_{01} (°)	$\theta_{\mathbf{N}}$ (°)	$e_{\hat{S}}$	$e_{\bar{\theta}}$	e_s	$e_{\overline{H_{1/3}}}$
30.00°	60.00°	90.00°	0.13%	0.10%	0.11%	0.25%
45.00°	30.00°	85.00°	0.14%	0.04%	0.02%	0.02%
15.78°	66.50°	82.28°	0.15%	0.20%	0.14%	0.39%
55.20°	35.50°	19.70°	0.21%	0.09%	0.11%	0.02%

Table 3.8: Root-mean-square error for the ocean wave spectrum extraction under different bistatic configurations

ϕ (°)	θ_{01} (°)	$\theta_{\mathbf{N}}$ (°)	$RMSE_{\hat{S}}$ (m^2/s)	$RMSE_{\bar{\theta}}$ (°)	$RMSE_s$	$RMSE_{\overline{H_{1/3}}}$ (m)
30.00°	60.00°	90.00°	7.12×10^{-1}	1.57×10^{-2}	2.15×10^{-3}	8.46×10^{-3}
45.00°	30.00°	85.00°	8.10×10^{-1}	5.95×10^{-3}	4.30×10^{-4}	6.50×10^{-4}
15.78°	66.50°	82.28°	8.37×10^{-1}	3.02×10^{-2}	2.60×10^{-3}	1.34×10^{-2}
55.20°	35.50°	19.70°	1.16	1.37×10^{-2}	2.04×10^{-3}	7.90×10^{-4}

3.5.5 Discussion

As can be observed from the results presented in the previous section, the presented method successfully extracted the directional ocean wave spectrum from the second-order bistatic HF radar cross section of the ocean surface with fairly high accuracy.

Regarding errors in the non-directional spectrum, the accuracy of the extraction was slightly affected by changes in the wind direction, even though the results are still accurate. Larger errors are expected at low wind speeds, since in these cases there is not enough energy in the spectral region observed by the radar [91]. No particular trend was observed in the extraction error for the non-directional spectrum due to changes in the wind direction or in the bistatic configuration.

As for errors in the directional spectrum, the mean wind direction and spreading function seem to be more affected by changes in the wind speed. In this case, again, the normalized root-mean-square error was very small, even in the worst case. With respect to changes in the wind speed, the errors were very small in all cases, with a higher error value in the $U_{19.5} = 22$ m/s case. No particular trends were noticed in the errors by changing the spreading factor s.

Errors in the significant wave height follow the trend of the non-directional ocean wave spectrum, since the former was measured from the latter. The peak wave period, also obtained from the ocean wave spectrum, had errors equal to zero in all the cases, meaning that the extraction method successfully captured the peak position of the ocean wave spectra exactly.

The extraction method also proved to be robust to changes in the bistatic configuration, with very small error values for all the cases and no noticeable trend.

As expected, the RMS error was very low in all the cases, with the exception of the non-directional spectrum error due to changes in the wind speed. In this case, however, the error is still very small if compared to the magnitudes of the spectrum, which indicates that the method is accurate. It must be emphasized, however, that these results were derived from the application of the presented method to an ideal case, in which there is no noise or presence of first-order scattering. It is not expected that such close agreement would be obtained from real data.

It was also observed that the regularization parameter presented in (3.11) decreases monotonically with the discrepancy δ of the previous iteration, converging to an optimal parameter. This technique is analogous to the one presented by Oraintara *et al.* [122], where the optimal regularization parameter for the linear Tikhonov regularization is reached through an iterative process. In all presented cases, the regularization parameter converged monotonically to zero, which is expected for a noiseless case. In a noise-contaminated case, however, the regularization parameter should converge to a non-zero value.

3.6 General Chapter Summary

In this chapter, the extraction of the ocean wave spectrum from the second-order bistatic cross section was presented. In Section 3.3, a change of variables was introduced to the second-order bistatic cross-section presented by Gill [3], which allowed for further simplification of the expression, as well as to help identify the direct relationship between variables in the cross-section formulation. These changes later facilitated the extraction method.

In Section 3.2.2, the extraction method was presented. A brief explanation on regularized nonlinear least-squares and Tikhonov regularization in Hilbert spaces was provided, as well as a formulation for the regularization parameter. Then, the methodology was presented, detailing the approach to the ocean wave spectrum extraction using the techniques presented earlier.

Section 3.5 contained the results of the directional ocean wave spectrum extraction, providing both normalized and root-mean-square errors for each measurement, as well as for significant wave height and peak wave period. The method proved to be successful in extracting the ocean wave spectrum in both its directional and non-directional components, doing so with high accuracy, with normalized root-mean-square errors varying between 0% and 0.89% for the extracted parameters, and 1.65% reaching on the worst case for the significant wave height, an indirect measurement.

Even though the proposed method has been proven successful in the extraction of the ocean wave spectrum from the second-order bistatic cross section, the second-order cross section is not available as an independent measurement in the field. However, being the two most energetic components of the received signal, the first- and second- order cross sections combined can provide a more realistic approach to the problem. Also, these results, provided as a proof-of-concept for usefulness of the method, were obtained for noise-free simulated data, which is, again, not realistic. In the next chapter, both these situations will be addressed, and the extraction method will be applied to measurements obtained in noisy environments in the presence of first-order scattering effects.

Chapter 4

Nonlinear Extraction of the Ocean Wave Spectrum from Noisy Bistatic HF Radar Data

4.1 Introduction

In the previous chapter, a new nonlinear extraction method of the directional ocean wave spectrum from bistatic HF radar data was presented. The method achieved a fair level of accuracy, being able to extract the directional spectrum from several different ocean conditions. The presented cases, however, do not represent realistic scenarios.

Every measurement, especially in an uncontrolled environment, is likely contaminated by noise. This is especially true for HF radar field data. To not take into account the presence of noise in the extraction method is to account only for the

best-case scenario. Therefore, the method's robustness to noise should be tested in order to determine if the method can be applied to field measurements.

Another point to be considered is that the second-order cross section is not available independent of other orders of scattering. Higher orders of scattering are, in general, less energetic than the lower ones, with the first-order being the most energetic. Consequently, in order to obtain a more realistic case, the first-order cross section should be considered in the extraction process.

This chapter takes both these aims into account in the extraction process.

4.2 Noiseless Patch Scattering Cross Section

According to Equation (2.31), the patch scattering cross section per unit area of the ocean surface up to its second order can be written as

$$\sigma_P(\omega_d) = \sigma_1(\omega_d) + \sigma_{2P}(\omega_d), \tag{4.1}$$

where σ_1 is the first-order cross section described by Eq. (2.35) and σ_{2P} is the second-order cross section described by Eq. (3.27) after simplification. Since (4.1) contains the two most energetic scattering cross section orders, the total cross section σ can be approximated as σ_P. Throughout the text, this approximation will be considered.

Since the scattering occurs at the same patch of the ocean for both first- and patch scattering second-order, the ocean wave spectrum for both first-order and the first scatter of the second-order scattering can be considered the same. This conclusion plays a role in the extraction of the directional ocean wave spectrum, since the first-order cross section also carries information about it.

The same methodology as was presented in Section 3.4 will be applied to the patch scattering cross section. However, only the changes in variables that were identified to impact the accuracy of the extraction — i.e. wind speed and wind direction — will be considered.

4.2.1 Extraction Results

4.2.1.1 Changes in Wind Speed

Figure 4.1 presents the synthetic patch scattering cross section simulation for different wind speeds, while Figures 4.2 and 4.3 show the original and extracted non-directional spectrum and directional spread function for each case. Tables 4.1 and 4.2 present, respectively, the normalized and RMS errors for the extracted spectrum and for indirect meteorological measurements for each wind speed and direction. For all results, errors in the peak wave period T_{max} were equal to zero, meaning that the peak wave period was retrieved exactly in all experiments.

4.2.1.2 Changes in Wind Direction

Figure 4.4 presents the synthetic patch scattering cross section simulation for different wind directions, while Figures 4.5 and 4.6 show the original and extracted non-directional spectrum and directional spread function for each case. Tables 4.3 and 4.4 present, respectively, the normalized and RMS errors for the extracted spectrum and for indirect meteorological measurements for each wind speed and direction. For all results, errors in the peak wave period T_{max} were equal to zero, meaning that the peak wave period was retrieved exactly in all experiments.

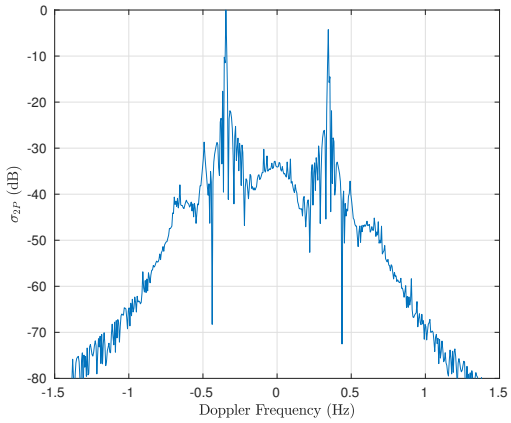

(a) $U_{19.5} = 6$ m/s

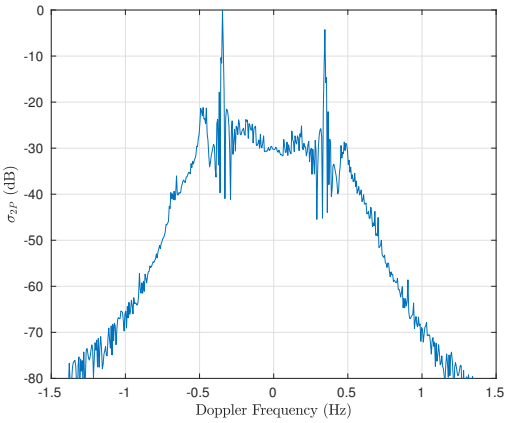

(b) $U_{19.5} = 10$ m/s

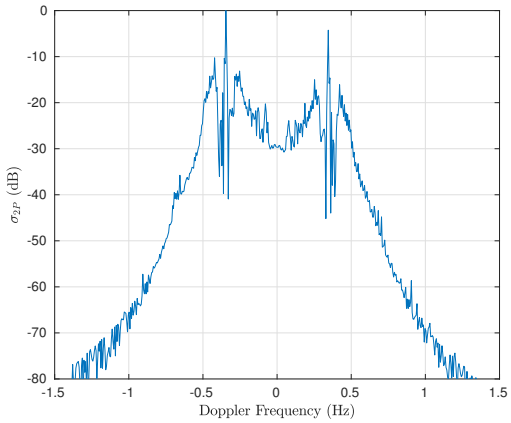

(c) $U_{19.5} = 18$ m/s

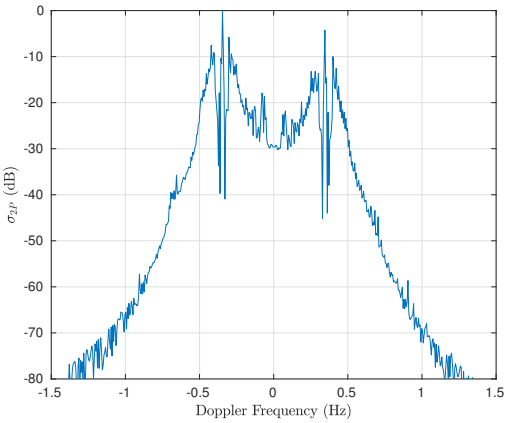

(d) $U_{19.5} = 22$ m/s

Figure 4.1: Synthetic patch scattering bistatic cross section under different wind speeds. Transmitter frequency $f_o = 13.385$ MHz, bistatic angle $\phi = 30°$, transmitter look direction $\theta_{01} = 60°$, spreading factor $s = 1.85$, and wind direction $\theta_w = \bar{\theta} = 15°$.

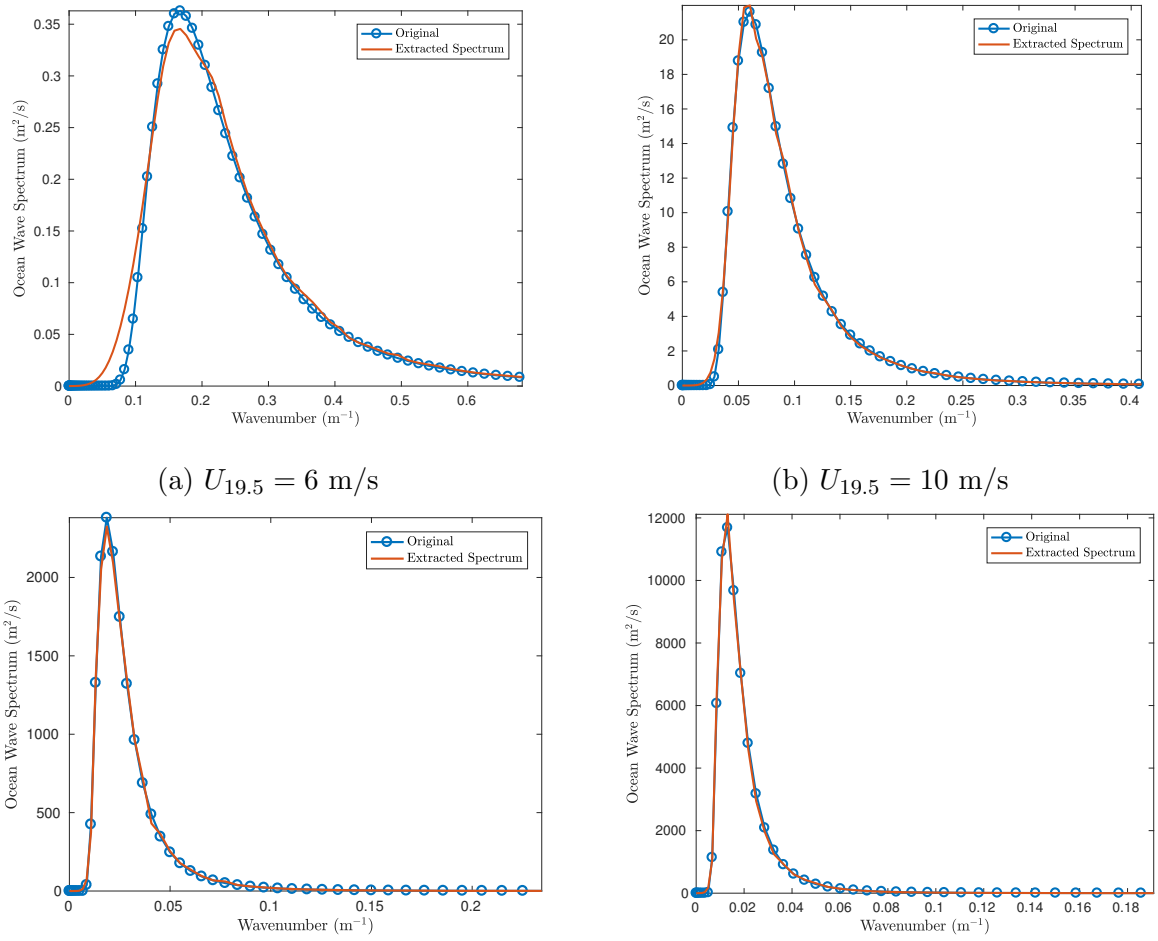

(a) $U_{19.5} = 6$ m/s

(b) $U_{19.5} = 10$ m/s

(c) $U_{19.5} = 18$ m/s

(d) $U_{19.5} = 22$ m/s

Figure 4.2: Comparison between the original and extracted non-directional ocean wave spectra for different wind speeds. Transmitter frequency $f_o = 13.385$ MHz, bistatic angle $\phi = 30°$, transmitter look direction $\theta_{01} = 60°$, spreading factor $s = 1.85$, and wind direction $\theta_w = \bar{\theta} = 15°$.

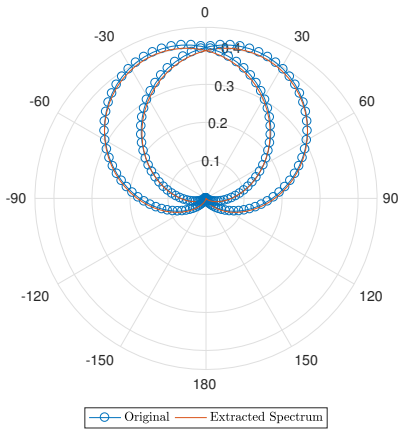

(a) $U_{19.5} = 6$ m/s

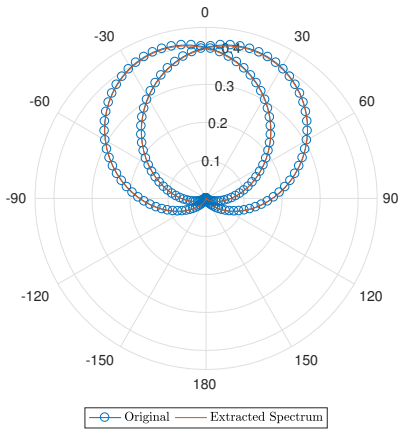

(b) $U_{19.5} = 10$ m/s

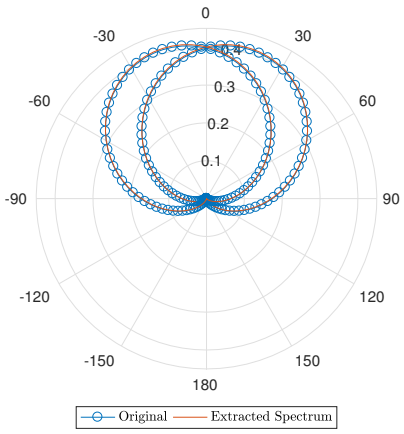

(c) $U_{19.5} = 18$ m/s

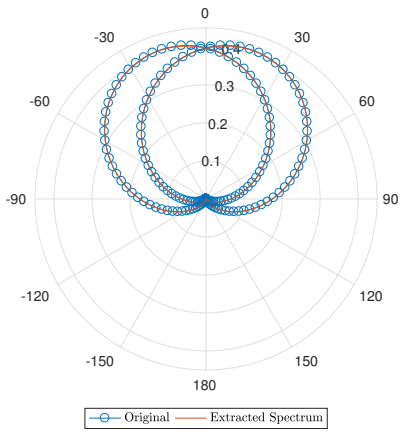

(d) $U_{19.5} = 22$ m/s

Figure 4.3: Comparison between the original and extracted ocean wave directional spread functions for different wind speeds. Transmitter frequency $f_o = 13.385$ MHz, bistatic angle $\phi = 30°$, transmitter look direction $\theta_{01} = 60°$, spreading factor $s = 1.85$, and wind direction $\theta_w = \bar{\theta} = 15°$.

Table 4.1: Normalized root-mean-square error for the ocean wave spectrum extraction from the patch cross section under different wind speeds

$U_{19.5}$ (m/s)	$e_{\hat{S}}$	$e_{\bar{\theta}}$	e_s	$e_{\overline{H_{1/3}}}$
6.00	2.53%	5.33%	4.44%	0.65%
10.00	0.66%	1.03%	1.27%	0.55%
18.00	0.43%	1.66%	1.80%	0.10%
22.00	0.41%	0.68%	0.62%	0.94%

Table 4.2: Root-mean-square error for the ocean wave spectrum extraction under different wind speeds

$U_{19.5}$ (m/s)	$RMSE_{\hat{S}}$ (m^2/s)	$RMSE_{\bar{\theta}}$ (°)	$RMSE_s$	$RMSE_{\overline{H_{1/3}}}$ (m)
6.00	9.19×10^{-3}	7.99×10^{-1}	8.22×10^{-2}	3.52×10^{-3}
10.00	1.42×10^{-1}	1.55×10^{-1}	2.35×10^{-2}	8.31×10^{-3}
18.00	10.20	2.48×10^{-1}	3.32×10^{-2}	4.78×10^{-3}
22.00	48.20	1.02×10^{-1}	1.15×10^{-2}	6.87×10^{-2}

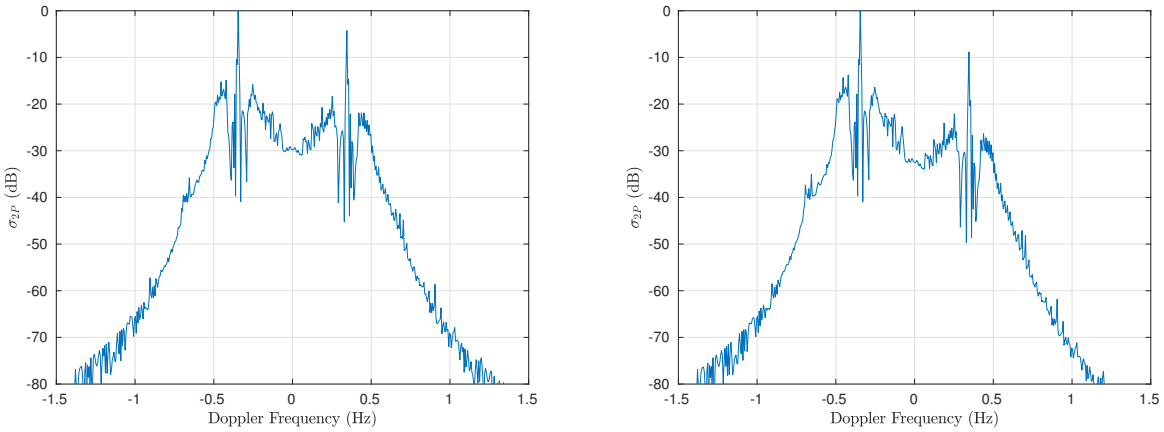

(a) $\bar{\theta} = 15°$

(b) $\bar{\theta} = 30°$

(c) $\bar{\theta} = 60°$

(d) $\bar{\theta} = 90°$

Figure 4.4: Synthetic patch scattering bistatic cross section under different wind directions. Transmitter frequency $f_o = 13.385$ MHz, bistatic angle $\phi = 30°$, transmitter look direction $\theta_{01} = 60°$, spreading factor $s = 1.85$, and wind speed $U_{19.5} = 15$ m/s.

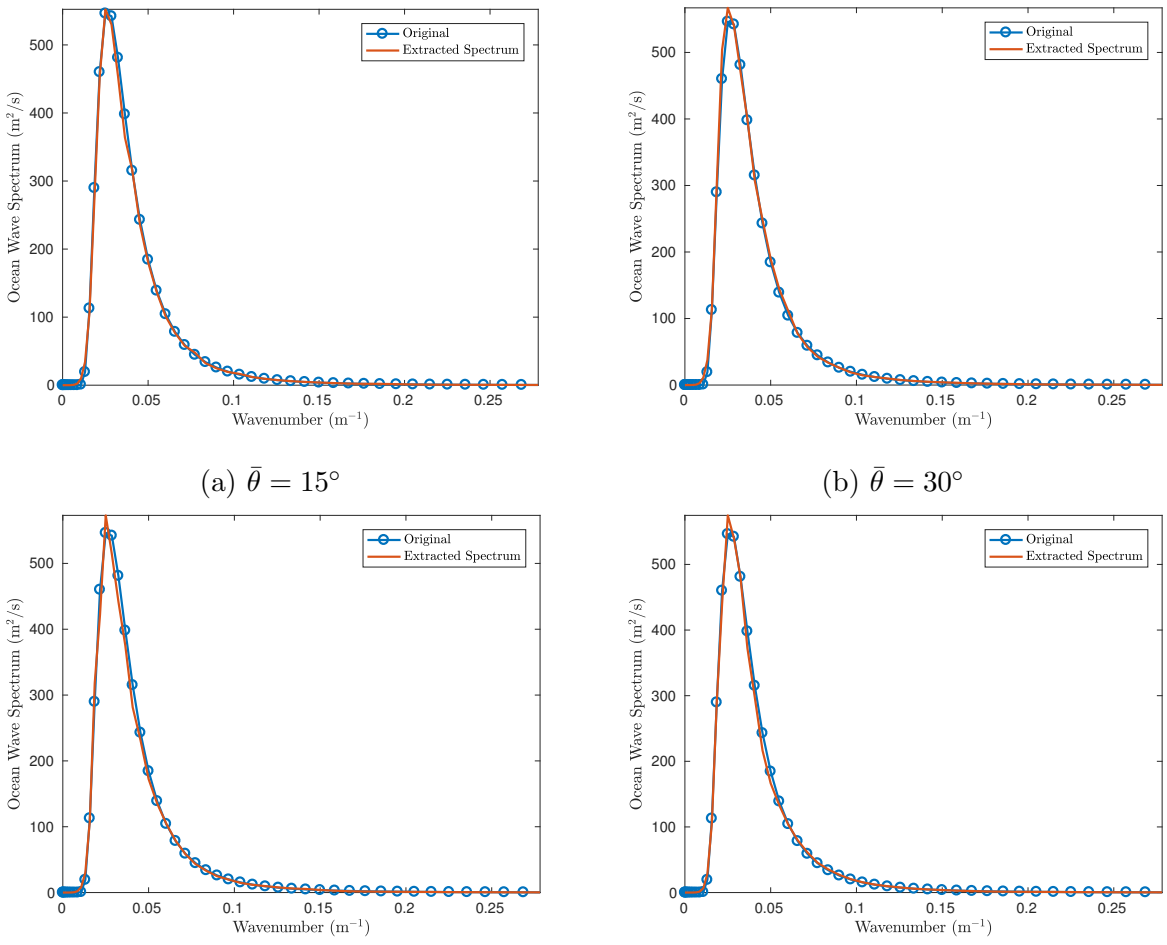

(a) $\bar{\theta} = 15°$

(b) $\bar{\theta} = 30°$

(c) $\bar{\theta} = 60°$

(d) $\bar{\theta} = 90°$

Figure 4.5: Comparison between the original and extracted non-directional ocean wave spectra for different wind directions. Transmitter frequency $f_o = 13.385$ MHz, bistatic angle $\phi = 30°$, transmitter look direction $\theta_{01} = 60°$, spreading factor $s = 1.85$, and wind speed $U_{19.5} = 15$ m/s.

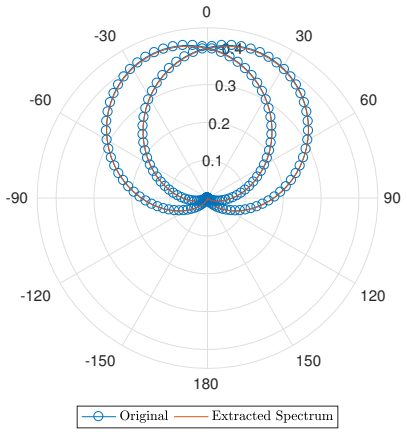

(a) $\bar{\theta} = 15°$

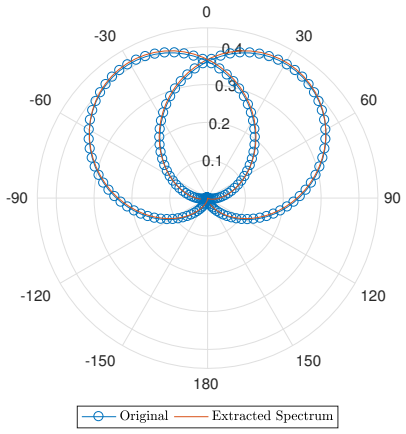

(b) $\bar{\theta} = 30°$

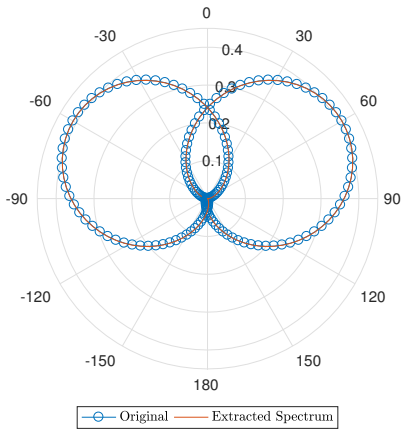

(c) $\bar{\theta} = 60°$

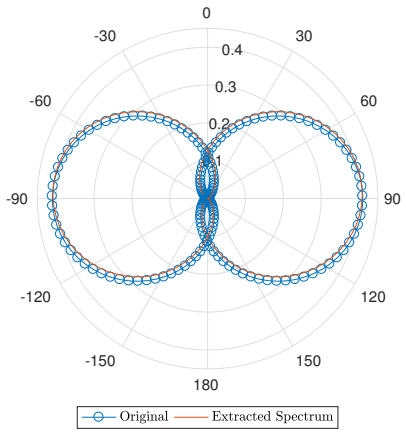

(d) $\bar{\theta} = 90°$

Figure 4.6: Comparison between the original and extracted ocean wave directional spread functions for different wind directions. Transmitter frequency $f_o = 13.385$ MHz, bistatic angle $\phi = 30°$, transmitter look direction $\theta_{01} = 60°$, spreading factor $s = 1.85$, and wind speed $U_{19.5} = 15$ m/s.

Table 4.3: Normalized root-mean-square error for the ocean wave spectrum extraction from the patch cross section under different wind directions

$\bar{\theta}$ (°)	$e_{\hat{S}}$	$e_{\bar{\theta}}$	e_s	$e_{\overline{H_{1/3}}}$
15.00°	0.61%	0.66%	1.32%	1.07%
30.00°	0.66%	2.95%	2.46%	0.58%
60.00°	0.99%	0.23%	0.24%	1.84%
90.00°	0.67%	3.95%	0.69%	1.17%

Table 4.4: Root-mean-square error for the ocean wave spectrum extraction under different wind directions

$\bar{\theta}$ (°)	$RMSE_{\hat{S}}$ (m^2/s)	$RMSE_{\bar{\theta}}$ (°)	$RMSE_s$	$RMSE_{\overline{H_{1/3}}}$ (m)
15.00°	3.34	9.96×10^{-2}	2.43×10^{-2}	3.64×10^{-2}
30.00°	3.60	8.85×10^{-1}	4.55×10^{-2}	1.98×10^{-2}
60.00°	5.39	1.39×10^{-1}	4.51×10^{-3}	6.24×10^{-2}
90.00°	3.67	3.56	1.28×10^{-2}	3.97×10^{-2}

4.2.2 Discussion

Comparing with the results obtained in Chapter 3, the inclusion of the first-order cross section resulted in an increase of the RMS error for changes in both wind speed and direction.

Regarding changes in the wind speed, the extraction at 6 m/s returned the highest relative RMS error for the non-directional spectrum. From its extracted non-directional spectrum in Figure 4.2, it is evident that the regularization parameter played a role in the increase of the error value, oversmoothing the spectrum. Also, as previously explained, at 6 m/s the wave field did not return enough energy to the receiver for a transmitted signal of 13.385 MHz, making this radar configuration unsuitable to map wave fields generated by these wind speeds [91]. In the following experiments, the 6 m/s will then be dropped, giving place to a wind speed within an appropriate range for a 13.385 MHz HF radar. The trend of decreasing normalized RMS error for higher wind speeds is confirmed, while for the directional parameters, this trend is not confirmed.

As for changes in the wind direction, the error for the non-directional spectrum was relatively stable, while no specific trend could be identified for the directional parameters. During the optimization, however, it was observed that the algorithm missed the optimal point for the directional parameters while trying to minimize the error for the non-directional spectrum. Further studies will be necessary to determine the cause of this problem.

As expected for the noiseless case, the regularization parameter converged to zero in all presented conditions.

4.3 Noise-contaminated Doppler Radar Data

According to the International Telecommunication Union [123, 124], there are three main sources of radio noise in the HF band: atmospheric noise due to lightning, cosmic noise, and man-made noise. Noise from these sources usually does not appear independently, and each of them has a characteristic spectral distribution. However, if a single cause is not dominant, radio noise can be characterized as white Gaussian noise [124].

Using the model proposed by Pierson [125] for a stationary Gaussian process, Gill [3] presented the radio noise voltage as

$$\begin{aligned} n_r(t) &= \int_{\omega'} \left[h\left(\omega' + \frac{B}{2}\right) - h\left(\omega' - \frac{B}{2}\right) \right] e^{j\omega' t} e^{j\epsilon(\omega')} \sqrt{S_N(\omega') \frac{d\omega'}{2\pi}} \\ &= \int_{-\frac{B}{2}}^{\frac{B}{2}} e^{j\omega' t} e^{j\epsilon(\omega')} \sqrt{S_N(\omega') \frac{d\omega'}{2\pi}}. \end{aligned} \tag{4.2}$$

The form suggested by Pierson [125] can be applied to any stationary Gaussian process. According to Barrick and Snider [32], even though the first-order cross section describes a stationary Gaussian process, the second-order is clearly not Gaussian, since it is the product of two Gaussian processes. For practical purposes, however, the second-order cross section can be approximated as a Gaussian process with fair accuracy [32], which allows the use of Pierson's form for the received radar signal.

The power spectral density of the received radar signal can be written as

$$S_\sigma(\omega) = \sqrt{C\sigma(\omega)}, \tag{4.3}$$

where C is the radar attenuation function, defined as

$$C = \frac{{\lambda_o}^2 P_T G_T G_R A p |\mathcal{F}(\rho_{01})\mathcal{F}(\rho_{20})|^2}{(4\pi)^3 {\rho_{01}}^2 {\rho_{20}}^2}, \tag{4.4}$$

where:

- G_T: Gain of the transmitter.
- G_R: Gain of the receiver, which can be defined as

$$G_R = 5.48\frac{(N+1)d_s}{\lambda_o}$$

  for an N-element linear array dipole array.

- P_T: Power of the transmitter.
- A_P: Area of the scattering patch, defined in Equation (2.33), where θ_{HPBW} is the half-power beamwidth of the receiver, given by

$$\theta_{HPBW} = 2.65\frac{\lambda_o}{(N+1)\pi d_s}$$

  for an N-element linear dipole array, with a distance d_s between elements.

- λ_o: wavelength of the transmitter signal.
- ρ_{01}: Distance between the transmitter and the first scatter.
- ρ_{02}: Distance between the second scatter and the receiver.
- $\mathcal{F}$: Transmission path attenuation function. For short distances the Sommerfeld attenuation function is sufficient. However, for the usual distances in HF radar, the equation proposed by Wait [21], and later revisited by Dawe [126], should be used, since it accounts for the Earth's curvature and impedance of the ocean surface.

Using Pierson's form, the time series of the received radar signal can be written as

$$E_r(t) = \sqrt{C} \int_{-\frac{B}{2}}^{\frac{B}{2}} e^{j\omega' t} e^{j\epsilon(\omega')} \sqrt{S_\sigma(\omega') \frac{d\omega'}{2\pi}} \tag{4.5}$$

In order to simulate the noise-contaminated received radar signal, additive white Gaussian noise should be applied to the radar received time series. Therefore, the resulting noise-contaminated received radar signal E_n would then be written as

$$E_n(t) = E_r(t) + n_r(t).$$

One way to quantify the noise in a signal is by its signal-to-noise ratio (SNR). The SNR in dB is defined as

$$\mathrm{SNR}_{\mathrm{dB}} = 10 \log_{10} \left(\frac{P_{E_r}}{P_{n_r}} \right),$$

where P_{E_r} is the power of the uncorrupted received signal and P_{n_r} is the power of the noise signal.

According to Howard [127] for example, the power spectral density of a band-limited process can be written as

$$S(\omega_d) = \frac{1}{T} \left| \int_0^T E(t) e^{j\omega_d t} dt \right|^2 \tag{4.6}$$

The noise-contaminated radar received power spectral density can then be calculated from (4.6). This signal will have a significantly smaller power than the cross section σ, since it is calculated from a time series based on Equation (4.3). This introduces some complexities to the problem, since the problem of inversion would be dependent on the particular choice of transmitter and receiver. Barrick [33] circumvents this problem

by normalizing the spectrum by its maximum first-order peak, which eliminates the dependency on a specific radar, also getting rid of other attenuation factors.

Once the normalized noise-contaminated power spectral density was obtained, the method described in the previous chapter is applied, where it is compared to a noiseless normalized cross section.

4.3.1 Extraction Results

In order to focus on the effects of the noise in the extraction results, this section, unlike the previous ones, will only present the relative RMS errors in graphical form. Results that are particularly relevant to the discussion will be presented as required.

4.3.1.1 Changes in Wind Speed

Figures 4.7 to 4.11 show, respectively, the normalized RMS errors for the non-directional ocean wave spectrum, mean wind direction, spreading parameter, significant wave height, and peak wave period for different wind speeds and signal-to-noise ratios.

4.3.1.2 Changes in Wind Direction

Figures 4.12 to 4.16 present, respectively, the normalized RMS errors for the non-directional ocean wave spectrum, mean wind direction, spreading parameter, significant wave height, and peak wave period for different mean wind directions and noise levels.

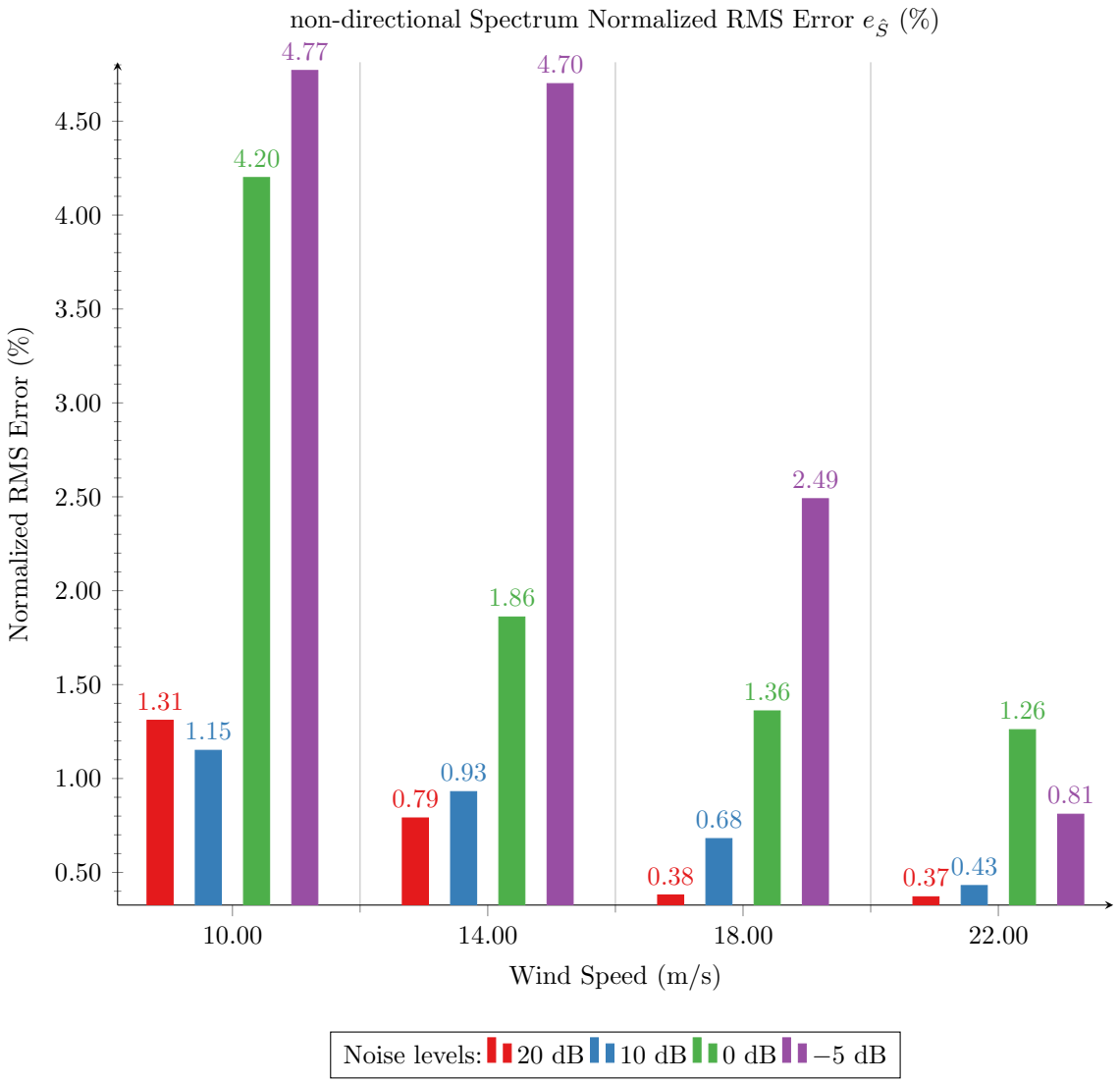

Figure 4.7: Normalized root-mean-square error for the extracted non-directional ocean wave spectrum under different wind speeds and signal-to-noise ratios. Transmitter frequency $f_o = 13.385$ MHz, bistatic angle $\phi = 30°$, transmitter look direction $\theta_{01} = 60°$, spreading factor $s = 1.85$, and wind direction $\theta_w = \bar{\theta} = 15°$.

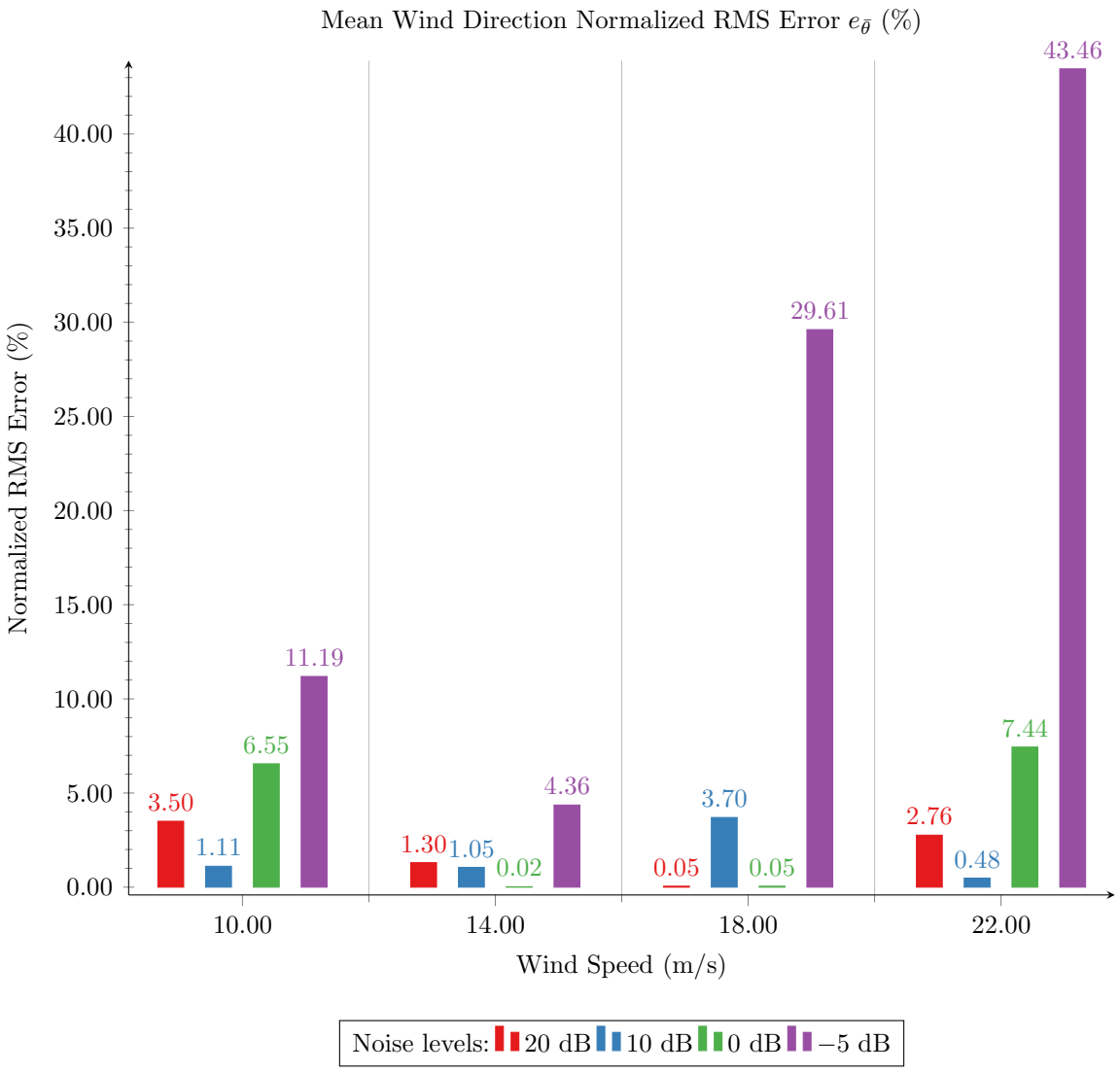

Figure 4.8: Normalized root-mean-square error for the extracted mean wind direction $\bar{\theta}$ under different wind speeds and signal-to-noise ratios. Transmitter frequency f_o = 13.385 MHz, bistatic angle $\phi = 30°$, transmitter look direction $\theta_{01} = 60°$, spreading factor $s = 1.85$, and wind direction $\theta_w = \bar{\theta} = 15°$.

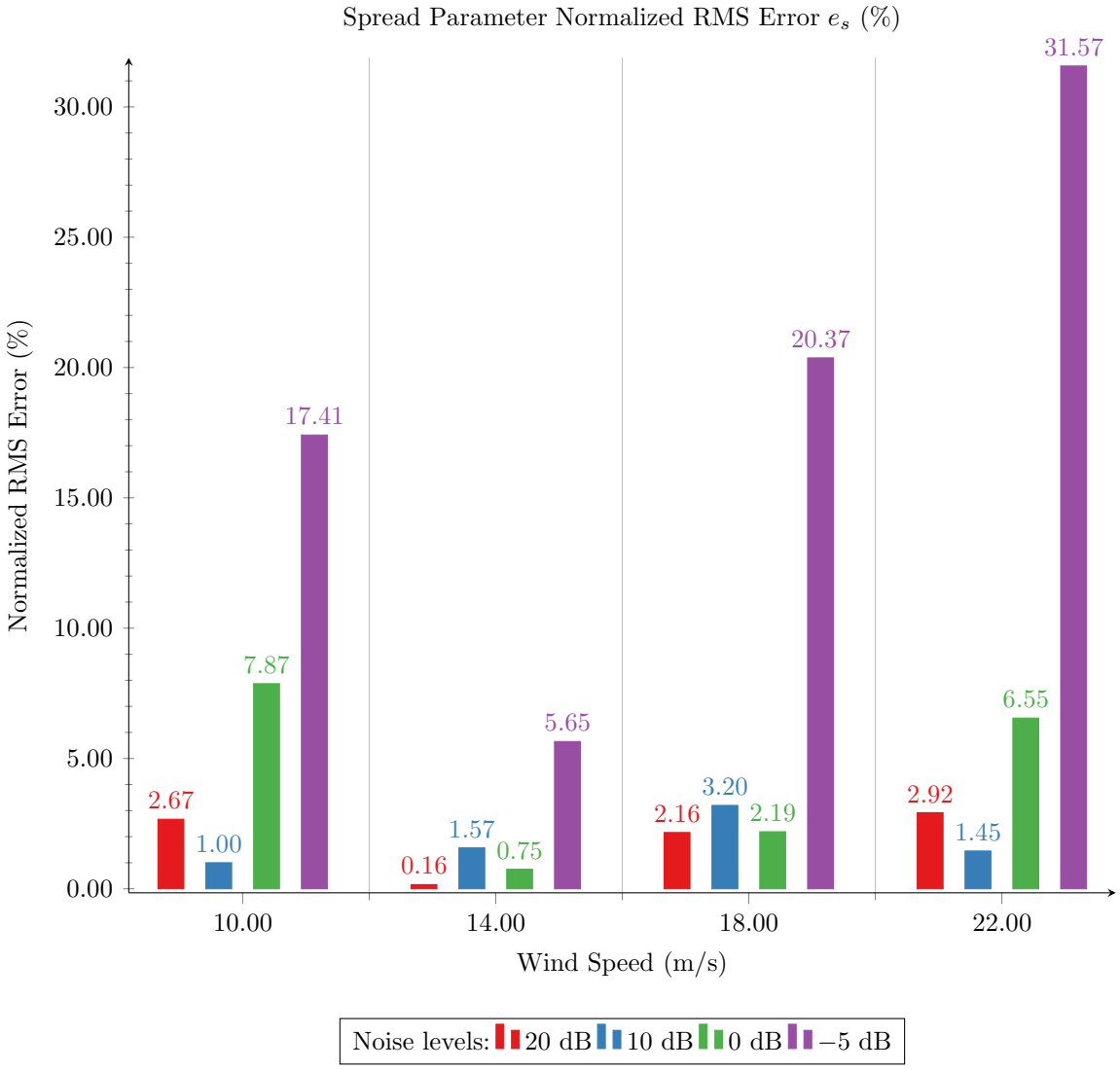

Figure 4.9: Normalized root-mean-square error for the extracted spread parameter under different wind speeds and signal-to-noise ratios. Transmitter frequency f_o = 13.385 MHz, bistatic angle $\phi = 30°$, transmitter look direction $\theta_{01} = 60°$, spreading factor $s = 1.85$, and wind direction $\theta_w = \bar{\theta} = 15°$.

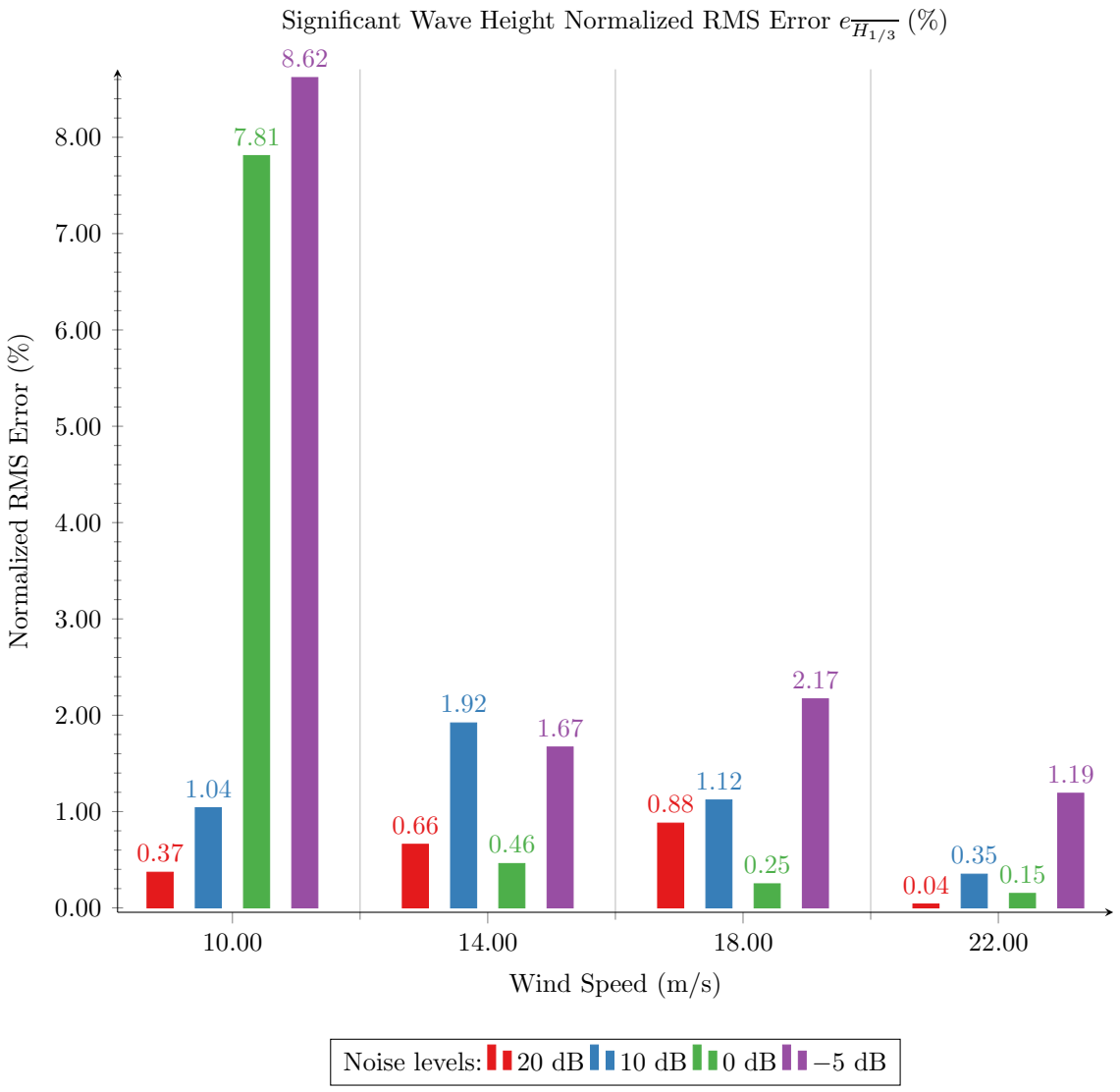

Figure 4.10: Normalized root-mean-square error for the calculated significant wave height $\overline{H_{1/3}}$ under different wind speeds and signal-to-noise ratios. Transmitter frequency $f_o = 13.385$ MHz, bistatic angle $\phi = 30°$, transmitter look direction $\theta_{01} = 60°$, spreading factor $s = 1.85$, and wind direction $\theta_w = \bar{\theta} = 15°$.

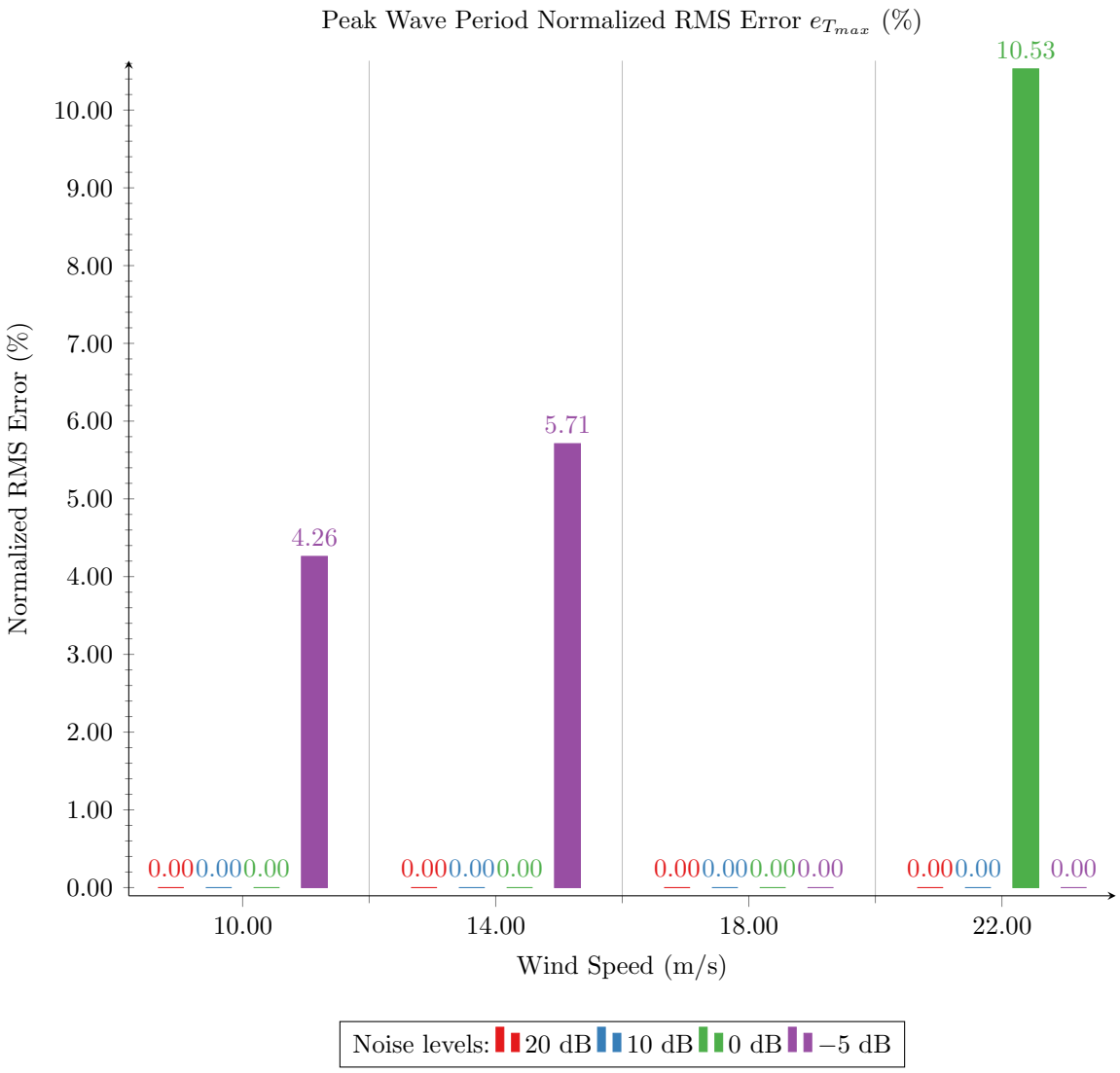

Figure 4.11: Normalized root-mean-square error for the peak wave period T_{max} under different wind speeds and signal-to-noise ratios. Transmitter frequency f_o = 13.385 MHz, bistatic angle $\phi = 30°$, transmitter look direction $\theta_{01} = 60°$, spreading factor $s = 1.85$, and wind direction $\theta_w = \bar{\theta} = 15°$.

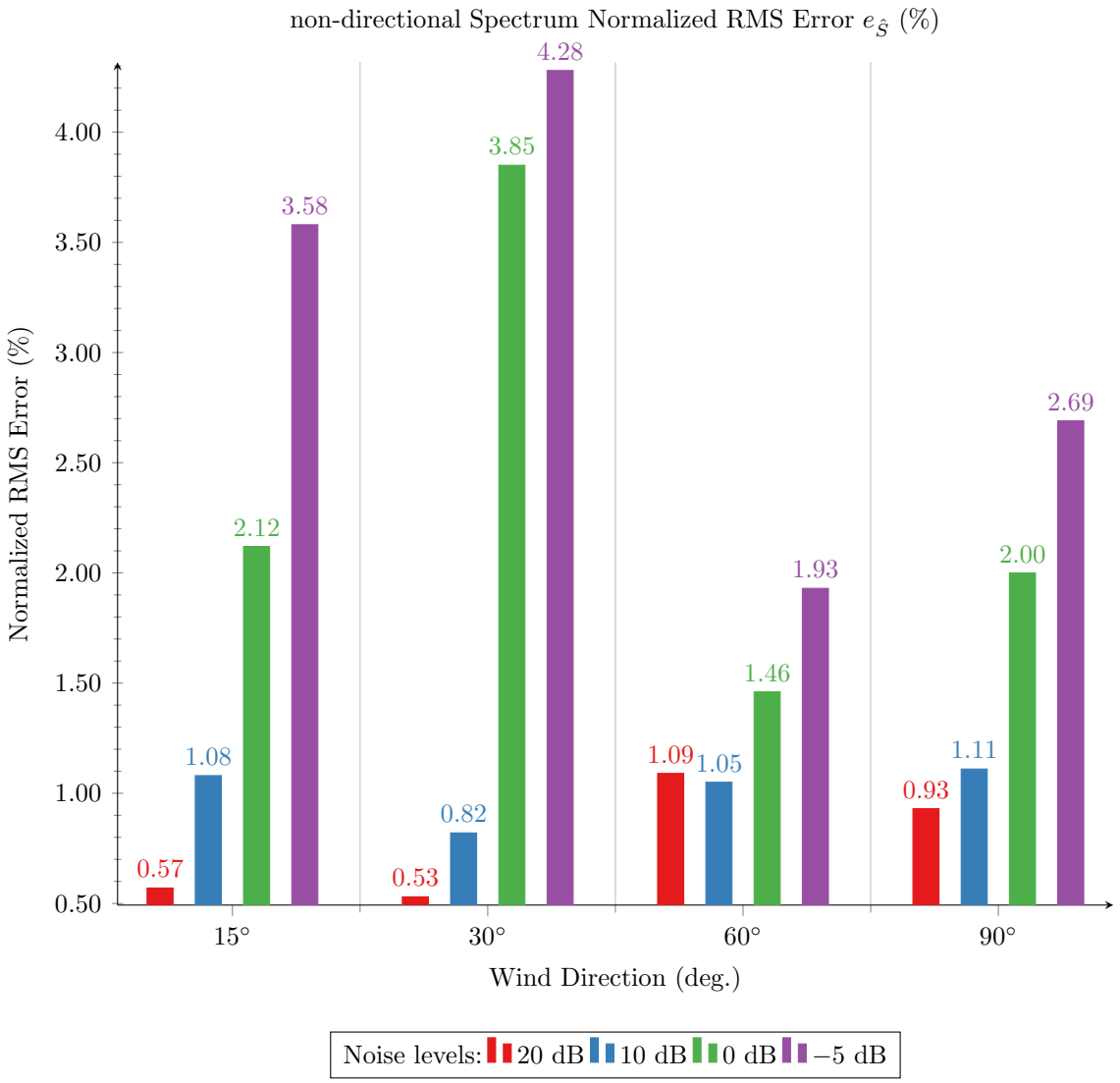

Figure 4.12: Normalized root-mean-square error for the extracted non-directional ocean wave spectrum under different wind directions and signal-to-noise ratios. Transmitter frequency $f_o = 13.385$ MHz, bistatic angle $\phi = 30°$, transmitter look direction $\theta_{01} = 60°$, spreading factor $s = 1.85$, and wind speed $U_{19.5} = 15$ m/s.

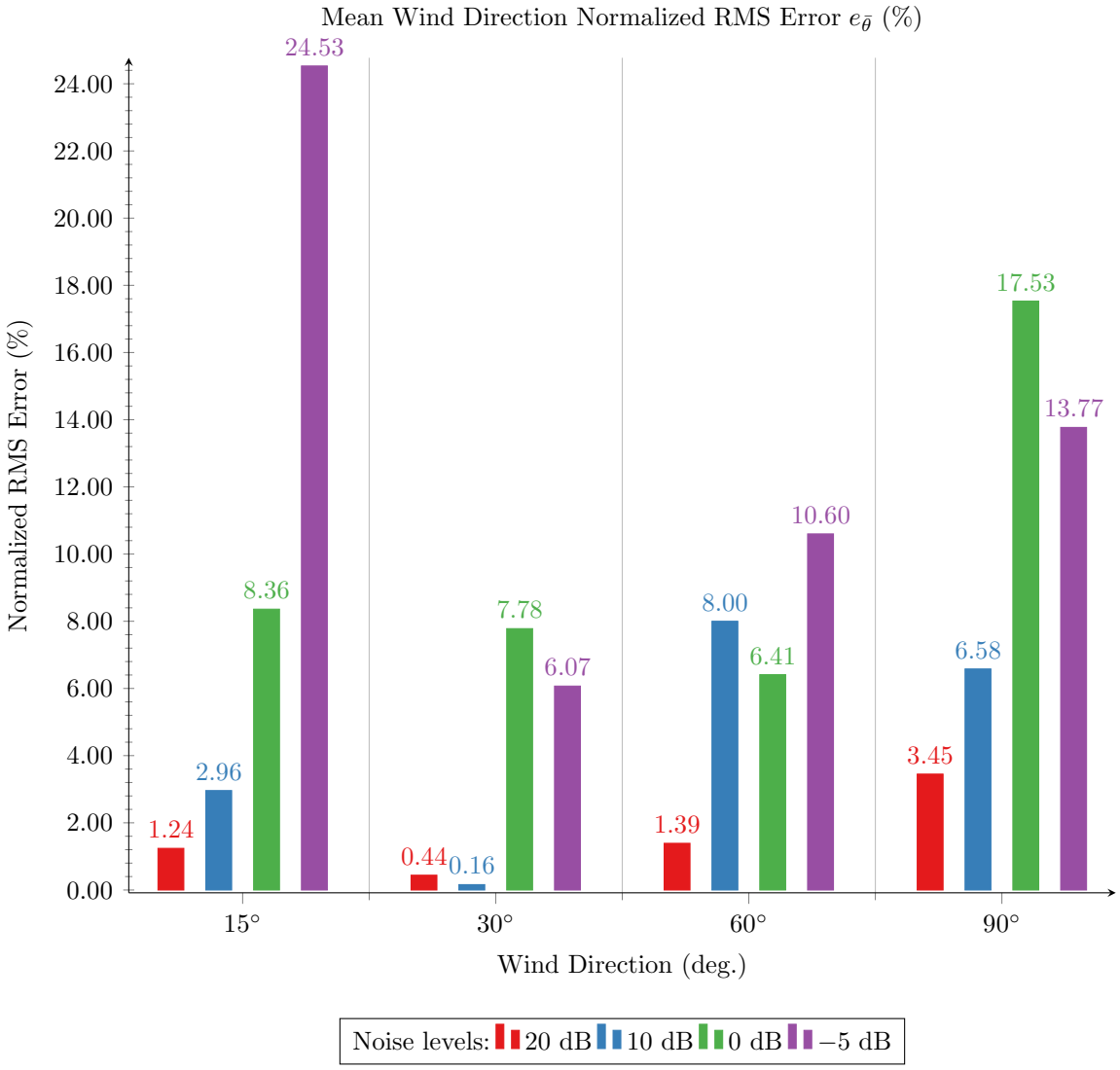

Figure 4.13: Normalized root-mean-square error for the extracted mean wind direction $\bar{\theta}$ under different wind directions and signal-to-noise ratios. Transmitter frequency $f_o = 13.385$ MHz, bistatic angle $\phi = 30°$, transmitter look direction $\theta_{01} = 60°$, spreading factor $s = 1.85$, and wind speed $U_{19.5} = 15$ m/s.

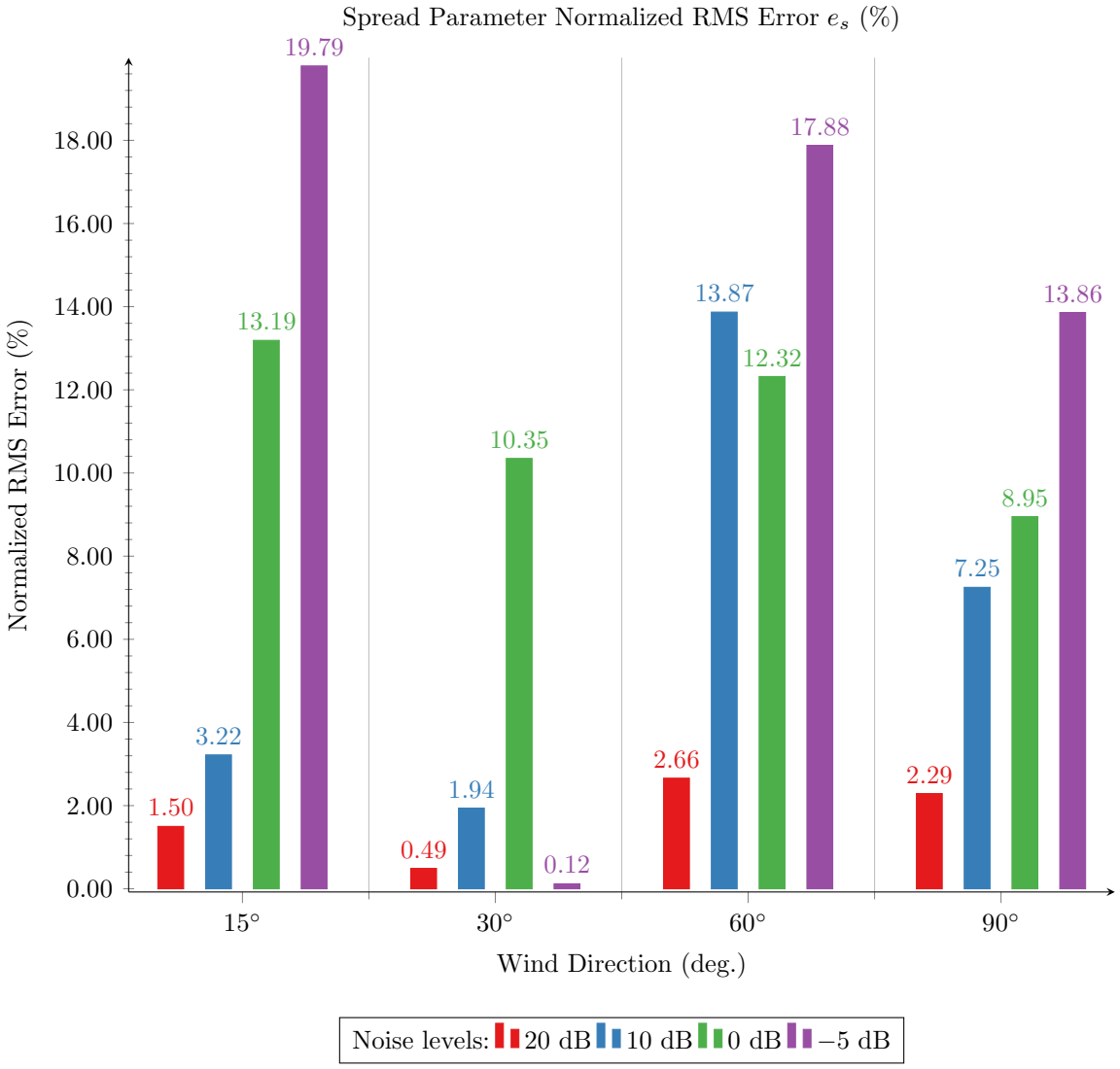

Figure 4.14: Normalized root-mean-square error for the extracted spread parameter under different wind directions and signal-to-noise ratios. Transmitter frequency f_o = 13.385 MHz, bistatic angle $\phi = 30°$, transmitter look direction $\theta_{01} = 60°$, spreading factor $s = 1.85$, and wind speed $U_{19.5} = 15$ m/s.

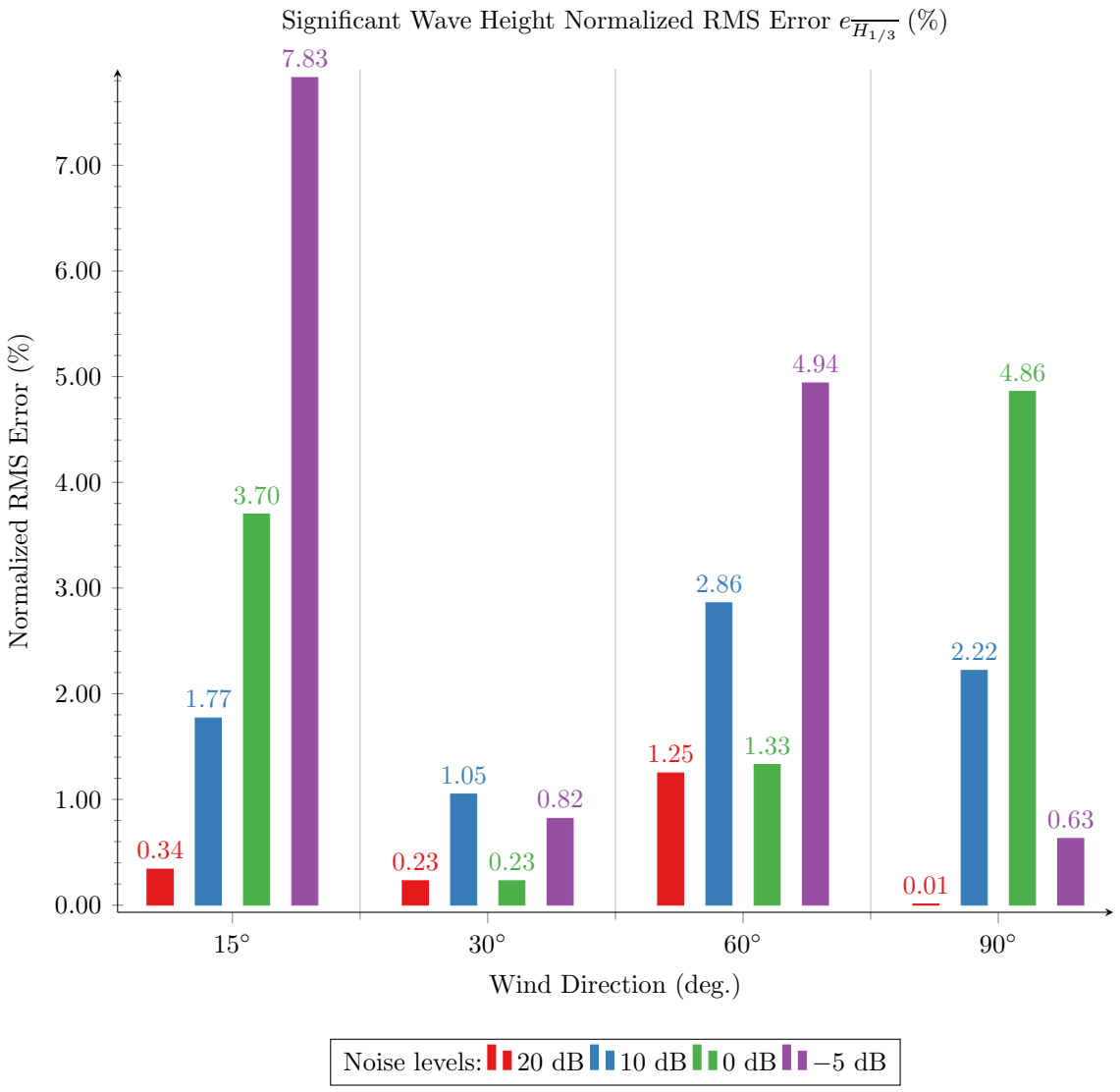

Figure 4.15: Normalized root-mean-square error for the calculated significant wave height $\overline{H_{1/3}}$ under different wind directions and signal-to-noise ratios. Transmitter frequency $f_o = 13.385$ MHz, bistatic angle $\phi = 30°$, transmitter look direction $\theta_{01} = 60°$, spreading factor $s = 1.85$, and wind speed $U_{19.5} = 15$ m/s.

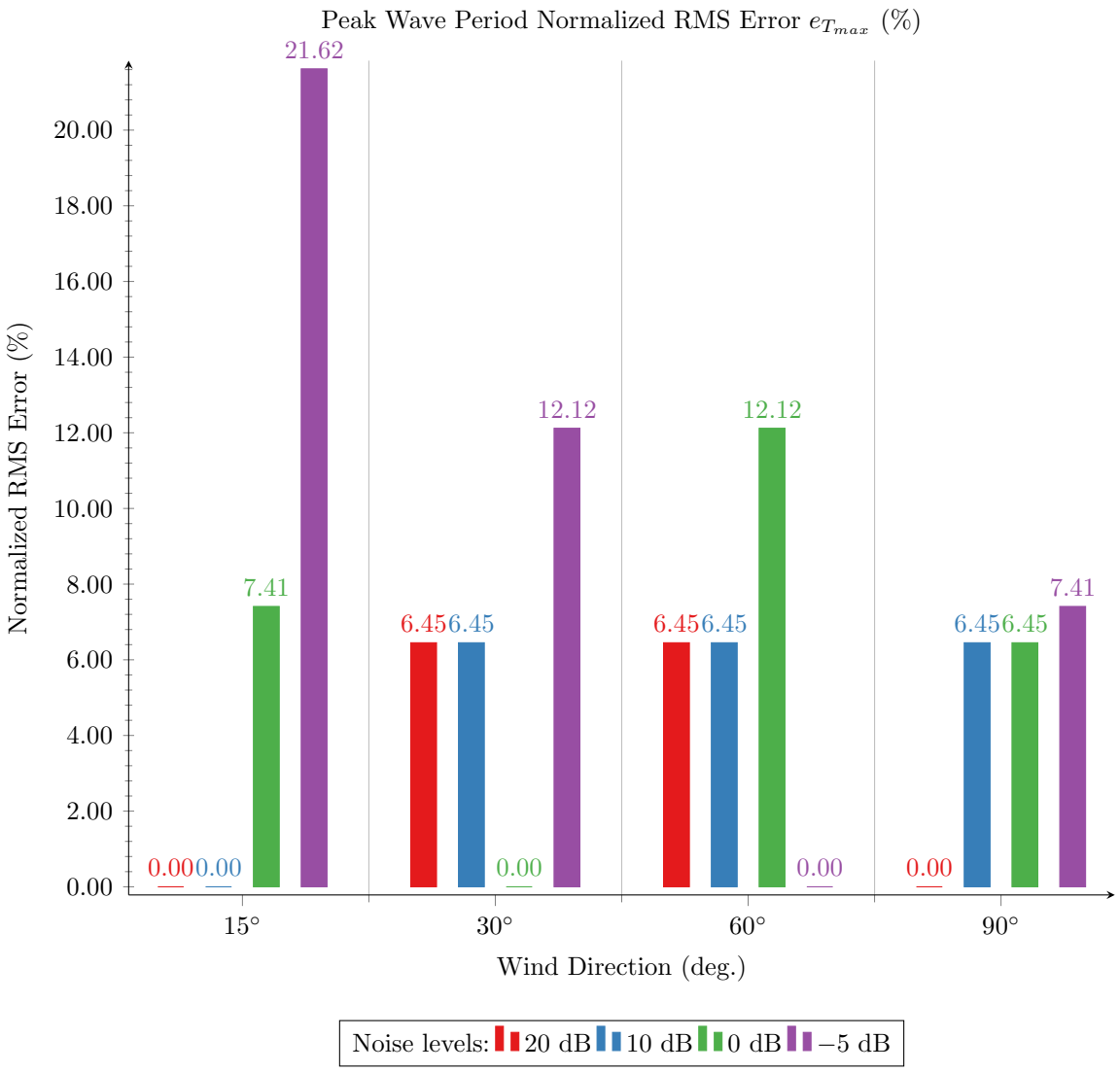

Figure 4.16: Normalized root-mean-square error for the calculated peak wave period T_{max} under different wind directions and signal-to-noise ratios. Transmitter frequency $f_o = 13.385$ MHz, bistatic angle $\phi = 30°$, transmitter look direction $\theta_{01} = 60°$, spreading factor $s = 1.85$, and wind speed $U_{19.5} = 15$ m/s.

4.3.2 Discussion

From the results, it is possible to conclude that the presented method was able to recover the directional ocean wave spectrum in a noisy environment. However, some considerations must be made.

The cases with lower wind speeds were more affected by an increase in noise levels, as seen in Figure 4.7. The comparison between noiseless and noisy Doppler spectra in these situations, as shown in Figure 4.17, might bring some insights to this problem.

As can be observed, the second-order features in all cases presented in Figure 4.17 have been contaminated by noise to such a degree that part of the information from the non-directional ocean wave spectrum was lost. Therefore, a greater relative error was observed in these cases. It should be added, however, that even though these error values were higher if compared to the highest wind speeds, these errors were still small considering the noise levels that were present in these cases.

For the mean wind direction, on the other hand, there was a higher error in the 18 m/s and 22 m/s cases, especially in the SNR= -5 dB case. While further studies will be dedicated to the origin of these errors, earlier results indicate that the `lsqnonlin` function continued trying to fit after the closest point to convergence was reached. As for the spreading factor, the behaviour of its normalized error was consistent with the one observed for the mean wind direction.

As expected, the relative error of the significant wave height followed the trend set by the nondirecitonal spectrum. The significant wave height was fairly robust to noise.

While in previous cases the peak wave period was precisely determined, this was

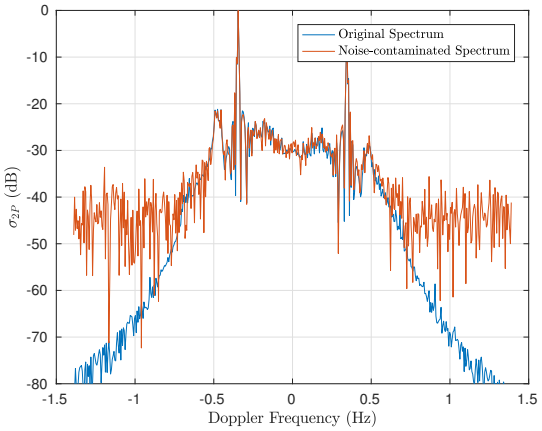

(a) $U_{19.5} = 10$ m/s, SNR= 0 dB

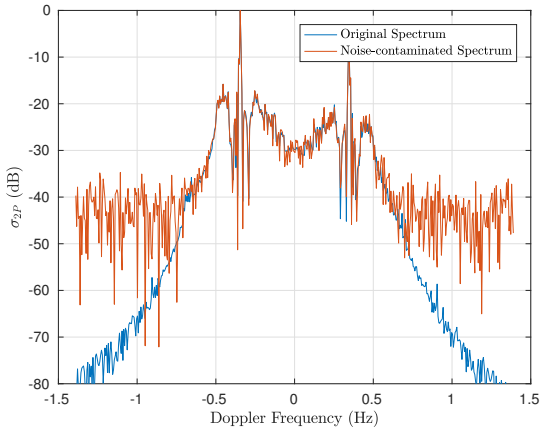

(b) $U_{19.5} = 14$ m/s, SNR= 0 dB

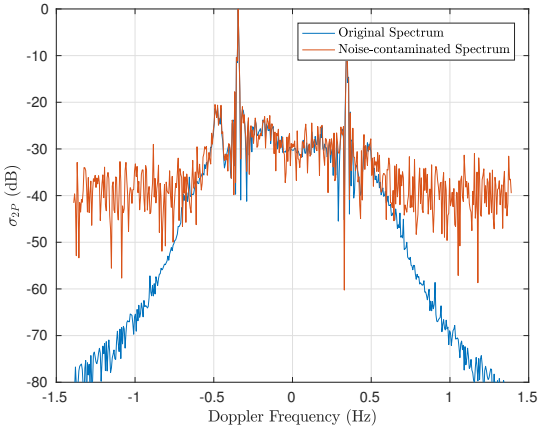

(c) $U_{19.5} = 10$ m/s, SNR= -5 dB

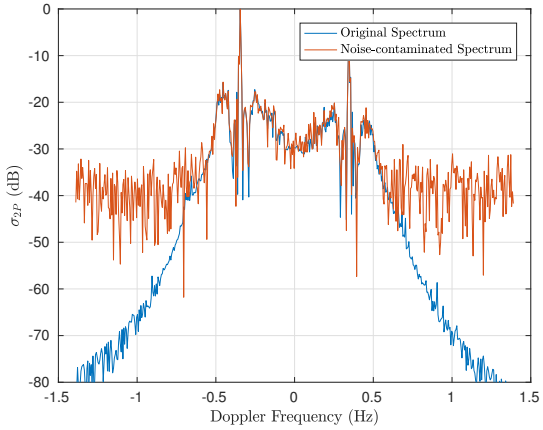

(d) $U_{19.5} = 14$ m/s, SNR= -5 dB

Figure 4.17: Comparison between noiseless and noisy synthetic patch scattering bistatic cross section under different wind speeds and signal-to-noise ratios. Transmitter frequency $f_o = 13.385$ MHz, bistatic angle $\phi = 30°$, transmitter look direction $\theta_{01} = 60°$, spreading factor $s = 1.85$, and wind direction $\theta_w = \bar{\theta} = 15°$

not the case in the presence of noise. From Figure 4.11 it can be observed that in most cases, the peak wave period was precisely determined. However, in three cases — $U_{19.5} = 10$ m/s with SNR $= -5$ dB, $U_{19.5} = 14$ m/s with SNR $= -5$ dB, and $U_{19.5} = 22$ m/s with SNR $= 0$ dB — T_{max} presented errors. Since T_{max} was

directly dependent on the wave number, these error values were dependent on the discretization of the non-directional spectrum. The resolution of the nondirectional spectrum in the Y_1 domain used throughout the thesis is 0.01172 $(\text{rad/m})^{-2}$, with the spectrum spanning from 0.0059 $(\text{rad/m})^{-2}$ to 2.9951 $(\text{rad/m})^{-2}$.

With respect to changes in the mean wind direction, the extraction of the non-directional spectra was reasonably accurate, with error values below 4.5% in all cases. The directional parameters, on the other hand, were more sensitive to noise, with error values being as high as 25% for the mean wind direction and 20% for the spread parameter, for the $\bar{\theta} = 15^{\circ}$ and SNR$= -5$ dB case. As in the previous cases, the directional parameters followed the same error trend, while the significant wave height followed the non-directional wave spectrum error trend.

As for the peak wave period, it can be observed that T_{max} was more sensitive to changes in the mean wave direction than to changes in the wind speed. An interesting feature observed in Figure 4.16 was that some values were frequently obtained in the error graph. This was due to the fact that, being dependent on the discretization of the ocean wave spectrum, the error of the peak wave period is a discrete quantity.

The regularization parameter for each case has converged to a nonzero value, since it needs to account for the discrepancy added by the noise. This confirms the action of Tikhonov regularization on the final result.

4.4 General Chapter Summary

In this chapter, the extraction method presented in Chapter 3 was applied to a more realistic scenario. In the first part of the chapter, the concept of the patch scattering

cross section was introduced, in which the scatterings were considered up to the second-order. The extraction results were satisfactory, with a slight variation from the case presented in the previous chapter.

In the second part of the chapter, the process of noise contamination of the ocean wave spectrum was presented. Since the addition of noise occurred in the time domain, Pierson's model for the time series of a stationary Gaussian process was applied, taking into account the remarks from Barrick and Snider [32], which consider the second-order scattering of the ocean surface a Gaussian process for practical purposes. The noise model was chosen according to recommendations of the International Telecommunication Union [123, 124], which indicates the use of additive white Gaussian noise when there was no dominant cause for the noise. Then, the extraction method was applied to the noise-contaminated Doppler spectrum, under different noise levels, where the wind speed and direction were changed independently. It was observed that the extraction of the directional parameters and peak wave period were more susceptible to variations in the mean wind direction, while the non-directional ocean wave spectrum presented consistent results in the same situation. As for changes in the wind speed, the directional parameters showed high error values at the highest noise levels and wind speeds.

Chapter 5

Conclusions

5.1 General Summary

The present work introduced a new approach to the extraction of the directional ocean wave spectrum from bistatic HF radar data. The method, based on the approach presented by Shahidi and Gill [1], consists of the use of a change of variables to simplify the second-order cross section per unit area of the ocean surface to a nonlinear Fredholm integral equation of the first kind, and then applying Tikhonov regularization in Hilbert scales to the inverse problem in question.

Chapter 1 introduced the subject by describing the importance of this research, being the first method known to the author to deal with the nonlinear extraction of the directional ocean wave spectrum from bistatic HF radar data. A literature review was then presented, where previous works in radio oceanography, especially in the HF band, were described, giving a historical perspective on the topic. Then, the scope of the thesis was presented.

Chapter 2 presented the theoretical background of the physical phenomena related to the mapping of the ocean surface using HF radar. In its first section, a brief review of the classification, generation and spectral representation of ocean waves was given. This section was important for understanding the object of study in radio oceanography, as well as for introducing concepts such as the ocean wave spectrum, wave vectors and meteorological measurements of the ocean surface, and spectral effects of wave-wave interaction. Also, the spectral and directional spreading function models used throughout this thesis were presented in this section. The following section presented the fundamentals regarding the bistatic radar cross section, in which the bistatic geometry, scattering mechanisms and the formulations of the first- and second-order cross sections were given.

Once the fundamentals of the theory and the historical perspective of the topic were presented, the new extraction method was described in Chapter 3. In the first section, some fundamental concepts to the presented method were introduced, such as the idea of Hilbert spaces, posedness of a problem, and regularized nonlinear least-square. Then, in the same section, Tikhonov regularization in Hilbert scales was presented, as well as a choice of the regularization parameter. Then, the simplification of the second-order cross section was presented, as well as the geometrical properties and spectral scaling and translation that arise after the simplification. These properties are important in designing the problem in question. Finally, the method was applied to synthetic second-order HF radar data, retrieving the directional ocean wave spectrum with a reasonable level of accuracy, with a maximum error of 0.28% for the spectrum estimation, 0.89% for the mean wave energy direction, 0.67% for the spreading factor, and 1.65% for the significant wave height. In all cases of this

chapter, the peak position of the non-directional spectra were exactly obtained.

The results presented in Chapter 3, even though encouraging, only served the purpose of confirming the theoretical soundness of the proposed method. A more realistic situation was addressed in Chapter 4, where the first-order cross section and noise were introduced into the problem. First, the patch scattering cross section, which contains the cross sections related to the scattering processes that occurred within the scattering patch, was presented. In this work, the patch scattering cross section was considered up to second-order. Then, the extraction method was applied to synthetic patch scattering cross-sections for different wind speeds and directions, where it generated good results for all ocean conditions to which the radar configuration in question was suited. In the second part of Chapter 4, the fundamentals of radio noise addition were presented, describing the mathematical process of noise contamination of the radar Doppler data. The extraction method was then applied to the noise-contaminated bistatic HF radar data, returning good results for most noise and ocean conditions. The extraction of the non-directional ocean wave spectrum was consistent, while the directional parameters were susceptible to high levels of noise.

Overall, the method was proven effective for the extraction of the directional ocean wave spectrum from bistatic HF radar data even in noise-contaminated environments. These results are important, since, to the author's knowledge, this is the first nonlinear extraction method applied to bistatic HF radar data.

5.2 Suggestions for Future Work

Future work may focus on the analysis of the noise sensitivity of the directional parameters, as well as generalizing the method for an unknown form of the directional spreading function, in which no function model is assumed.

Regarding the extraction method, other techniques can be applied to solve the nonlinear inversion problem. The works of Chavent [104] and Wazwaz [102] contain alternatives to Tikhonov regularization in Hilbert scales. Also, other choices of regularization parameter can be considered, such that the variations in the regularizing factor are also considered. The book by Kaltenbacher *et al.* [118] presents some iterative regularization methods that can be applied to the extraction problem.

Furthermore, the method should be tested with real bistatic HF radar data in order to confirm its efficacy.

References

[1] R. Shahidi and E. W. Gill, "A new method for ocean spectrum extraction from high-frequency second-order doppler radar data," in *MTS/IEEE Oceans'16 Monterey*, 2016.

[2] W. Munk, "Origin and generation of waves," *Coastal Engineering Proceedings*, vol. 1, no. 1, p. 1, 1950.

[3] E. W. Gill, "The scattering of high frequency electromagnetic radiation from the ocean surface : an analysis based on a bistatic ground wave radar configuration," Ph.D. dissertation, Memorial University of Newfoundland. Faculty of Engineering and Applied Science, St. John's, Newfoundland and Labrador, Canada, 1999.

[4] S. A. Kitaigorodskii, "Applications of the theory of similarity to the analysis of wind-generated wave motion as a stochastic process," *Izv. Geophys. Ser. Acad. Sci., USSR*, vol. 1, pp. 105–117, 1962.

[5] E. W. Gill, "An algorithm for the extraction of ocean wave parameters from wide beam HF radar (CODAR) backscatter," Master's thesis, Memorial Univer-

sity of Newfoundland. Faculty of Engineering and Applied Science, St. John's, Newfoundland and Labrador, Canada, 1990.

[6] M. Skolnik, *Radar Handbook, Third Edition.* McGraw-Hill Education, 2008.

[7] N. Willis, *Bistatic Radar*, ser. Electromagnetics and Radar. Institution of Engineering and Technology, 2005.

[8] E. L. Feinberg, "On the propagation of radio waves along an imperfect surface," *J. Phys.(Moscow)*, vol. 8, no. 6, pp. 317–330, 1944.

[9] L. V. Blake, "Reflection of radio waves from a rough sea," *Proceedings of the IRE*, vol. 38, no. 3, pp. 301–304, 1950.

[10] S. O. Rice, "Reflection of electromagnetic waves from slightly rough surfaces," *Communications on pure and applied mathematics*, vol. 4, no. 2-3, pp. 351–378, 1951.

[11] B. Kinsman, *Wind waves: their generation and propagation on the ocean surface.* Courier Corporation, 1965.

[12] S. R. Massel, *Ocean surface waves: their physics and prediction.* World scientific, 2013, vol. 36.

[13] W. J. Pierson, *A unified mathematical theory for the analysis, propagation, and refraction of storm generated ocean surface waves.* New York University, College of Engineering, Department of Meteorology, 1952, vol. I and II.

[14] G. Neumann, *On wind generated ocean waves with special reference to the problem of wave forecasting.* New York University, College of Engineering, Dept. of Meteorology, 1952.

[15] C. Eckart, "The scattering of sound from the sea surface," *The Journal of the Acoustical Society of America*, vol. 25, no. 3, pp. 566–570, 1953.

[16] C. Cox and W. Munk, "Measurement of the roughness of the sea surface from photographs of the sun's glitter," *J. Opt. Soc. Am.*, vol. 44, no. 11, pp. 838–850, Nov 1954.

[17] L. J. Cote, J. O. Davis, W. Marks, R. J. McGough, E. Mehr, W. Pierson, J. Ropek, G. Stephenson, and R. C. Vetter, "The directional spectrum of a wind generated sea as determined from data obtained by the Stereo Wave Observation Project," New York University, College of Engineering, Research Division, Tech. Rep. NONR 285(03), 1960.

[18] L. Moskowitz, W. J. Pierson, and E. Mehr, "Wave spectra estimated from wave records obtained by the OWS Weather Explorer and the OWS Weather Reporter (II)," New York University Bronx School of Engineering and Science, Tech. Rep. AD0405616, 1963.

[19] W. J. Pierson and L. Moskowitz, "A proposed spectral form for fully developed wind seas based on the similarity theory of S.A. Kitaigorodskii," DTIC Document, Tech. Rep., 1963.

[20] D. D. Crombie, "Doppler spectrum of sea echo at 13.56 mc./s." *Nature*, 1955.

[21] J. R. Wait, "Theory of HF ground wave backscatter from sea waves," *Journal of Geophysical Research*, vol. 71, no. 20, pp. 4839–4842, 1966.

[22] D. E. Barrick and W. H. Peake, "Scattering from surfaces with different roughness scales: Analysis and interpretation," National Aeronautics and Space Administration, Tech. Rep. AD0662751, 1967.

[23] ——, "A review of scattering from surfaces with different roughness scales," *Radio Science*, vol. 3, no. 8, pp. 865–868, August 1968.

[24] D. E. Barrick, "Radar signal spectrum distortions produced by volume and surface distributed scatterers," Battelle Memorial Institute, Columbus Labs, Columbus, OH, USA, Tech. Rep. AD0673560, 1968.

[25] ——, "Theory of ground-wave propagation across a rough sea at dekameter wavelengths," Battelle Memorial Institute, Columbus Labs, Tech. Rep. AD865840, 1970.

[26] ——, "Theory of HF and VHF propagation across the rough sea, 1, the effective surface impedance for a slightly rough highly conducting medium at grazing incidence," *Radio Science*, vol. 6, no. 5, pp. 517–526, 1971.

[27] ——, "Theory of HF and VHF propagation across the rough sea, 2, application to HF and VHF propagation above the sea," *Radio Science*, vol. 6, no. 5, pp. 527–533, 1971.

[28] W. H. Munk and W. A. Nierenberg, "High frequency radar sea return and the phillips saturation constant," *Nature*, vol. 224, no. 5226, p. 1285, Dec 1969.

[29] K. Hasselmann, "Determination of ocean wave spectra from doppler radio return from the sea surface," *Nature*, vol. 229, no. 1, pp. 16–17, 1971.

[30] D. E. Barrick, "First-order theory and analysis of MF/HF/VHF scatter from the sea," *IEEE Transactions on Antennas and Propagation*, vol. 20, no. 1, pp. 2–10, Jan 1972.

[31] ——, *Remote Sensing of Sea Sate by Radar*, ser. Remote Sensing of the Troposphere. Boulder, Colorado, USA: National Oceanic and Atmospheric Administration, 1972, ch. 12.

[32] D. Barrick and J. Snider, "The statistics of HF sea-echo doppler spectra," *IEEE Transactions on Antennas and Propagation*, vol. 25, no. 1, pp. 19–28, Jan 1977.

[33] D. E. Barrick, "Extraction of wave parameters from measured HF radar sea-echo Doppler spectra," *Radio Science*, vol. 12, no. 3, pp. 415–424, 1977.

[34] ——, "The ocean waveheight nondirectional spectrum from inversion of the HF sea-echo doppler spectrum," *Remote Sensing of Environment*, vol. 6, no. 3, pp. 201–227, 1977.

[35] B. Lipa, "Derivation of directional oceanwave spectra by integral inversion of secondorder radar echoes," *Radio Science*, vol. 12, no. 3, pp. 425–434, 6 1977.

[36] ——, "Inversion of second-order radar echoes from the sea," *Journal of Geophysical Research: Oceans*, vol. 83, no. C2, pp. 959–962, 1978.

[37] B. Lipa and D. Barrick, "Ocean swell parameters from narrow-beam HF radar

sea echo," in *AGARD Spec. Topics in HF Propagation on 12 p (SEE N80-19372 10-32)*, 1979.

[38] D. E. Barrick and B. J. Lipa, *Ocean Surface Features Observed by HF Coastal Ground-Wave Radars: A Progress Review.* Boston, MA: Springer US, 1979, pp. 129–152.

[39] ——, *A Compact Transportable HF Radar System for Directional Coastal Wave Field Measurements.* Boston, MA: Springer US, 1979, pp. 153–201.

[40] S. K. Srivastava, "Scattering of high-frequency electromagnetic waves from an ocean surface : an alternative approach incorporating a dipole source," Ph.D. dissertation, Memorial University of Newfoundland. Faculty of Engineering and Applied Science, St. John's, Newfoundland and Labrador, Canada, 1984.

[41] J. Walsh, "On the theory of electromagnetic propagation across a rough surface and calculations in the VHF region," Ocean Engineering Information Centre, Memorial University of Newfoundland, St. John's, Newfoundland, Canada, Tech. Rep. OEIC Report N00232, 1980.

[42] L. Wyatt, J. Venn, G. Burrows, A. Ponsford, M. Moorhead, and J. Van Heteren, "HF radar measurements of ocean wave parameters during NURWEC," *IEEE Journal of oceanic Engineering*, vol. 11, no. 2, pp. 219–234, 1986.

[43] L. Wyatt, "The measurement of the ocean wave directional spectrum from HF radar doppler spectra," *Radio science*, vol. 21, no. 3, pp. 473–485, 1986.

[44] B. J. Lipa and D. E. Barrick, "Analysis methods for narrow-beam high-

frequency radar sea echo," US Department of Commerce, National Oceanic and Atmospheric Administration, Environmental Research Laboratories, Tech. Rep., 1982.

[45] M. I. Chahine, "A general relaxation method for inverse solution of the full radiative transfer equation," *Journal of the Atmospheric Sciences*, vol. 29, no. 4, pp. 741–747, 1972.

[46] S. Twomey, B. Herman, and R. Rabinoff, "An extension to the chahine method of inverting the radiative transfer equation," *Journal of the Atmospheric Sciences*, vol. 34, no. 7, pp. 1085–1090, 1977.

[47] R. Howell, "An algorithm for the extraction of ocean wave spectra from narrow beam HF radar backscatter," Master's thesis, Memorial University of Newfoundland. Faculty of Engineering and Applied Science, St. John's, Newfoundland and Labrador, Canada, 1990.

[48] R. Howell and J. Walsh, "Measurement of ocean wave spectra using narrow-beam HF radar," *IEEE Journal of Oceanic Engineering*, vol. 18, no. 3, pp. 296–305, Jul 1993.

[49] J. Walsh, R. Howell, and B. Dawe, "Model development for evaluation studies of ground wave radar," Department of National Defence, Government of Canada, Memorial University of Newfoundland, St. John's, NL, Canada, Tech. Rep. DSS contract W7714-8-5655/01-ss, 1990.

[50] Y. Hisaki, "Nonlinear inversion of the integral equation to estimate ocean wave spectra from HF radar," *Radio science*, vol. 31, no. 1, pp. 25–39, 1996.

[51] ——, "Ocean wave directional spectra estimation from an HF ocean radar with a single antenna array: Observation," *Journal of Geophysical Research: Oceans*, vol. 110, no. C11, 2005, c11004.

[52] ——, "Ocean Wave Directional Spectra Estimation from an HF Ocean Radar with a Single Antenna Array: Methodology," *Journal of Atmospheric and Oceanic Technology*, vol. 23, no. 2, pp. 268–286, 2006.

[53] ——, "Quality Control of Surface Wave Data Estimated from Low Signal-to-Noise Ratio HF Radar Doppler Spectra," *Journal of Atmospheric and Oceanic Technology*, vol. 26, no. 11, pp. 2444–2461, 2009.

[54] ——, "Inter-comparison of wave data obtained from single high-frequency radar, in situ observation, and model prediction," *International Journal of Remote Sensing*, vol. 35, no. 10, pp. 3459–3481, 2014.

[55] ——, "Development of HF radar inversion algorithm for spectrum estimation (HIAS)," *Journal of Geophysical Research: Oceans*, vol. 120, no. 3, pp. 1725–1740, 2015.

[56] ——, "Ocean wave parameters and spectrum estimated from single and dual high-frequency radar systems," *Ocean Dynamics*, vol. 66, no. 9, pp. 1065–1085, 2016.

[57] R. Shahidi and E. W. Gill, personal communication.

[58] ——, "An efficient and exact solution for the extraction of nondirectional ocean

wave spectra from second-order high-frequency doppler spectra," in *MTS/IEEE Oceans'17 Aberdeen*, 2017.

[59] V. Pidgeon, "Bistatic cross section of the sea," *IEEE Transactions on Antennas and Propagation*, vol. 14, no. 3, pp. 405–406, 1966.

[60] V. W. Pidgeon, "Doppler dependence of radar sea return," *Journal of Geophysical Research*, vol. 73, no. 4, pp. 1333–1341, 1968.

[61] C. C. Teague, J. F. Vesecky, and D. M. Fernandez, "HF radar instruments, past to present," *OCEANOGRAPHY-WASHINGTON DC-OCEANOGRAPHY SOCIETY-*, vol. 10, pp. 40–44, 1997.

[62] A. M. Peterson, C. C. Teague, and G. L. Tyler, "Bistatic-radar observation of long-period, directional ocean-wave spectra with loran a," *Science*, vol. 170, no. 3954, pp. 158–161, 1970.

[63] C. C. Teague, "High-frequency resonant scattering techniques for the observation of directional ocean-wave spectra." Ph.D. dissertation, Dept. of Electrical Engineering, Stanford University, 1971.

[64] D. E. Barrick, "The interaction of HF/VHF radio waves with the sea surface and its implications," in *AGARD Conference proceedings No. 77 on Electromagnetics of the Sea*, A. G. for Aerospace Research & Development (AGARD), Ed., no. AGARD-CP-77-70. National Atlantic Threaty Organization (NATO), 1970, pp. 18–1 – 18–25.

[65] W. A. Nierenberg and W. H. Munk, "Sea spectra and radar scattering," Institute for Defense Analyses, Arlington, VA, USA, Tech. Rep. AD0760693, 1969.

[66] E. W. Gill and J. Walsh, "Bistatic form of the electric field equations for the scattering of vertically polarized high-frequency ground wave radiation from slightly rough, good conducting surfaces," *Radio science*, vol. 35, no. 6, pp. 1323–1335, 2000.

[67] J. Walsh and E. W. Gill, "An analysis of the scattering of high-frequency electromagnetic radiation from rough surfaces with application to pulse radar operating in backscatter mode," *Radio Science*, vol. 35, no. 6, pp. 1337–1359, 2000.

[68] J. Zhang and E. W. Gill, "Extraction of ocean wave spectra from simulated noisy bistatic high-frequency radar data," *IEEE Journal of Oceanic Engineering*, vol. 31, no. 4, pp. 779–796, 2006.

[69] E. W. Gill and J. Walsh, "High-frequency bistatic cross sections of the ocean surface," *Radio Science*, vol. 36, no. 6, pp. 1459–1475, 2001.

[70] O. Phillips, *The Dynamics of the Upper Ocean*, 2nd ed., ser. Cambridge Monographs on Mechanics and Applied Mathematics. Cambridge University Press, 1977.

[71] H. Lamb, *Hydrodynamics*, 4th ed. Cambridge University Press, 1916.

[72] B. Cushman-Roisin and J.-M. Beckers, *Introduction to Geophysical Fluid Dy-*

namics: Physical and Numerical Aspects (International Geophysics). Academic Press, 2011.

[73] O. M. Phillips, "On the generation of waves by turbulent wind," *Journal of Fluid Mechanics*, vol. 2, no. 05, pp. 417–445, 1957.

[74] J. W. Miles, "On the generation of surface waves by shear flows," *Journal of Fluid Mechanics*, vol. 3, no. 02, pp. 185–204, 1957.

[75] J. A. Elliott, "Microscale pressure fluctuations near waves being generated by the wind," *Journal of Fluid Mechanics*, vol. 54, no. 3, pp. 427–448, 1972.

[76] K. Hasselmann, T. Barnett, E. Bouws, H. Carlson, D. Cartwright, K. Enke, J. Ewing, H. Gienapp, D. Hasselmann, P. Kruseman et al., "Measurements of wind-wave growth and swell decay during the Joint North Sea Wave Project (JONSWAP)," Deutches Hydrographisches Institut, Tech. Rep., 1973.

[77] R. H. Stewart, *Introduction to physical oceanography*. Texas A & M University, 2004.

[78] K. Hasselmann, "On the non-linear energy transfer in a gravity-wave spectrum part 1. general theory," *Journal of Fluid Mechanics*, vol. 12, no. 4, pp. 481–500, 1962.

[79] ——, "On the non-linear energy transfer in a gravity wave spectrum part 2. conservation theorems; wave-particle analogy; irrevesibility," *Journal of Fluid Mechanics*, vol. 15, no. 2, pp. 273–281, 1963.

[80] ——, "On the non-linear energy transfer in a gravity-wave spectrum. part 3. evaluation of the energy flux and swell-sea interaction for a neumann spectrum," *Journal of Fluid Mechanics*, vol. 15, no. 3, pp. 385–398, 1963.

[81] S. R. Massel, *Ocean Waves Breaking and Marine Aerosol Fluxes (Atmospheric and Oceanographic Sciences Library)*. Springer, 2007.

[82] Y. Toba, "Local balance in the air-sea boundary processes," *Journal of the Oceanographical Society of Japan*, vol. 29, no. 5, pp. 209–220, 1973.

[83] M. Longuet-Higgins, D. Cartwright, and N. Smith, "Observations of the directional spectrum of sea waves using the motions of a floating buoy," in *Ocean Wave Spectra*. Englewood Cliffs, NJ: Prentice-Hall, 1961, pp. 111–132.

[84] T. S. Glickman, *Glossary of meteorology*, 2nd ed. Boston, MA, USA: American Meteorological Society, 2017, ch. Fully Developed Sea. [Online]. Available: http://glossary.ametsoc.org/wiki/Fully_developed_sea

[85] T. Ellison, *Survey in Mechanics*. Cambridge University Press, 1956, ch. Atmospheric turbulence, pp. 400–430.

[86] O. M. Phillips, "The equilibrium range in the spectrum of wind-generated waves," *Journal of Fluid Mechanics*, vol. 4, no. 04, pp. 426–434, 1958.

[87] W. J. Pierson, G. Neumann, and R. W. James, "Practical methods for observing and forecasting ocean waves by means of wave spectra and statistics," US Naval Hydrographyc Office, Tech. Rep. Publ. No. 603, 1955.

[88] M. Abramowitz and I. A. Stegun, *Handbook of mathematical functions: with formulas, graphs, and mathematical tables*. Courier Corporation, 1964, vol. 55.

[89] B. Weber and D. Barrick, "On the nonlinear theory for gravity waves on the ocean's surface. part i: Derivations," *Journal of Physical Oceanography*, vol. 7, no. 1, pp. 3–10, 1977.

[90] "IEEE Standard for Definitions of Terms for Antennas," *IEEE Std 145-2013 (Revision of IEEE Std 145-1993)*, pp. 1–50, March 2014.

[91] E. W. Gill, personal communication.

[92] S. Dawson, "The reflective property of an ellipse," 2001. [Online]. Available: http://www.math.ubc.ca/~cass/courses/m309-01a/dawson/

[93] M. Artin, *Algebra*. Pearson Prentice Hall, 2011.

[94] H. Anton, *Elementary Linear Algebra*. John Wiley & Sons, 2010.

[95] H. Royden and P. Fitzpatrick, *Real Analysis*. Prentice Hall, 2010. [Online]. Available: https://books.google.ca/books?id=0Y5fAAAACAAJ

[96] W. Rudin, *Real and Complex Analysis*, ser. Mathematics series. McGraw-Hill, 1987.

[97] A. N. Tikhonov, "Solution of incorrectly formulated problems and the regularization method," *Soviet Mathematics Doklady*, vol. 4, pp. 1035–1038, 1963.

[98] V. Y. Arsenin, "On ill-posed problems," *Russian Mathematical Surveys*, vol. 31, no. 6, p. 93, 1976. [Online]. Available: http://stacks.iop.org/0036-0279/31/i=6/a=R06

[99] A. Neubauer, "Tikhonov regularization of nonlinear iii-posed problems in hilbert scales," *Applicable Analysis*, vol. 46, no. 1-2, pp. 59–72, 1992.

[100] J. Mueller and S. Siltanen, *Linear and Nonlinear Inverse Problems with Practical Applications*. Philadelphia, PA: Society for Industrial and Applied Mathematics, 2012.

[101] C. W. Groetsch, "Integral equations of the first kind, inverse problems and regularization: a crash course," *Journal of Physics: Conference Series*, vol. 73, no. 1, p. 012001, 2007. [Online]. Available: http://stacks.iop.org/1742-6596/73/i=1/a=012001

[102] A.-M. Wazwaz, *Linear and Nonlinear Integral Equations: Methods and Applications*. Springer, 2011.

[103] S. I. Kabanikhin, "Definitions and examples of inverse and ill-posed problems," *Journal of Inverse and Ill-Posed Problems*, vol. 16, no. 4, pp. 317–357, 2008.

[104] G. Chavent, *Nonlinear least squares for inverse problems: theoretical foundations and step-by-step guide for applications*. Springer Science & Business Media, 2010.

[105] L. Vandenberghe, "Ee133a lecture notes," 2017. [Online]. Available: http://www.seas.ucla.edu/~vandenbe/133A/133A-notes.pdf

[106] J. N. Franklin, "Well-posed stochastic extensions of ill-posed linear problems," *Journal of Mathematical Analysis and Applications*, vol. 31, no. 3, pp. 682–716, 1970.

[107] D. L. Phillips, "A technique for the numerical solution of certain integral equations of the first kind," *J. ACM*, vol. 9, no. 1, pp. 84–97, Jan. 1962.

[108] K. Levenberg, "A method for the solution of certain non-linear problems in least squares," *Quarterly of Applied Mathematics*, vol. 2, no. 2, pp. 164–168, 1944. [Online]. Available: http://www.jstor.org/stable/43633451

[109] D. W. Marquardt, "An algorithm for least-squares estimation of nonlinear parameters," *Journal of the Society for Industrial and Applied Mathematics*, vol. 11, no. 2, pp. 431–441, 1963.

[110] H. W. Engl, K. Kunisch, and A. Neubauer, "Convergence rates for tikhonov regularisation of non-linear ill-posed problems," *Inverse Problems*, vol. 5, no. 4, p. 523, 1989.

[111] S. G. Krein and Y. I. Petunin, "Scales of banach spaces," *Russian Mathematical Surveys*, vol. 21, no. 2, p. 85, 1966. [Online]. Available: http://stacks.iop.org/0036-0279/21/i=2/a=R03

[112] U. Tautenhahn, "On a general regularization scheme for nonlinear ill-posed problems: Ii. regularization in hilbert scales," *Inverse Problems*, vol. 14, no. 6, p. 1607, 1998. [Online]. Available: http://stacks.iop.org/0266-5611/14/i=6/a=016

[113] S. Lu, S. Pereverzev, Y. Shao, U. Tautenhahn et al., "On the generalized discrepancy principle for tikhonov regularization in hilbert scales," *Journal of Integral Equations and Applications*, vol. 22, no. 3, pp. 483–517, 2010.

[114] H. W. Engl, M. Hanke, and A. Neubauer, *Regularization of inverse problems*. Springer Science & Business Media, 1996, vol. 375.

[115] P. C. Hansen, "Analysis of Discrete Ill-Posed Problems by Means of the L-Curve," *SIAM Review*, vol. 34, no. 4, pp. 561–580, 1992.

[116] P. C. Hansen and D. P. OLeary, "The Use of the L-Curve in the Regularization of Discrete Ill-Posed Problems," *SIAM Journal on Scientific Computing*, vol. 14, no. 6, pp. 1487–1503, 1993.

[117] J. Flemming, "Generalized tikhonov regularization: basic theory and comprehensive results on convergence rates," Ph.D. dissertation, Chemnitz, Germany, October 2011.

[118] B. Kaltenbacher, A. Neubauer, and O. Scherzer, *Iterative Regularization Methods for Nonlinear Ill-Posed Problems*. Berlin/Boston, GERMANY: De Gruyter, 2008.

[119] A. Neubauer, "Tikhonov regularisation for non-linear ill-posed problems: optimal convergence rates and finite-dimensional approximation," *Inverse Problems*, vol. 5, no. 4, p. 541, 1989. [Online]. Available: http://stacks.iop.org/0266-5611/5/i=4/a=008

[120] D. E. Barrick, "Remote sensing of sea state by radar," in *Ocean 72 - IEEE International Conference on Engineering in the Ocean Environment*, Sept 1972, pp. 186–192.

[121] R. Shahidi, personal communication.

[122] S. Oraintara, W. C. Karl, D. A. Castanon, and T. Q. Nguyen, "A method for choosing the regularization parameter in generalized tikhonov regularized linear inverse problems," in *Proceedings 2000 International Conference on Image Processing (Cat. No.00CH37101)*, vol. 1, 2000, pp. 93–96 vol.1.

[123] International Telecommunication Union, "Recommendation ITU-R P.372-13: Radio noise," Geneva, Sep. 2016.

[124] ——, "Recommendation ITU-R SM.1753-2: Methods for measurements of radio noise," Geneva, Sep. 2012.

[125] W. J. Pierson, "Wind generated gravity waves," *Advances in geophysics*, vol. 2, pp. 93–178, 1955.

[126] B. J. Dawe, "Radio wave propagation over earth : field calculations and an implementation of the roughness effect," Master's thesis, Memorial University of Newfoundland. Faculty of Engineering and Applied Science, St. John's, Newfoundland and Labrador, Canada, 1988.

[127] R. M. Howard, *The Power Spectral Density*. Wiley-IEEE Press, 2002, pp. 59–91.